8-2016

Command shaping with constrained peak input acceleration to minimize residual vibration in a flexible-joint robot

Yumeng Wu
Purdue University

PURDUE UNIVERSITY
GRADUATE SCHOOL
Thesis/Dissertation Acceptance

This is to certify that the thesis/dissertation prepared

By Yumeng Wu

Entitled

COMMAND SHAPING WITH CONSTRAINED PEAK INPUT ACCELERATION TO MINIMIZE RESIDUAL VIBRATION IN A FLEXIBLE-JOINT ROBOT

For the degree of Master of Science in Mechanical Engineering

Is approved by the final examining committee:

Peter H. Meckl
Chair

Galen B. King

Raymond J. Cipra

To the best of my knowledge and as understood by the student in the Thesis/Dissertation Agreement, Publication Delay, and Certification Disclaimer (Graduate School Form 32), this thesis/dissertation adheres to the provisions of Purdue University's "Policy of Integrity in Research" and the use of copyright material.

Approved by Major Professor(s): Peter H. Meckl

Approved by: Jay P. Gore 7/10/2016

Head of the Departmental Graduate Program Date

COMMAND SHAPING WITH CONSTRAINED PEAK INPUT ACCELERATION TO MINIMIZE RESIDUAL VIBRATION IN A FLEXIBLE-JOINT ROBOT

A Thesis

Submitted to the Faculty

of

Purdue University

by

Yumeng Wu

In Partial Fulfillment of the

Requirements for the Degree

of

Master of Science in Mechanical Engineering

August 2016

Purdue University

West Lafayette, Indiana

Dedicated to

my father Dr. Xiaoqing Wu and my mother Xuezhen Fu

who have unsolicitedly supported me since I was born

ACKNOWLEDGMENTS

Foremost, I would like to extend my sincere gratitude to my thesis advisor, Prof. Peter Meckl, for his patience, immense knowledge and continuous support of my study and research.

I wish to thank other members of my advisory committee, Prof. Galen King and Prof. Raymond Cipra for their willingness and effort to serve in this capacity.

I would also like to thank my research partner and previous graduate mentor Alok Agrawal, for his willingness to help when I face obstacles and patience when I need time to digest theories; my research partner Nick, for his great support when we spent long hours to work in the lab.

TABLE OF CONTENTS

Page

LIST OF TABLES

LIST OF FIGURES

Figure Page

ABSTRACT

Wu, Yumeng MSME, Purdue University, August 2016. Command Shaping with Constrained Peak Input Acceleration to Minimize Residual Vibration in a Flexible-Joint Robot . Major Professor: Peter H. Meckl, School of Mechanical Engineering.

Rapid point-to-point motion is limited when flexibilities exist in the system. In order to minimize the vibrations related to joint flexibilities, much work has been done, including modifying the system so that vibrations can be damped out more quickly, calculating the inverse dynamics of the system and constructing shaped input profiles that avoid system natural frequencies. In this work, the earlier fixed-time command shaping method has been extended to a peak-acceleration-constrained approach with two basis functions, the ramped sinusoid function and the versine function, such that the maximum acceleration is guaranteed without overconstraining the input profiles. The approach is developed and then validated with a two-link flexible-joint robotic arm. The effect of peak input acceleration and weighting factor on residual vibrations has been studied. A performance metric has been developed to assess residual vibrations. Input profiles with two basis functions are compared with each other, as well as the results of a bang-bang profile. All simulations and experiments have shown the effectiveness of the command shaping method with constrained peak input acceleration on residual vibration reduction. In addition, the ability to weigh the trade-off between actuation time and settling time warrants the optimization of

total move time. Lastly, there exists an optimal weighting factor for each peak input acceleration to minimize the total move time and the total move time decreases with higher peak input acceleration.

1. INTRODUCTION

1.1 Motivation

Motion control is the foundation of almost all modern robots. Among them, many contemporary robotic systems perform rapid point-to-point motion with tight tolerance on precision. Such systems include industrial robotic arms, disk reader heads, printer jet heads, chip fabricating systems, etc. While residual vibration is the least desired feature, it is inevitable with the presence of flexibilities in these systems. Although such flexibilities cause undesired vibrations, they are natural characteristics of engineering systems, either unavoidable or designed-in. Flexibilities in such systems can be ascribed to transmission components, including gears, belts, and chains, or specially designed, for tolerance, safety, or optimization for human interaction. In certain cases, flexibility gives a buffer zone for potential collision and reduces the damage from impact.

While robotic systems are made for various tasks, most of them can be modeled as start-and-stop operations with focus on resulting motion only, for example, the disk reader head starts at initial position and stops at the desired coordinates of data; printer jet head moves to the desired location to print before printing. These operations are intended to be fast yet precise; however, in the presence of system flexibilities, achieving both tends to be difficult. Rapid motion requires large acceleration,

which ultimately excites resonance. Such resonance causes undesired vibration, impairing the system's ability to achieve precise motion control. This issue is significant if the system is lightly damped, such that residual vibrations lead to longer settling times.

1.2 Literature Review

Many researchers have aimed to reduce vibrations of flexible systems. Control strategies to reduce vibrations on flexible systems can be generalized to two categories: terminal controllers and tracking controllers. Terminal controllers are designed to take the system from an initial state to a final state while partially satisfying the desired performance. The control inputs are specified as smooth time functions in order to minimize excitation of system resonances. Aspinwall shaped a smooth time function to minimize excitation of system resonance in [1] by selecting the coefficients of a finite Fourier Series expansion, such that the envelope of the residual response spectrum is depressed in a desired region. The reduced vibration is at the cost of longer actuation time. Aspinwall's method requires twice as long as the time-optimal bang-bang profile. Various researchers, including Farrenkopf [2], Swigert [3], Turner and Junkins [4] and Turner and Chun [5], combined performance indices with Pontryagin's principle to generate optimal control functions. Hale, et al. [6] incorporated both the control input and its derivative with constraints of smooth start and stop transitions on the control input to minimize the excitation of system resonance.

Other open-loop approaches include the use of cam profile shapes and the use of a series of appropriately-timed step inputs to eliminate residual vibrations at the end of motion, which is also known as posicast control. Sehitoglu and Aristizabal [7] used such a profile to generate smooth motions without adaptation to system dynamics to minimize both move time and residual vibrations. Smith [8] presented the posicast control method for producing dead-beat response in a lightly-damped oscillatory feedback system. Beyond that, Singer [9] extended this concept to improve robustness to system parameter uncertainty while demanding less computation.

The controller utilized by tracking control theory is designed, just as its name implies, to track a reference input. The constant feedback gains are not determined with terminal states. Gupta [10] presented a "frequency-shaped cost functional" that tailors the controller to have less energy at frequencies corresponding to certain system modes. Balas [11] proposed "Innovations feedthrough" and output feedback control to prevent instability due to modes that are not modeled. Meirovitch, et al. [12] and Balas [13] developed modal controllers for dominant modes of distributed flexible systems. Heinrichfreise [14] developed a delicate three-joint elastic robot and constructed an observer to estimate unmeasured states. This technique requires an exact model of the system to achieve good control and to avoid making the system unstable.

Although traditional feedback methods can partially achieve the goal, the closed-loop system does not have enough damping to fully achieve the goal. Sweet and Good [15] and Futami, et al. [16] have proven that joint flexibilities impair the ability

of a controller to achieve desired performance. Common methods to address joint flexibilities can be categorized as modifying system dynamics and modifying the inputs. The first method modifies system dynamics such that the system would be forced to follow the input and minimize the vibration. The second method modifies the inputs and uses feedforward control. Readman [17] covered various control approaches for flexible-joint robots. Tomie [18] used a closed-loop PD controller to control a flexible system. Tian and Goldenberg [19] used joint torque feedback with robust adaptive control dealing with uncertainties to control a flexible system.

When dealing with flexible systems, researchers developed two categories of control strategies. The first one is to model and control the whole system based on the endpoint. This involves the modeling of both rigid and flexible parts at the same time. Obviously, this is more difficult and the bandwidth is limited because of the flexibility. The second one is to model the whole system but only control the actuators. Thus, the dynamics of flexible elements would not be involved in the control effort. Naturally, the controllers in this method are simpler and the input will be fed into the system with feedforward control. At the same time, the input is carefully constructed to reduce vibrations.

Feedforward control can be separated into two categories: forward compensation and inverse compensation. In forward compensation, a force applied to the system is constructed before the reference trajectory is derived. Such input forces are designed to avoid exciting flexible modes of the system. Removing all frequency content at high frequencies can avoid resonance in a flexible system. This can be achieved by

making the transition smoother, which is easy to implement as it does not require the knowledge of system flexibility. In inverse compensation, as explained by Moulin and Bayo [20], a force is calculated with the inverse dynamics of the system after the reference trajectory is determined. To compensate for the instability of plant inverse, Ghosh and Paden [21] presented pseudo-inverse methods; Lin and Hsiao [22] introduced the inverse adaptive feedforward control. Such alternatives cannot reduce vibrations without extending move time.

Command shaping methods attenuate the energy at known system natural frequencies to alleviate vibrations caused by flexible modes. Singer and Seering [23] shaped the input profile with a finite impulse response filter to remove energy at system natural frequencies. Bhat and Miu [24] proved the Laplace domain equivalence between filtering and placing zeros at undesirable system poles. This addresses the issue when selection of the input profile is limited by zero location. Thus, convolution of the input with a carefully-designed finite impulse response filter can improve system performance in terms of vibrations.

Meckl presented a command shaping method in [25] and [26]. This method constructs input commands with harmonics of a set of basis functions. Inputs constructed with such harmonics can minimize the energy at pre-selected frequencies, which naturally would be the system resonance frequencies, to minimize vibrations. Azad, et al. [27] compared two shaping methods and their experimental results. Beazel [28] confirmed that the command shaping method is robust to modeling errors and effective for systems having multiple modes. Chatlatanagulchai, Beazel and Meckl [29]

and Pao and Lau [30] proved that the command shaping method is also effective for time-varying systems and systems with configuration-dependent natural frequencies.

1.3 Overview of Thesis

This thesis covers the research on implementation of command shaping methods for a two-link flexible-joint robotic arm. The command shaping method proposed in [25] and [26] suggested a time-optimal solution to reduce vibration on a flexible robot. This method constructs a smooth force input profile by summing harmonics of sinusoidal basis functions with carefully-selected coefficients. The generated profile minimizes the energy at a band of frequencies around the system natural frequencies while at the same time approximating a bang-bang profile with a least square fit. Instead of generating a time-fixed profile as in [31], [28] and [32], this work presents the implementation of a profile in which the move time depends on constraints on the input amplitude.

The command shaping theory and the procedure for generating such profile with two different basis functions are presented in Chapter 2. With the developed profiles, validation of such profiles is completed with a specifically-built two-link flexible-joint robotic arm. This robotic arm has been well-studied and its mathematical model has been developed to serve as a testbed for shaped vibration-minimization input profiles. The physical system and its model are presented in Chapter 3. Experimental results of command shaping implementation with two different basis functions and

the corresponding performance metric are given in Chapter 4. Lastly, Chapter 5 presents the conclusion and proposes future work to refine this technique.

2. PEAK-ACCELERATION-CONSTRAINED COMMAND SHAPING

2.1 Background

The command shaping method reduces a system's residual vibration by shaping the input profile with minimized energy around the system natural frequencies. Meckl [25] developed the method to generate a profile that minimizes both time and residual vibrations. The approach approximates a bang-bang profile and avoids energy around the system natural frequencies. The input function uses the harmonics of select basis functions. Harmonics are given by characteristic numbers that satisfy the boundary value problem, which imposes zero magnitude and slope on the desired waveform. This method was used to design inputs for open-loop systems. Later, Meckl [26] extended his work to set up a weighted objective fitness function, such that the input would approximate the time-optimal bang-bang profile and penalize the energy at frequency bands around system natural frequencies. Such energy is calculated from the Fourier Transform of the basis functions. In order to be implemented on physical hardware, the command shaped input is incorporated with a feedback controller. With this setup, the plant and the feedback controller are treated as one part, thus, the input serves as reference to the feedback controller. When the method is implemented on current hardware, Beazel [28] took one step further and adapted the command-shaping method to a nonlinear system with configuration-dependent natu-

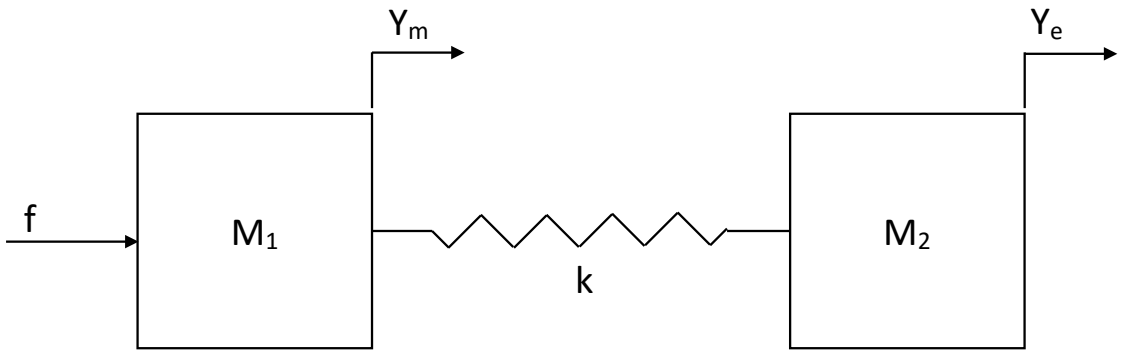

Figure 2.1. : Schematic of a Two-Mass System.

ral frequencies. Later, Scheel, et al. [32] refined the technique for the implementation on the physical robotic arm. In this work, the command shaping method is adapted to include an input acceleration constraint. As a result, weighting the trade-off between actuation time and settling time is possible, where actuation time is defined as the time between the start and the end of the input profile and settling time is defined as the time between the end of the input profile and the acceleration at the endpoint staying under a certain threshold level. The detail of settling time will be defined in Section 4.1.

2.2 Theory of Command Shaping

A two-mass system is shown in Figure 2.1, which is the starting point for analyzing the two-link robotic arm. This model simplified the robotic arm, while keeping the most important properties. The two-mass model has both a rigid body mode and a resonant mode. Thus, analyzing the two-mass model helps to understand the relationship between the residual vibrations and the resonant mode. In this figure,

M_1 represents motor inertia, M_2 represents endpoint inertia, and k represents transmission and structural stiffness. Starting with such two-mass system, Meckl [26] formulated the relationship between residual vibration and the magnitude of the Fourier Transform of the forcing function at the flexible mode of the system. Although the two-link robotic arm has two resonant modes instead of only one in the two-mass model, the conclusion from the two-mass model would still apply to the more complicated two-link robotic arm. The mathematical relationship is given by

$$A^* = \omega_n T_f \left| F^*(\omega_n T_f) \right|, \tag{2.1}$$

where A^* is the dimensionless residual vibration given in amplitude of acceleration; ω_n is the natural frequency of a two-mass system; T_f is the final move time; $|F^*(\omega_n T_f)|$ is the dimensionless Fourier Transform of the forcing function, which is defined in

$$|F^*(\omega_n T_f)| = \frac{|F^*(\omega_n)|}{F_{max} T_f}, \tag{2.2}$$

and F_{max} is the peak of the forcing function.

In this work, the forcing function has a general form given by

$$f(t) = \sum_{l=1}^{L} B_l \Phi_l^*(t), \tag{2.3}$$

where L is the total number of harmonics; l denotes the l^{th} harmonic; B_l is the coefficient for each harmonic and $\Phi_l^*(t)$ is the forcing function that will be detailed in Sections 2.3 and 2.4.

The shaped profile, which is the input to the system, is the reference trajectory. It is built with acceleration and then integrated for velocity and position. The acceleration profile has a general form as given by

$$\ddot{\theta} = \ddot{\theta}_{d,max} f(t). \tag{2.4}$$

Since $f(t)$ is normalized to a range between -1 and 1, the acceleration in the shaped profile ranges between $-\ddot{\theta}_{d,max}$ and $\ddot{\theta}_{d,max}$. Meckl [26] developed an objective function to measure how well the shaped profile approximates a bang-bang profile with penalty on energy at system natural frequencies. The general form of the objective function is given as

$$J_{gen} = \frac{1}{T_f} \int_0^{T_f} \left[f_{bangbang}(t) - f(t) \right]^2 dt + \rho \sum_{i=1}^{22} (\omega_i T_f)^2 |F^*(\omega_i T_f)|^2, \tag{2.5}$$

where $f_{bangbang}(t)$ and $f(t)$ are the bang-bang profile and commanded profile; T_f is the profile time, which is defined as the length of one segment of commanded profile. The summation of 22 terms of the Fourier Transform results from the 22 points around system natural frequencies, which will be further explained in Sections 2.3 and 2.4. With this setup, the objective function would cover a sufficiently big window around the system natural frequencies to give enough tolerance for modeling error. The goal

is to minimize the objective function J_{gen}. In order to do so, the derivative of J_{gen} with respect to B_l should be 0. This can be given by

$$\frac{\partial J_{gen}}{\partial B_l} = 0 \qquad (l = 1, 2, \ldots, L). \tag{2.6}$$

After coefficients B_l are found, they are normalized with a scale factor SF. The relationships are shown in

$$B_l^* = \frac{B_l}{SF}, \qquad SF = \max[|f(t)|]. \tag{2.7}$$

2.3 Ramped Sinusoid

Meckl introduced two basis functions to form a commanded profile in [25] and [26] to improve the robustness to the modeling error of the system. The first basis function is formed with a ramped sinusoid profile and its harmonics. This basis function has smooth transitions throughout the whole period and is odd symmetrical about $t = \frac{T_f}{2}$. The coefficient of each harmonic of the ramped sinusoid function is specially chosen, such that the requirement on magnitude of the frequency spectrum will be satisfied. In order to ensure its robustness to modeling error, this function minimizes energy at 11 equally-spaced points in a band of $\pm 10\%$ surrounding each system natural frequency.

The forcing function for the ramped sinusoid profile has the same form as Equation 2.3, but it has its own harmonic Φ_l^*, which is given by

$$\Phi_l^*(t) = \frac{1-2\tau}{2\alpha} + \frac{\sin(\alpha_l \tau)}{\alpha_l^2} - \frac{\cos(\alpha_l \tau)}{2\alpha_l}, \tag{2.8}$$

where τ is the dimensionless time defined as

$$\tau = \frac{t}{T_f}, \tag{2.9}$$

and α_l is the characteristic number associated with each harmonic. Such characteristic number of each harmonic can be calculated with

$$\alpha_l \sin \alpha_l + 2\cos \alpha_l - 2 = 0. \tag{2.10}$$

The first ten values of α are given in Table 2.1 and the first four harmonics of the ramped sinusoid functions are plotted in Figure 2.2.

The objective function for the ramped sinusoid function, given by

$$J_{rs} = \frac{1}{T_f}\left[\int_0^{\frac{T_f}{2}} [1-f(t)]^2 dt + \int_{\frac{T_f}{2}}^{T_f} [-1-f(t)]^2 dt\right] + \rho \sum_{i=1}^{22} (\omega_i T_f)^2 |F^*(\omega_i T_f)|^2, \tag{2.11}$$

is derived from Equation 2.5. Minimizing J_{rs} ensures the minimization of the sum of error with the bang-bang profile and energy at a 10% band around the system natural frequencies.

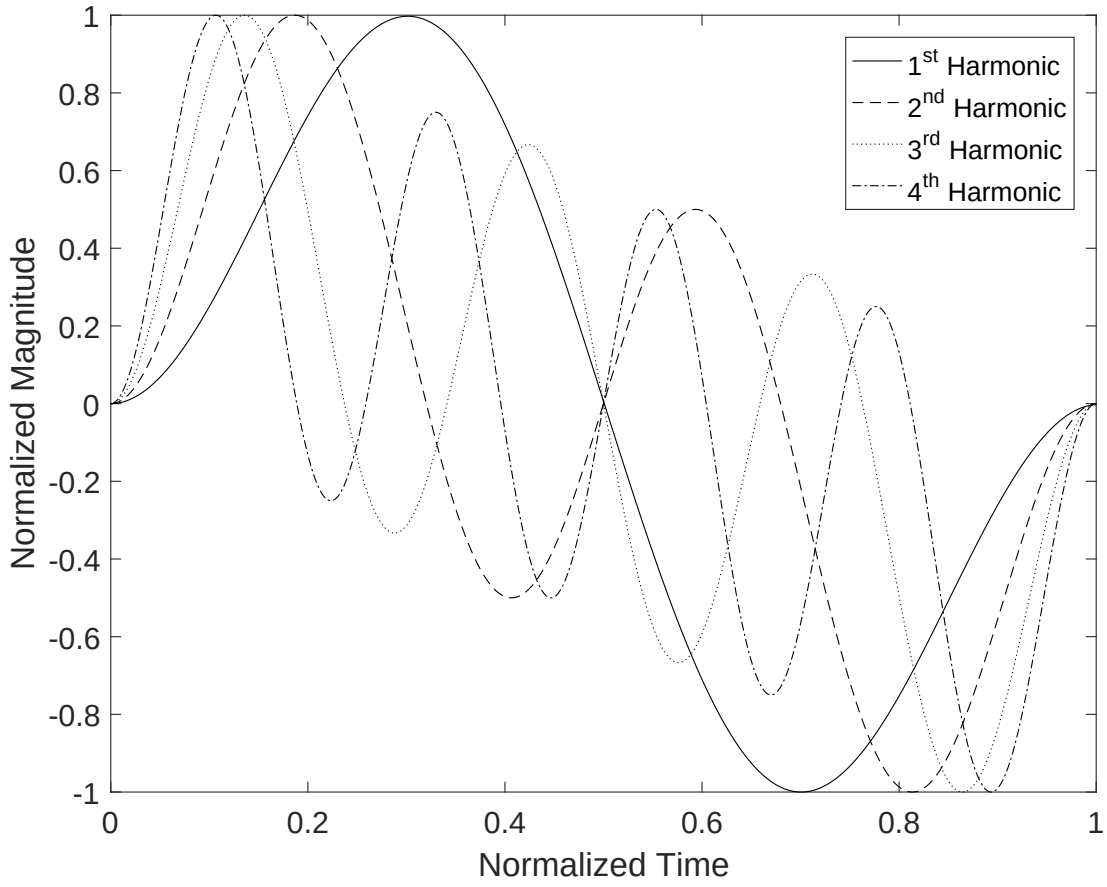

Figure 2.2. : First Four Harmonics of the Normalized Ramped Sinusoid Function.

Table 2.1. : Characteristic Number α Associated with First Ten Harmonics of the Ramped Sinusoid.

l^{th} Harmonic	Value
α_1	8.9688
α_2	15.4505
α_3	21.8082
α_4	28.1324
α_5	34.4415
α_6	40.7426
α_7	47.0389
α_8	53.3321
α_9	59.6232
α_{10}	65.9128

The coefficients of the harmonics B_l are calculated with Equation 2.6. With this technique, the general form equation can be derived as

$$\sum_{l=1}^{L} B_l I'_{r,l} = I^*_l, \tag{2.12}$$

where B_l, $I'_{r,l}$ and I^*_l are functions of α_r and α_l. The relationship between $I'_{r,l}$ and I^*_l is given by

$$\begin{aligned} I'_{r,l} =& I^*_{r,l} + \rho \sum_{i=1}^{22} (\omega_i T_s)^2 \frac{\alpha_r}{\alpha_r^2 - (\omega_i T_f)^2} \frac{\alpha_l}{\alpha_l^2 - (\omega_i T_f)^2} \\ & \left(\frac{2\sin(\frac{\omega_i T_f}{2}) - \omega_i T_f \cos(\frac{\omega_i T_f}{2})}{(\omega_i T_f)^2} \right)^2, \end{aligned} \tag{2.13}$$

where $I^*_{r,l}$ can be calculated with

$$I^*_{r,l} = \begin{cases} (12\alpha_r\alpha_l)^{-1} & r \neq l \\ \dfrac{1}{4\alpha_l^4} + \dfrac{5}{24\alpha_l^2} + \left[\dfrac{1}{16\alpha_l^3} - \dfrac{1}{4\alpha_l^5}\right]\sin(2\alpha_l) & \\ \quad + \left[\dfrac{1}{2\alpha_l^3} - \dfrac{2}{\alpha_l^5}\right]\sin\alpha_l + \dfrac{1}{4\alpha_l^4}\cos(2\alpha_l) + \dfrac{2}{\alpha_l^4}\cos\alpha_l & r = l, \end{cases} \tag{2.14}$$

and I^*_l can be calculated with

$$I^*_l = \frac{1}{\alpha_l^3}\left[\frac{\alpha_l^2}{4} - 2\cos\frac{\alpha_l}{2} - \alpha_l \sin\frac{\alpha_l}{2} + \cos\alpha_l + \frac{\alpha_l}{2}\sin\alpha_l + 1\right]. \tag{2.15}$$

There are two different times that determine the calculations based on Equation 2.11. T_s, given by

$$T_s = 2\sqrt{\frac{y_f}{a_{max}}}, \tag{2.16}$$

is the time for a rectangular pulse input that the command shaping method tries to approximate. a_{max} is the desired peak acceleration, which remains the same in the generated command shaping profile. y_f is the distance that either profile will travel. T_f is called the profile time, which is defined as the actual time for one command shaping profile. Since profiles with the ramped sinusoid functions only have one segment, the actuation time is equal to the profile time.

The relationship between T_f and T_s is given by

$$T_f = \Gamma T_s, \tag{2.17}$$

where Γ is a time penalty factor given by

$$\Gamma = \sqrt{\frac{3SF}{\sum_{l=1}^{L} B_l}}. \tag{2.18}$$

SF is the normalization factor, which normalizes the peak of the function to 1. Since the ramped sinusoid profile cannot supply as much energy as a bang-bang profile for a given peak input acceleration, a longer time is needed to travel the same distance with the same peak acceleration. As a result, Γ is always bigger than 1.

With a given T_f, the command shaping method would lead to an optimized profile with limited residual vibrations. The coefficient of each harmonic can be calculated with a set of linear equations, which can be expressed in a matrix form as

$$[I^*_{r,l}][B_l] = [I^*_l]. \tag{2.19}$$

Due to the inherent coupling between Γ and B_l, proper B_l cannot be calculated directly, such that an iteration procedure is necessary to determine the correct B_l and corresponding Γ. This procedure is listed as follows:

1. Use Equation 2.16 to determine the desired T_s based on a_{max} and y_f.
2. Specify an initial guess for Γ.
3. Solve for B_l with Equation 2.19.
4. Normalize the ramped sinusoid function with the scale factor SF.
5. Calculate Γ with Equation 2.18.
6. Use new Γ to update T_f with Equation 2.17.
7. Repeat steps 3 to 6 until Γ converges to acceptable accuracy, which means error between two values is less than 10^{-5}.

Initial guess can affect the convergence significantly. Based on experience, it could range between 1 and 100. For this work, the first three initial guesses are 2, 5 and 10. Although the convergence depends on the combination of ρ and a_{max}, these 3 initial guesses would lead at least 30% of combinations to convergence. Aitken acceleration, which updates Γ, written as

$$\Gamma_{i+3} = \frac{\Gamma_i \Gamma_{i+2} - \Gamma_{i+1}^2}{\Gamma_{i+2} - 2\Gamma_{i+1} + \Gamma_i}, \tag{2.20}$$

is used for every fourth Γ to improve the rate of convergence.

2.4 Versine

In real-world applications, the peak velocity is as important as peak acceleration. Ideally, the acceleration would decrease when the velocity is approaching the system's limit, however, this leads to a time-varying forcing function. As one can imagine, this time-varying function differs between systems, thus, a general approach is hard to develop. In order to address the issues, implementing a trapezoidal velocity profile would meet such requirements. With a trapezoidal velocity profile, both acceleration and deceleration segments will be controlled by a constant force and no force between two segments when the system operates in an ideal constrained-velocity condition. Thus, the command shaping method should resemble a trapezoidal velocity profile instead of a triangular velocity profile to reduce residual vibration in a peak-velocity-constrained system.

Since the ramped sinusoid cannot assemble either acceleration-only or deceleration-only profiles, the versine function was introduced by Meckl [26] to form a shaped profile as the other basis function. This basis function is smooth and has no discontinuity at the beginning or end. The versine function can be used to construct a rectangular pulse of either acceleration or deceleration by adding higher harmonics to the fundamental. Energy around natural frequencies can be attenuated with a similar technique to that introduced in Section 2.3. Eleven equally-spaced points in a band of $\pm 5\%$ surrounding each system natural frequency are evaluated for minimizing energy. This window is narrower than that used in the ramped sinusoid because the versine is

fine-tuned for each segment, leading to a smaller change of natural frequency between start and end of each segment.

The forcing function of the versine function shares the same form as Equation 2.3 with its own harmonic $\Phi_l^*(t)$, which is given by

$$\Phi_l^*(t) = 1 - \cos\frac{2\pi lt}{T_f} \qquad l = 1, 2, 3...L. \tag{2.21}$$

B_l is a specifically chosen coefficient for each harmonic, such that both move time T_f and magnitude of the frequency spectrum at 22 points surrounding two natural frequencies are minimized. One important thing differentiating the versine from the ramped sinusoid is that profiles with the versine functions have two segments. Each segment has to be evaluated separately, in other words, if both profiles are used to approximate the same bang-bang profile, T_s for the versine would be half of T_s for the ramped sinusoid. As a result, the actuation time is the summation of the two segments and the time of a possible segment with constant velocity.

The first three harmonics of the versine function are shown in Figure 2.3. As presented in the figure, each harmonic is even symmetrical about half of the period. Just like the technique used in finding proper B_l for each harmonic of the ramped sinusoid function, command shaping utilizing the versine as basis function also determines

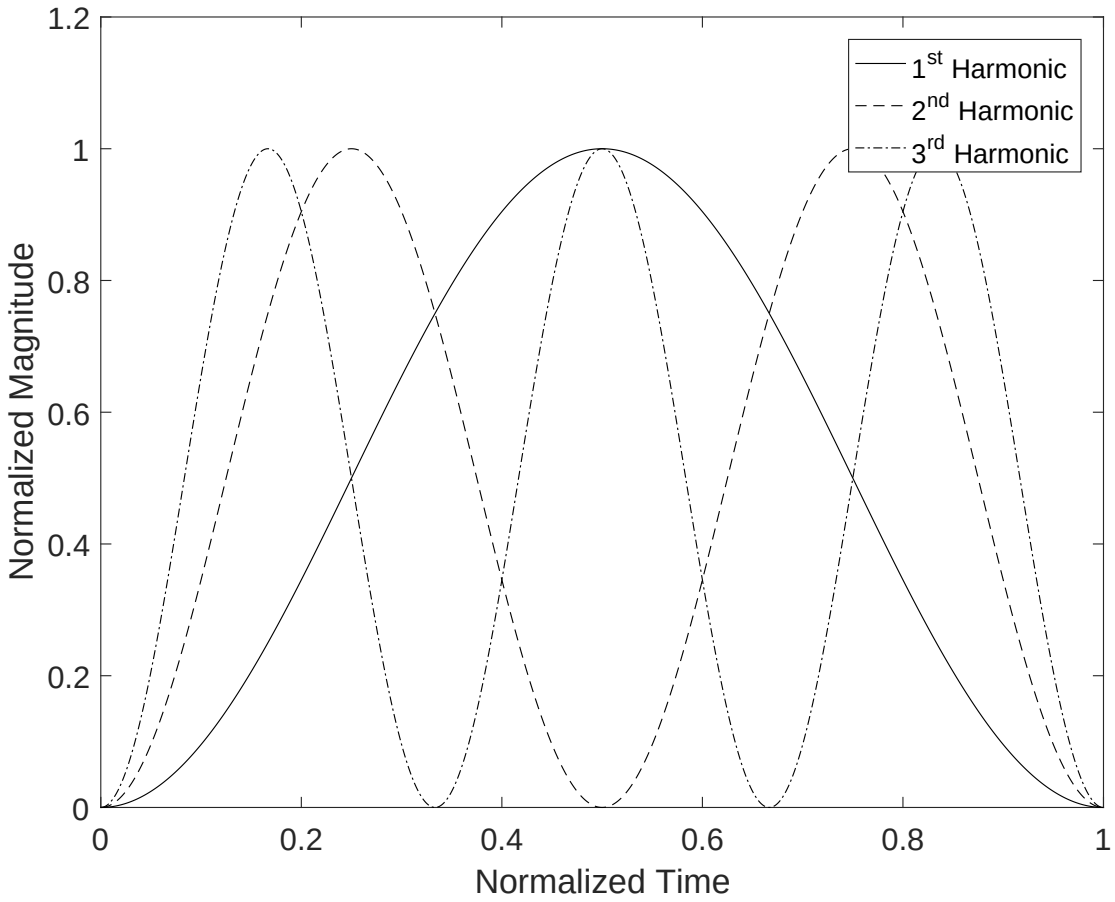

Figure 2.3. : First Three Harmonics of the Normalized Versine Function.

correct B_l for each harmonic with an objective function. This objective function J_v, given by the following equation

$$J_v = \frac{1}{T_f}\int_0^{T_f}[1-f(t)]^2dt + \rho\sum_{i=1}^{22}(\omega_i T_s)^2|F^*(\omega_i T_f)|^2, \tag{2.22}$$

minimizes the sum of error and magnitude at given frequencies. The waveform is approximated with a least square fit and the magnitude is calculated with the Fourier Transform of a versine function.

In order to minimize the objective function and solve for B_l, J_v is differentiated with respect to B_l. The value is set to be zero, which suggests a local minimum. This can be expressed as:

$$\sum_{l=1}^{L} B_l I'_{r,l} = 1, \tag{2.23}$$

where $I'_{r,l}$ is an intermediate variable to simplify the expression. It is given as

$$I'_{r,l} = I^*_{r,l} + 64\pi^4\rho\sum_{i=1}^{22}(\omega_i T_s)^2\frac{l^2}{(2\pi l)^2-(\omega_i T_f)^2}\frac{r^2}{(2\pi r)^2-(\omega_i T_f)^2}\frac{\sin^2\frac{\omega_i T_f}{2}}{(\omega_i T_f)}, \tag{2.24}$$

where

$$I^*_{r,l} = \begin{cases} 1 & r \neq l \\ & \\ 1.5 & r = l \end{cases}. \tag{2.25}$$

B_l can be calculated from these equations with given T_f using the following equations in matrix form:

$$[I'_{r,l}][B_l] = [1]_{20\times 1}. \tag{2.26}$$

Because T_f is not known in advance, iteration is required to find a good combination of T_f and B_l. Since the shaped profile would not supply as much energy as the square wave profile with the same peak acceleration, the time for a shaped profile has to be longer. This time penalty is given by

$$T_f = \Gamma_V T_s, \tag{2.27}$$

where

$$\Gamma_V = \frac{SF}{\sum_{l=1}^{L} B_l}, \tag{2.28}$$

and

$$T_s = \frac{v_{max}}{a_{max}}. \tag{2.29}$$

SF is the scale factor that normalizes the peak of the forcing function to be 1. v_{max} and a_{max} are the desired maximum velocity and the desired maximum acceleration for the square wave.

As T_f and B_l are dependent on each other, the iteration procedure introduced in Section 2.3 will be used:

1. Use Equation 2.29 to find the desired T_s based on v_{max} and a_{max}.

2. Specify an initial guess for Γ_V.

3. Solve for B_l with Equation 2.26.

4. Normalize the versine forcing function with the scale factor SF.

5. Calculate Γ_V with Equation 2.28.

6. For every 3 iterations, use Equation 2.20 to update the new Γ_V

7. Use the new Γ_V to update T_f with Equation 2.27.

8. Repeat steps 3 to 7 until Γ_V converges to acceptable accuracy, which means error between two values is less than 10^{-5}.

With this iteration procedure, the profile is guaranteed to be minimized both in time and magnitude of frequency spectrum at the desired frequencies.

3. HARDWARE SETUP

A two-link robotic arm is designed with typical flexibilities. This system serves as a generalized model, thus, better understanding of it is possible after extensive study. The hardware and its parameters are described in section 3.1, the mathematical model of the robot is given in section 3.2 and the parameters of this system are included in section 3.3. All of them serve as the foundation for further work, including controller design, simulation and implementation, to verify the effectiveness of the shaped input method.

3.1 Two-Link Robotic Arm

The hardware of the two-link robotic arm is physically located in Ruth and Joel Spira Laboratory for Electromechanical Systems in the School of Mechanical Engineering at Purdue University. The system is shown in Figure 3.1. It is custom-built with two sets of links, accelerometers, encoders, permanent magnet DC motors, chains and sprockets serving as transmission gears, where the two links are usually referred to as link 1 and link 2. It is designed to be a 2-DOF robotic arm operating in a horizontal plane. The first motor and the first link's encoder are mounted on the robot base, providing the inertia frame of reference for the two links. The second motor is mounted inside the housing at one end of the first link, which prevents interference

with the robot base. The second link's encoder and the first link's accelerometer are mounted at the other end of link 1. Both links are indirectly driven by corresponding motors utilizing transmission gears. The second link's accelerometer is mounted at the end of the second link, which also provides the ability to add loads to change the configuration of the system, such that the load effect can be investigated. This arm was first designed by Yegerlehner [33] to investigate controlling a rigid-joint nonlinear system and later modified by Kinceler [34] to study a flexible nonlinear system. Chatlatanagulchai programmed and implemented the controller with LabVIEW in [35]. Details of the hardware are presented in section 3.1.1.

3.1.1 Hardware Parameters

The whole set of experimental equipment includes LabVIEW version 8.5.1 with added modules in a desktop PC, which has the third-generation Intel Core i5 CPU and 16 GB RAM. The controller is programmed in this PC serving as a bridge between the user and the field-programmable gate array (FPGA) . The FPGA is National Instruments PXI-7831R, which has 8 analog inputs, 8 analog outputs and 96 digital channels with Virtex-II 1M gate. The FPGA provides the ability to deal with large amounts of data while operating. Although the FPGA supports at least 200 kHz sampling rate, it is configured to operate at 2 kHz in this implementation. Two National Instruments SCB-68 Shielded I/O Connector Blocks are connected to the FPGA, such that one of them is connected to deal with encoder readings and the other is used for other input signals.

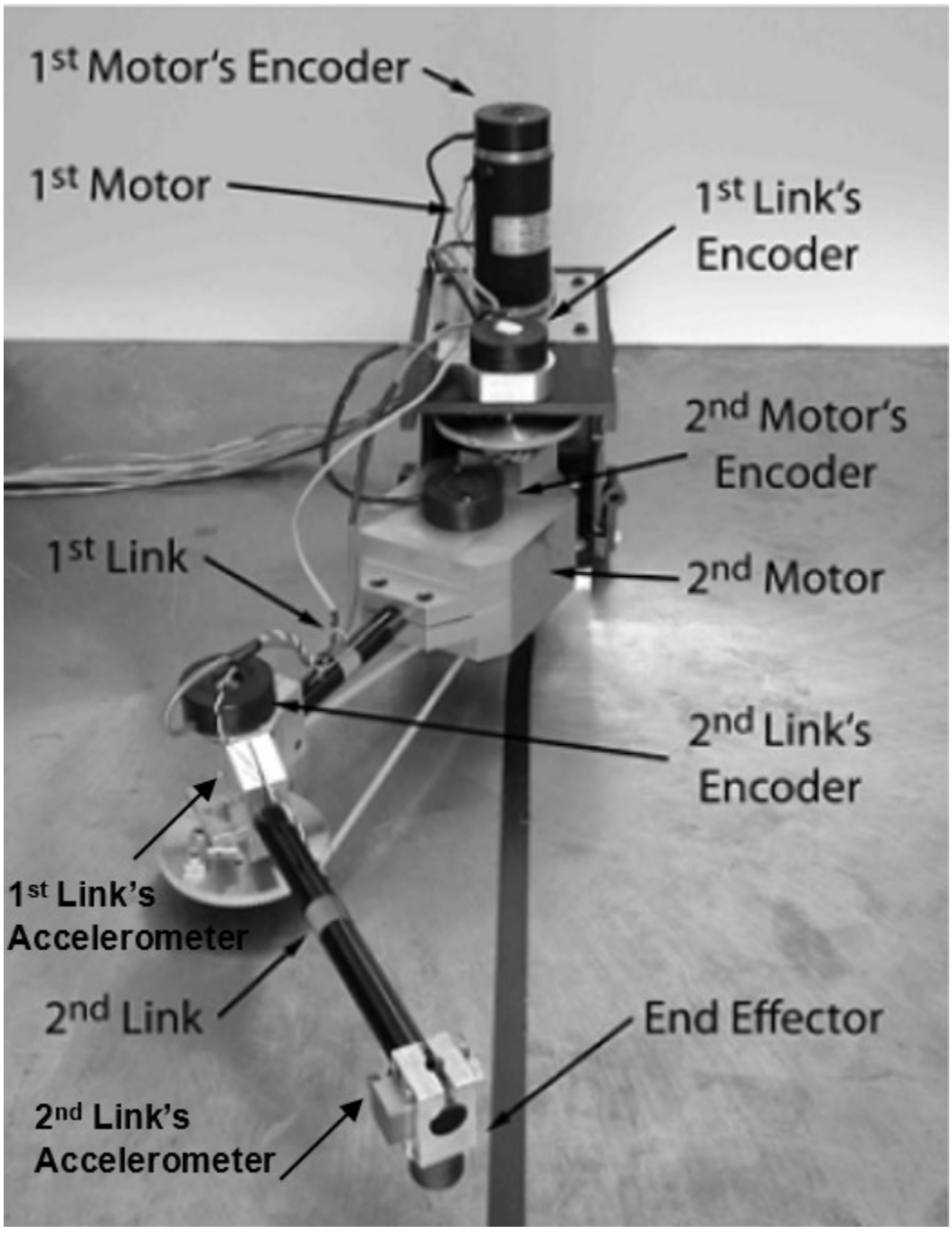

Figure 3.1. : Physical Setup of Robotic Arm [31].

A DC motor, model DPP242 made by Electro Craft, with maximum torque of 2.47 Nm at 21.2 A and a torque constant of 0.118 Nm/A is used to drive the first link. The DC motor driving the second link is an Inland T-3108-A, which has a maximum torque of 1.35 Nm at about 2 A, a torque constant of 0.61 Nm/A and, more importantly does not have a frame. Each motor is driven by an Advanced Motion Control brushless pulse-width-modulated transconductance servo amplifier, which converts input voltage commands into current commands.

Each link is indirectly connected to the corresponding motor with a torsional spring and a set sprockets and chain, which sets the gear ratio at 5. The spring coefficients of the two torsional springs range from 10^3 Nm/rad to 10^5 Nm/rad. These springs are designed to have small spring coefficients, such that the ability of the control and trajectory algorithm can be tested in a more challenging system.

An incremental optical encoder is used to measure the actual position of each link. The encoder on the 1^{st} link is Model R80 made by Renco Encoders. The encoder on the 2^{nd} link is Model RM21 also made by Renco Encoders. The resolution of each encoder is 4000 counts per revolution. Velocity is calculated by taking finite differences of the encoder readings with a 4^{th}-order Butterworth filter. A Kistler model 8315A single-axis accelerometer is used to measure linear acceleration at the end of each link. This model of accelerometer has a range of ± 2 g, sensitivity of 2 V/g, frequency response between 0 and 250 Hz and the resolution of 0.35 mg.

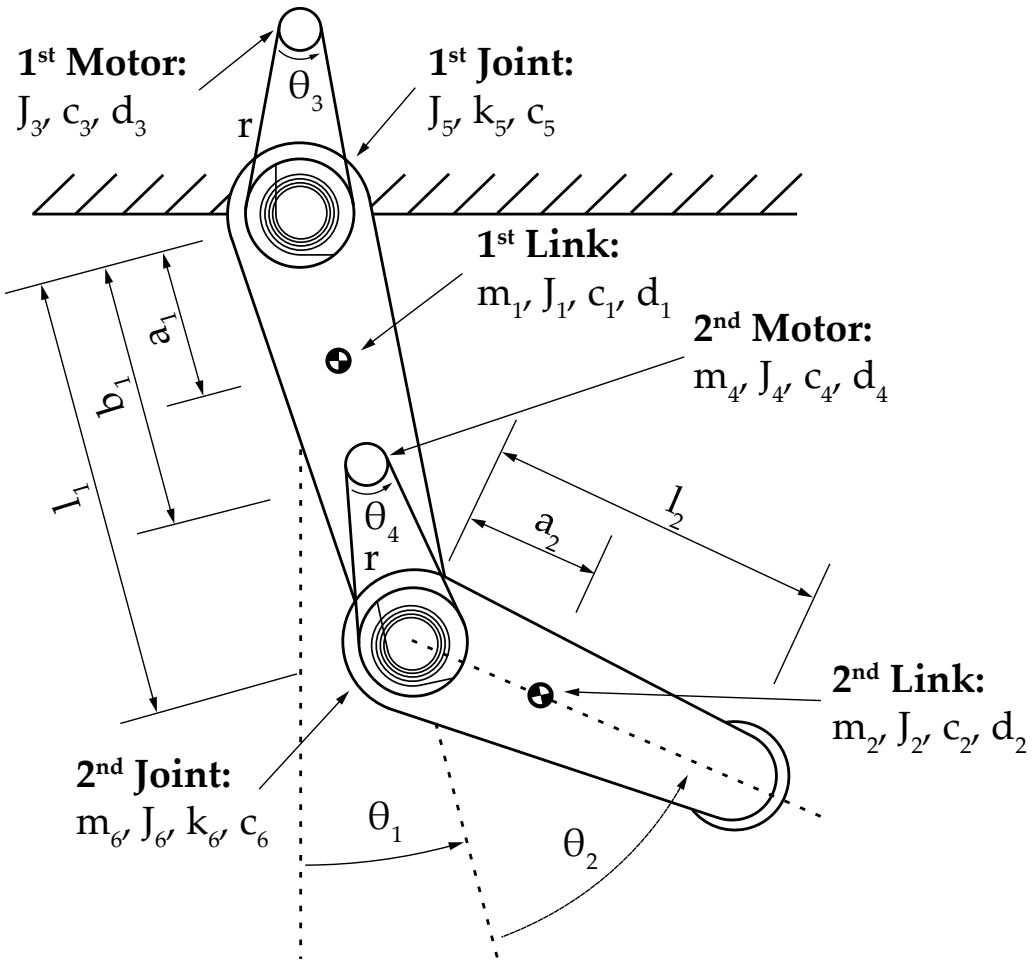

Figure 3.2. : Schematic of Two-Link Robotic Arm with parameters [36].

3.2 Mathematical Model of Robot

The physical setup of the two-link robotic arm with name of each component is shown in Figure 3.1. Notation of physical parameters of the robotic arm, which are shown in Figure 3.2, helps to interpret the relationship between elements. The technique utilized to identify these parameters is included in the following subsections. It is important to note that angles related to Link 1, which are Link 1 angle and Motor 1 angle, θ_1 and θ_3, are measured in an inertial reference, while angles related to Link 2, which are Link 2 angle and Motor 2 angle, θ_2 and θ_4, are measured relative to Link 1.

3.2.1 Lagragian Model

Nho [36] derived a Lagragian model for this robotic arm. Both friction and damping due to motors, links and torsional springs are modeled. The model in [36] included an intelligent payload estimation system, which is not a focus for this work, thus, the payload is chosen to be 0 instead. As a result, the payload effect is not analyzed in either simulation or experiments.

The Lagrangian Model of the robotic arm with notations shown in Figure 3.2 can be written as

$$\mathbf{M}(\theta)\ddot{\theta} + \mathbf{V}(\theta, \dot{\theta}) + \mathbf{C}\dot{\theta} + \mathbf{K}\theta + \mathbf{D} = \mathbf{T}, \tag{3.1}$$

in which θ is the generalized notation of θ_i.

$\mathbf{M}(\theta)$ in Equation 3.1 is the inertia matrix that can be calculated with

$$\mathbf{M}(\theta) = \begin{bmatrix} m_{11} & m_{12} & 0 & m_{14} \\ m_{21} & m_{22} & 0 & 0 \\ 0 & 0 & m_{33} & 0 \\ m_{41} & 0 & 0 & m_{44} \end{bmatrix}, \tag{3.2}$$

wherein m_i are the lumped masses and can be calculated with the corresponding equations:

$$m_{11} = m_1 a_1^2 + m_2(l_1^2 + a_2^2) + m_4 b_1^2 + m_6 l_1^2 + J_1 + J_2 + J_4 + J_6 + 2 l_1 m_2 a_2 \cos(\theta_2), \tag{3.3}$$

$$m_{12} = m_{21} = m_2 a_2^2 + J_2 + l_1 m_2 a_2 \cos(\theta_2), \tag{3.4}$$

$$m_{14} = m_{41} = J_4 + \frac{J_6}{r}, \tag{3.5}$$

$$m_{22} = m_2 a_2^2 + J_2, \tag{3.6}$$

$$m_{33} = J_3 + \frac{J_5}{r^2}, \tag{3.7}$$

$$m_{44} = J_4 + \frac{J_5}{r^2}, \tag{3.8}$$

where J_i represents the moment of inertia; l_i represents the length of the corresponding link; a_i represents the distance between the center of gravity of the link and its joint; b_1 represents the distance between the second motor and the first joint; r represents the gear ratio resulting from the transmission mechanism with sprockets and chain.

$\mathbf{V}(\theta, \dot{\theta})$ is the matrix of Coriolis and centrifugal forces, which can be calculated with

$$\mathbf{V}(\theta, \dot{\theta}) = \begin{bmatrix} \mathbf{V}_{\text{link}} \\ 0 \end{bmatrix} = \begin{bmatrix} -m_2 l_1 a_2 (2\dot{\theta}_1 \dot{\theta}_2 + \dot{\theta}_2^2) \sin(\theta_2) \\ m_2 l_1 a_2 \dot{\theta}_1^2 \sin(\theta_2) \\ 0 \\ 0 \end{bmatrix}, \tag{3.9}$$

where $\dot{\theta}_i$ represents the angular velocity of the corresponding link.

$\mathbf{C}$ is the matrix of viscous damping, which can be calculated with

$$\mathbf{C} = \begin{bmatrix} c_1 + c_5 & 0 & -\frac{c_5}{r} & 0 \\ 0 & c_2 + c_6 & 0 & -\frac{c_6}{r} \\ -\frac{c_5}{r} & 0 & c_3 + \frac{c_5}{r^2} & 0 \\ 0 & -\frac{c_6}{r} & 0 & c_4 + \frac{c_6}{r^2} \end{bmatrix}, \tag{3.10}$$

where c_i represents the viscous damping coefficient of the corresponding element.

$\mathbf{K}$ is the matrix of stiffness coefficients, which can be calculated with

$$\mathbf{K} = \begin{bmatrix} k_5 & 0 & -\frac{k_5}{r} & 0 \\ 0 & k_6 & 0 & -\frac{k_6}{r} \\ -\frac{k_5}{r} & 0 & \frac{k_5}{r^2} & 0 \\ 0 & -\frac{k_6}{r} & 0 & \frac{k_6}{r^2} \end{bmatrix}, \tag{3.11}$$

where k_i is the stiffness coefficient of the corresponding torsional spring.

D is the matrix of Coulomb friction, which can be calculated with

$$\mathbf{D} = \begin{bmatrix} d_1 \text{sign}(\dot{\theta}_1) \\ d_2 \text{sign}(\dot{\theta}_2) \\ d_3 \text{sign}(\dot{\theta}_3) \\ d_4 \text{sign}(\dot{\theta}_4) \end{bmatrix}. \tag{3.12}$$

T is the matrix of torque, which can be calculated with

$$\mathbf{T} = \begin{bmatrix} 0 \\ \mathbf{T}_{\text{motor}} \end{bmatrix} = \begin{bmatrix} 0 \\ 0 \\ \mathbf{T}_1 \\ \mathbf{T}_2 \end{bmatrix}, \tag{3.13}$$

in which $\mathbf{T}_1$ represents the driving torque from the first motor and $\mathbf{T}_2$ represents the driving torque from the second motor.

3.2.2 Spong Model

While the full model of the robotic arm given in section 3.2.1 presents all features of the system, it is too complex to design a model-based feedback controller. In order to address the issue, a practical method is to keep the important characteristics of the dynamic system and simplify the model. Spong introduced a widely-accepted

reduced model in [37]. The reduced model is derived from the full Lagrangian model with the following two assumptions:

1. The damping coefficients of the torsional springs (c_5 and c_6) are negligible.

2. The kinetic energy of each motor is due only to its own rotation.

Assumption 2 is based on the fact that the rotor angular velocity of the motor will be significantly larger than the angular velocity of the link when the gear ratio is big, $r >> 1$. As a result, Equation 3.2 can be simplified.

Based on Assumption 1, Equation 3.10 will be simplified to

$$\mathbf{C}_{\text{reduced}} = \begin{bmatrix} c_1 & 0 & 0 & 0 \\ 0 & c_2 & 0 & 0 \\ 0 & 0 & c_3 & 0 \\ 0 & 0 & 0 & c_4 \end{bmatrix}. \tag{3.14}$$

Equation 3.14 can be further simplified to link damping matrix ($\mathbf{C}_{\text{link}}$) and motor damping matrix ($\mathbf{C}_{\text{motor}}$), given by

$$\mathbf{C}_{\text{link}} = \begin{bmatrix} c_1 & 0 \\ 0 & c_2 \end{bmatrix}, \qquad \mathbf{C}_{\text{motor}} = \begin{bmatrix} c_3 & 0 \\ 0 & c_4 \end{bmatrix}. \tag{3.15}$$

Thus, $\mathbf{C}_{\text{reduced}}$ can be further simplified to

$$\mathbf{C}_{\text{reduced}} = \begin{bmatrix} \mathbf{C}_{\text{link}} & 0 \\ 0 & \mathbf{C}_{\text{motor}} \end{bmatrix}. \tag{3.16}$$

Based on Assumption 2, Equation 3.2 can be simplified to

$$\mathbf{M}_{\text{reduced}}(\theta) = \begin{bmatrix} m_{11} & m_{12} & 0 & 0 \\ m_{21} & m_{22} & 0 & 0 \\ 0 & 0 & m_{33} & 0 \\ 0 & 0 & 0 & m_{44} \end{bmatrix}, \tag{3.17}$$

which can be further simplified to

$$\mathbf{M}_{\text{reduced}}(\theta) = \begin{bmatrix} \mathbf{M}_1(\theta) & 0 \\ 0 & \mathbf{M}_3 \end{bmatrix}, \tag{3.18}$$

with the introduction of $\mathbf{M}_1(\theta)$ and $\mathbf{M}_3$, defined as

$$\mathbf{M}_1(\theta) = \begin{bmatrix} m_{11} & m_{12} \\ m_{21} & m_{22} \end{bmatrix}, \qquad \mathbf{M}_3 = \begin{bmatrix} m_{33} & 0 \\ 0 & m_{44} \end{bmatrix}. \tag{3.19}$$

Equation 3.1 can be rewritten as link part:

$$\mathbf{M}_1(\theta)\ddot{\theta}_{\text{link}} + \mathbf{V}_{\text{link}}(\theta_{\text{link}}, \dot{\theta}_{\text{link}}) + \mathbf{C}_{\text{link}}\dot{\theta}_{\text{link}} + \mathbf{K}_{\text{s}}(\theta_{\text{link}} - \frac{\theta_{\text{motor}}}{r}) = 0, \tag{3.20}$$

and motor part:

$$\mathbf{M}_3\ddot{\theta}_{\text{motor}} + \mathbf{C}_{\text{motor}}\dot{\theta}_{\text{motor}} + \mathbf{K}_{\text{s}}(\frac{\theta_{\text{motor}}}{r^2} - \frac{\theta_{\text{link}}}{r}) = \mathbf{T}_{\text{motor}}, \tag{3.21}$$

with the introduction of

$$\mathbf{K}_{\text{s}} = \begin{bmatrix} k_5 & 0 \\ 0 & k_6 \end{bmatrix}, \tag{3.22}$$

where θ, θ_{link} and θ_{motor} are given by

$$\theta = \begin{bmatrix} \theta_{\text{link}} \\ \theta_{\text{motor}} \end{bmatrix} = \begin{bmatrix} \theta_1 \\ \theta_2 \\ \theta_3 \\ \theta_4 \end{bmatrix}. \tag{3.23}$$

Equations 3.20 and 3.21 show that only torsional springs in joints couple the links and the motors. Thus, equations 3.20 and 3.21 can be expressed as a 4^{th}-order state space system, given by

$$\dot{x} = \begin{bmatrix} \dot{x_1} \\ \dot{x_2} \\ \dot{x_3} \\ \dot{x_4} \end{bmatrix} = \begin{bmatrix} x_3 \\ x_4 \\ -\mathbf{M}_1(\theta)^{-1}[\mathbf{V}_{\text{link}} + \mathbf{C}_{\text{link}}\dot{\theta}_{\text{link}} + \mathbf{K}_{\text{s}}(\theta_{\text{link}} - \frac{\theta_{\text{motor}}}{r})] \\ -\mathbf{M}_3^{-1}[\mathbf{T}_{\text{motor}} - \mathbf{C}_{\text{motor}}\dot{\theta}_{\text{motor}} - \mathbf{K}_{\text{s}}(\frac{\theta_{\text{motor}}}{r^2} - \frac{\theta_{\text{link}}}{r})] \end{bmatrix}, \tag{3.24}$$

with state variables defined as

$$x = \begin{bmatrix} x_1 \\ x_2 \\ x_3 \\ x_4 \end{bmatrix} = \begin{bmatrix} \theta_{\text{link}} \\ \theta_{\text{motor}} \\ \dot{\theta}_{\text{link}} \\ \dot{\theta}_{\text{motor}} \end{bmatrix}. \tag{3.25}$$

3.3 System Parameters

The essential step before generating command profiles, designing model-based controllers and developing a simulation model is identifying precise system physical parameters. This step is even more critical for a robotic arm with nonlinearities and flexibilities, which violate modeling assumptions. Various approaches have been implemented to get precise parameter estimates through experiments in the past. Nho [36] was the first to do system identification on this two-link robotic arm. The least square fit used by Nho simplifies and linearizes the Lagrangian model by grouping certain parameters, which determines all parameters of the two-link robotic arm simultaneously.

All experiments were conducted with open-loop data before Lee performed the first estimated system parameters with closed-loop data in [38]. After re-identifying system parameters with closed-loop data, Lee found that the parameters led to unstable simulation. Later, he re-estimated the system parameters with a new system identification method based on the algorithm he had implemented on a NARMAX

model of the robot. Although the offsets in torque still remain in the simulation model, this method improves the simulation with Fourier regularization. With the offsets in torque signals fixed and the first motor replaced, new system identification was performed by Scheel, et al. [32]. Instead of estimating all parameters at once, [32] split the identification procedure into multiple experiments. This approach makes tailoring experiments for certain parameters possible and eliminates the propagation of estimation errors from previous experiments. Scheel separated the procedure into three parts, which are the identification of two motors, the Link 1 and the Link 2. Each part was identified with one experiment. This approach identified the important dynamic behavior of the robotic arm and the parameters gave good agreement with robot data. As a result, these parameters have been used in this work as well. All physical parameters of the robotic arm are listed in Table 3.1. p_1, p_2 and p_3 in Table 3.1 are shorthand notation to represent parameters as follows:

$$p_1 = m_1 a_1^2 + m_2 l_1^2 + m_4 b_1^2 + m_6 l_1^2 + J_1 + J_4 + J_6, \tag{3.26}$$

$$p_2 = m_2 a_2^2 + J_2, \tag{3.27}$$

and

$$p_3 = l_1 m_2 a_2. \tag{3.28}$$

Table 3.1. : Identified Parameters of Robotic Arm.

Parameter	**Value**		**Parameter**	**Value**	
c_1	0.04	$\frac{\text{Nm·s}}{\text{rad}}$	k_5	2.848	$\frac{\text{Nm}}{\text{rad}}$
c_2	0.0214	$\frac{\text{Nm·s}}{\text{rad}}$	k_6	2.848	$\frac{\text{Nm}}{\text{rad}}$
c_3	$1.894 \cdot 10^{-4}$	$\frac{\text{Nm·s}}{\text{rad}}$	J_3	$4.157 \cdot 10^{-5}$	$\frac{\text{kg·m}^2}{\text{rad}}$
c_4	$1.497 \cdot 10^{-4}$	$\frac{\text{Nm·s}}{\text{rad}}$	J_4	$7.543 \cdot 10^{-4}$	$\frac{\text{kg·m}^2}{\text{rad}}$
c_5	0.005	$\frac{\text{Nm·s}}{\text{rad}}$	J_5	0.025	$\frac{\text{kg·m}^2}{\text{rad}}$
c_6	$8.128 \cdot 10^{-5}$	$\frac{\text{Nm·s}}{\text{rad}}$	J_6	0.025	$\frac{\text{kg·m}^2}{\text{rad}}$
d_1	0.0199	Nm	p_1	0.140	$\frac{\text{kg·m}^2}{\text{rad}}$
d_2	0.0323	Nm	p_2	0.0196	$\frac{\text{kg·m}^2}{\text{rad}}$
d_3	0.005	Nm	p_3	0.0234	$\frac{\text{kg·m}^2}{\text{rad}}$
d_4	0.0271	Nm			

3.4 Computed Torque Controller

Researchers have developed many robot control methods over the years. These methods include adaptive control, robust control, adaptive robust control [39], learning control and so on. Computed torque control is a common approach for controlling rigid-joint robots. Computed torque controller differs from the standard feedback linearization form of nonlinear controllers in that it cancels out the nonlinearities with estimates of the robot model, thus, linear error equations are decoupled with reduced nonlinearities. Although the approach has been developed for rigid-joint robots, the effectiveness of the controller on flexible-joint robots was proved in [29]. As a result, the computed torque controller is chosen and implemented in this work as well for its good trajectory tracking, disturbance rejection and insensitivity to modeling error.

The computed torque controller consists of a model-based part and a servo-based part. The model-based part neutralizes the nonlinearities in the system and the servo-based part ensures asymptotically stable motor tracking dynamics and the compensation of disturbances. A hybrid of the full Lagrangian Model, Equation 3.1, and the inertia matrix of the Spong Model, Equation 3.18, is used to design the model-based part. This implementation is due to the significant effort to compensate the cross-coupling term in the inertia matrix of the Spong Model, which does not pay off from the benefit of eliminating the negligible cross-coupling term. Let $\mathbf{C}_H$ denote the last two rows of viscous friction matrix Equation 3.10; let $\mathbf{K}_{\mathrm{v}}$ and $\mathbf{K}_{\mathrm{p}}$ denote the

diagonal matrices of proportional and derivative gains. Then the model-based part can be written as

$$\mathbf{T}_{mb} = \mathbf{C}_H\dot{\theta} + \mathbf{D}_M + \mathbf{K}_{\mathrm{s}}(\frac{\theta_{\mathrm{motor}}}{r^2} - \frac{\theta_{\mathrm{link}}}{r}), \tag{3.29}$$

and the servo-based part can be written as

$$\mathbf{T}_{sb} = \mathbf{M}_3\left(\ddot{\theta}_{M,d} + \mathbf{K}_{\mathrm{v}}(\dot{\theta}_{M,d} - \dot{\theta}_{\mathrm{motor}}) + \mathbf{K}_{\mathrm{p}}(\theta_{M,d} - \theta_{\mathrm{motor}})\right). \tag{3.30}$$

The total torque is the summation of both parts, therefore, it can be written as

$$\mathbf{T}_{\mathrm{motor}} = \mathbf{T}_{mb} + \mathbf{T}_{sb}. \tag{3.31}$$

The closed-loop motor dynamics given by

$$\ddot{\theta}_{\mathrm{motor}} + \mathbf{K}_{\mathrm{v}}\dot{\theta}_{\mathrm{motor}} = \ddot{\theta}_{M,d} + \mathbf{K}_{\mathrm{v}}\dot{\theta}_{M,d} + \mathbf{K}_{\mathrm{p}}\theta_{M,d} \tag{3.32}$$

can be developed from the aforementioned equations, assuming a perfect model. Furthermore, with the definition of motor tracking error

$$e_{\mathrm{motor}} = \theta_{M,d} - \theta_{\mathrm{motor}}, \tag{3.33}$$

Equation 3.32 can be simplified to

$$\ddot{e}_{\mathrm{motor}} + \mathbf{K}_{\mathrm{v}}\dot{e}_{\mathrm{motor}} + \mathbf{K}_{\mathrm{p}}e_{\mathrm{motor}} = 0. \tag{3.34}$$

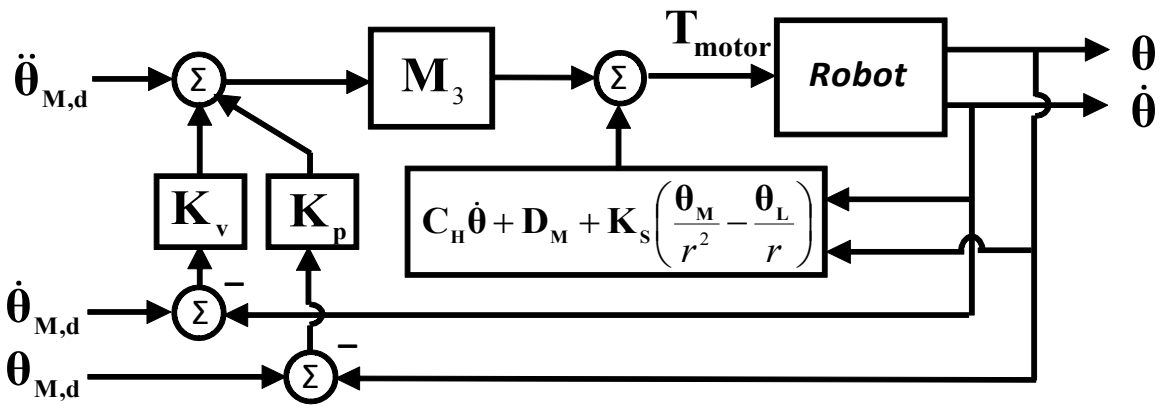

Figure 3.3. : Block Diagram of the Computed Torque Controller and the Robotic Arm [29].

$\mathbf{K}_p$ and $\mathbf{K}_v$ are chosen so that Equation 3.32 is Hurwitz. Thus, asymptotic tracking is guaranteed with computed torque and the link subsystem is stable. Figure 3.3 is the block diagram of the computed torque controller and the robotic arm.

3.5 Configuration-Dependent Frequency

The linearization of the closed-loop system with the feedback controller gives the varying natural frequencies of the system. With the determined natural frequencies, the command shaping method can be applied to the robotic arm. The varying natural frequencies of the robotic arm are due to the varying inertia resulting from the change of configuration of the two links. The classical method of addressing such issues is by linearizing at the equilibrium point. Since the inertia matrix M is a function of θ_2, which is shown in Equation 3.2, the natural frequencies of the robotic arm are also a function of θ_2. Thus, the direct relationship between the Link 2 position, θ_2, and the natural frequencies of the robotic arm can be found.

Substituting T in Equation 3.1 with $\mathbf{T}_{\text{motor}}$ in Equation 3.31 leads to the closed-loop equations of the robotic arm. In order to obtain the linearized form of the equations, Taylor expansions are performed on all rows up to the first-order term for an equilibrium point of both zero velocity and zero acceleration as a function of θ_2. The Coulomb friction is not considered in the linearized equations, since the derivatives of the Coulomb friction with respect to the velocity are assumed to be zero. As a result, the linearized closed-loop equation of the robotic arm is obtained as

$$\mathbf{M}_{\text{linearized}}\ddot{\theta} + \mathbf{C}_{\text{linearized}}\dot{\theta} + \mathbf{K}_{\text{linearized}}\theta = 0. \tag{3.35}$$

$\mathbf{M}_{\text{linearized}}$ is the linearized inertia matrix and can be represented as

$$\mathbf{M}_{\text{linearized}} = \begin{bmatrix} m_{\text{linearized,11}} & m_{\text{linearized,12}} & 0 & m_{14} \\ m_{\text{linearized,21}} & m_{22} & 0 & 0 \\ 0 & 0 & m_{33} & 0 \\ m_{41} & 0 & 0 & m_{44} \end{bmatrix}, \tag{3.36}$$

which has linearized matrix $m_{\text{linearized,11}}$, $m_{\text{linearized,12}}$ and $m_{\text{linearized,21}}$.

$m_{\text{linearized,11}}$ can be written as

$$\begin{aligned} m_{\text{linearized,11}} =& m_1 a_1^2 + m_2(l_1^2 + a_2^2) + m_4 b_1^2 + m_6 l_1^2 + J_1 \\ &+ J_2 + J_4 + J_6 + 2 l_1 m_2 a_2 \cos(\theta_{\text{linearized,2}}) \end{aligned}, \tag{3.37}$$

while $m_{\text{linearized,12}}$ and $m_{\text{linearized,21}}$ can be written as

$$m_{\text{linearized,12}} = m_{\text{linearized,21}} = m_2 a_2^2 + J_2 + l_1 m_2 a_2 \cos(\theta_{\text{linearized,2}}). \tag{3.38}$$

Besides the linearized inertia matrix, viscous damping matrix C and stiffness matrix K have to be linearized as well, which are given as

$$\mathbf{C}_{\text{linearized}} = \begin{bmatrix} c_1 + c_5 & 0 & -\frac{c_5}{r} & 0 \\ 0 & c_2 + c_6 & 0 & -\frac{c_6}{r} \\ -\frac{c_5}{r} & 0 & m_{33}\mathbf{K}_{\text{v,3}} & 0 \\ 0 & -\frac{c_6}{r} & 0 & m_{44}\mathbf{K}_{\text{v,4}} \end{bmatrix} \tag{3.39}$$

and

$$\mathbf{K}_{\text{linearized}} = \begin{bmatrix} k_5 & 0 & -\frac{k_5}{r} & 0 \\ 0 & k_6 & 0 & -\frac{k_6}{r} \\ 0 & 0 & m_{33}\mathbf{K}_{\text{p,3}} & 0 \\ 0 & 0 & 0 & m_{44}\mathbf{K}_{\text{p,4}} \end{bmatrix}. \tag{3.40}$$

With the linearized parameters, the natural frequencies of the linearized closed-loop system can be calculated by finding the imaginary part of the eigenvalues of the system matrix $\mathbf{A}$, given by

$$\mathbf{A} = \begin{bmatrix} 0 & \mathbf{I} \\ -\mathbf{M}_{\text{linearized}}^{-1}\mathbf{K}_{\text{linearized}} & -\mathbf{M}_{\text{linearized}}^{-1}\mathbf{C}_{\text{linearized}} \end{bmatrix}, \tag{3.41}$$

where $\mathbf{I}$ is the identity matrix.

As $\mathbf{M}_{\text{linearized}}$ is a function of θ_2, the eigenvalues of matrix $\mathbf{A}$ are also functions of θ_2. If the damping of the system is increased, the natural frequencies of the system will change. More specifically, the resonance peak will be more flattened. Meckl studied the impact of damping on system response in [26]. The system response degrades if more inherent damping is not considered in the command shaping method. In [26], the command shaping method is proved to be successful for lightly-damped systems, specifically for $\zeta < 0.3$. The command shaping method can be directly applied to the two-link robotic arm because it meets the requirement as a lightly-damped system. The configuration-dependent natural frequencies of the robotic arm, ω_1 and ω_2, have evident relationship with the position of Link 2, θ_2. This relationship is presented in Figure 3.4.

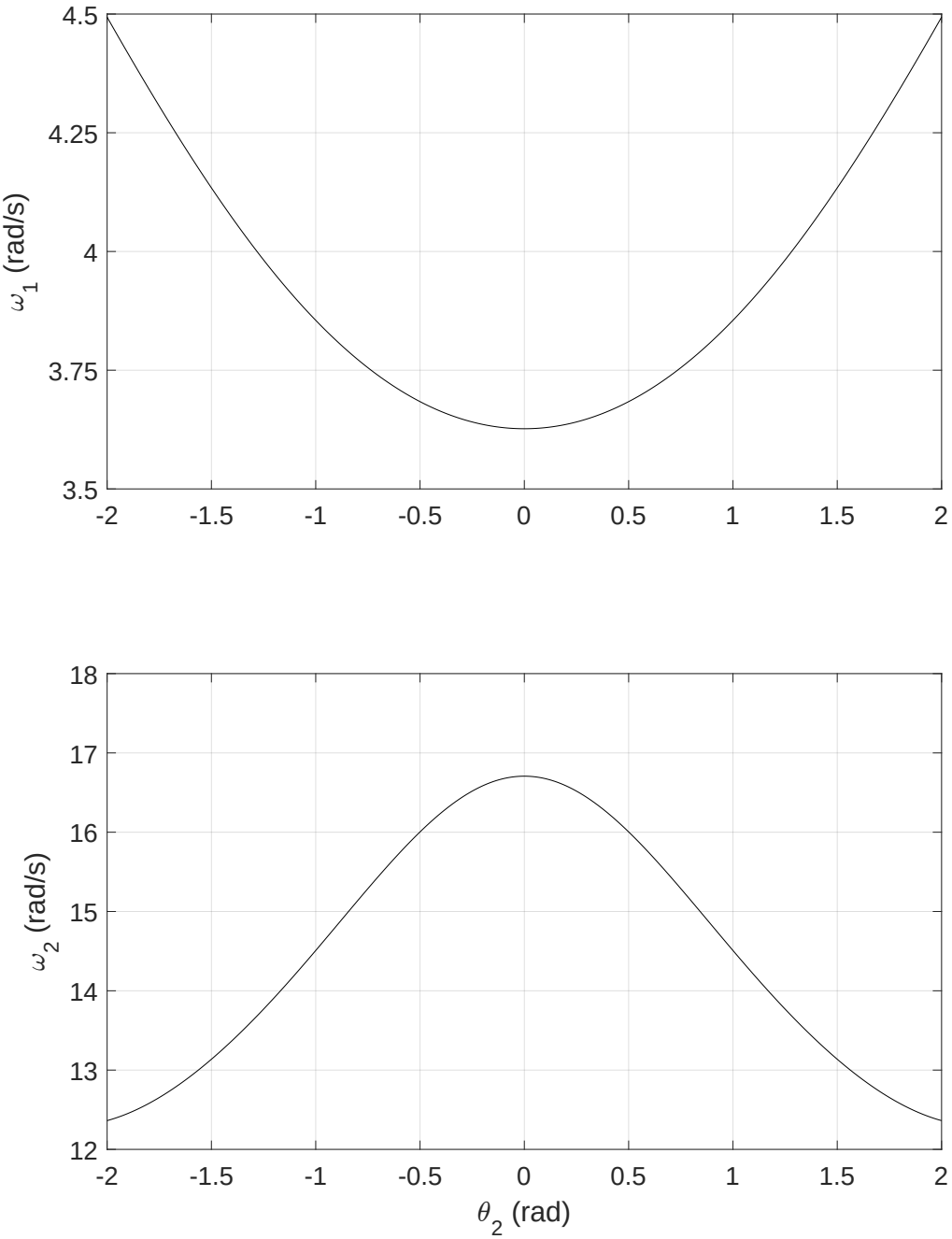

Figure 3.4. : Configuration-dependent natural frequencies of the system as a function of the position of the 2^{nd} link.

4. APPLICATION TO THE TWO-LINK FLEXIBLE-JOINT ROBOTIC ARM

Since the command shaping method is introduced in Chapter 2 and the two-link flexible-joint robotic arm is explained in Chapter 3, this chapter will include the application of command shaping profiles to the two-link flexible-joint robotic arm. Section 4.1 describes how to rank each profile and compare the results meaningfully. Section 4.2 includes both the input profiles and the corresponding experimental results from a bang-bang profile, which is used as a benchmark. Then Section 4.3 discusses the command shaping method with ramped sinusoid functions, in which the section is further split to three subsections. Section 4.3.1 includes constructing and analyzing the input signals with ramped sinusoid functions. Section 4.3.2 gives the simulations of the application of input profiles with ramped sinusoid functions to the robotic arm. After that, Section 4.3.3 validates the simulations with the physical robotic arm. Section 4.4 follows the same logic as Section 4.3 with three subsections, which are Sections 4.4.1, 4.4.2 and 4.4.3, while the basis function is changed to the versine function.

4.1 Performance Matrics

With so many types of data collected from the experiments, a proper performance matrix is required to judge how well each profile can reduce vibrations. The important

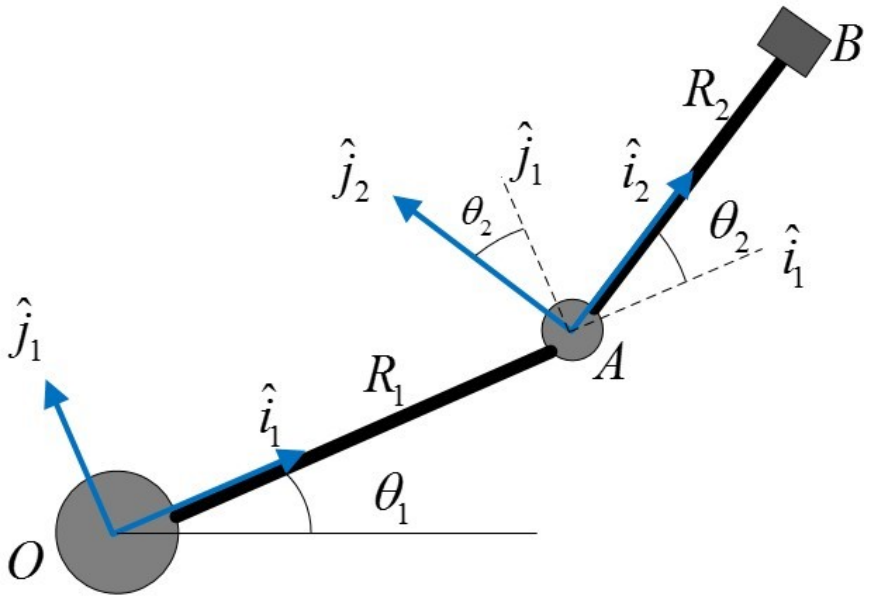

Figure 4.1. : Vector Loop of the Robotic Arm [31].

aspects of residual vibration are amplitude and duration. A common approach to analyze these two parameters is to fit a dissipation envelope to the response. As data is measured with respect to its local reference frame and the robotic arm is a nonlinear system with two modes, the vibration amplitude and settling time can no longer be analytically derived. This work presents a single parameter to illustrate the magnitude of residual vibrations in a straightforward way. This parameter is the magnitude of acceleration at the endpoint of the robotic arm. The rationale behind this is that any acceleration after the profile stops is undesirable, no matter in which direction it acts. The endpoint acceleration $\ddot{\overrightarrow{OB}}$ can be derived with a vector loop, which is shown in Figure 4.1. The notations in this figure are listed as follows:

- i_1 and j_1 are the vectors along the 1^{st} link and normal to it.
- i_2 and j_2 are the vectors along the 2^{nd} link and normal to it.

- R_1 represents the length of the 1^{st} link.
- R_2 represents the length of the 2^{nd} link.
- θ_1 represents the angle between the 1^{st} link and the inertia frame.
- θ_2 represents the angle between the 1^{st} link and the 2^{nd} link.

As can be seen from Figure 4.1, the endpoint of the 1^{st} link and that of the 2^{nd} link are not in the same reference frame. Therefore, a transformation is needed to convert either of the links in order to put both links in the same reference frame. Starting with the 1^{st} link, the position vector is

$$\overrightarrow{OA} = R_1\hat{i}_1 \tag{4.1}$$

and the velocity vector is

$$\dot{\overrightarrow{OA}} = R_1\omega_1\hat{j}_1, \tag{4.2}$$

where ω_1 is the angular velocity of the 1^{st} link. As a result, the acceleration at point A would be

$$\begin{aligned}\ddot{\overrightarrow{OA}} &= R_1\omega_1^2\hat{k}_1 \times \hat{j}_1 + R_1\dot{\omega}_1\hat{j}_1 \\ &= -R_1\omega_1^2\hat{i}_1 + R_1\dot{\omega}_1\hat{j}_1 \\ &= -R_1\omega_1^2\hat{i}_1 + a_1\hat{j}_1,\end{aligned} \tag{4.3}$$

where a_1 is the acceleration signal collected from the accelerometer at point A.

The same method is applied to analyze point B at the end of the 2^{nd} link. The position vector is given as

$$\begin{aligned}\overrightarrow{OB} &= \overrightarrow{OA} + \overrightarrow{AB} \\ &= R_1\hat{i}_1 + R_2\hat{i}_2,\end{aligned} \tag{4.4}$$

and the velocity vector is

$$\dot{\overrightarrow{OB}} = R_1\frac{d\hat{i}_1}{dt} + R_2\frac{d\hat{i}_2}{dt} + \dot{R}_1\hat{i}_1 + \dot{R}_2\hat{i}_2. \tag{4.5}$$

Since both links are rigid, $\dot{R}_1$ and $\dot{R}_2$ are both 0. As a result,

$$\begin{aligned}\dot{\overrightarrow{OB}} &= R_1\omega_1\hat{k}_1 \times \hat{i}_1 + R_2\omega_2\hat{k}_2 \times \hat{i}_2 \\ &= R_1\omega_1\hat{j}_1 + R_2\omega_2\hat{j}_2.\end{aligned} \tag{4.6}$$

Then the acceleration vector is given as

$$\begin{aligned}\ddot{\overrightarrow{OB}} &= R_1\omega_1^2\hat{k}_1 \times \hat{j}_1 + R_1\dot{\omega}_1\hat{j}_1 + R_2\omega_2^2\hat{k}_2 \times \hat{j}_2 + R_2\dot{\omega}_2\hat{j}_2 \\ &= -R_1\omega_1^2\hat{i}_1 + R_1\dot{\omega}_1\hat{j}_1 - R_2\omega_2^2\hat{i}_2 + R_2\dot{\omega}_2\hat{j}_2 \\ &= -R_1\omega_1^2\hat{i}_1 + a_1\hat{j}_1 - R_2\omega_2^2\hat{i}_2 + a_2\hat{j}_2,\end{aligned} \tag{4.7}$$

where a_2 is the signal measured from the accelerometer at point B. Clearly, if $\hat{i}_1$ and $\hat{j}_1$ can be transformed to $\hat{i}_2$ and $\hat{j}_2$, the aforementioned equations will be simplified with a

more straightforward expression. With the knowledge of kinematics, the relationship between the two reference frames can be derived as

$$\begin{aligned} \hat{i}_2 &= \cos\theta_2 \hat{i}_1 + \sin\theta_2 \hat{j}_1 \\ \hat{j}_2 &= -\sin\theta_2 \hat{i}_1 + \cos\theta_2 \hat{j}_1. \end{aligned} \tag{4.8}$$

Thus,

$$\begin{bmatrix} \hat{i}_1 \\ \\ \hat{j}_1 \end{bmatrix} = \begin{bmatrix} \cos\theta_2 & -\sin\theta_2 \\ \\ \sin\theta_2 & \cos\theta_2 \end{bmatrix} \begin{bmatrix} \hat{i}_2 \\ \\ \hat{j}_2 \end{bmatrix}. \tag{4.9}$$

Then, plugging Equation 4.9 into Equation 4.7 gives

$$\begin{aligned} \ddot{\overrightarrow{OB}} &= \begin{bmatrix} -R_1\omega_1^2 & a_1 \end{bmatrix} \begin{bmatrix} \hat{i}_1 \\ \\ \hat{j}_1 \end{bmatrix} + \begin{bmatrix} -R_2\omega_2^2 & a_2 \end{bmatrix} \begin{bmatrix} \hat{i}_2 \\ \\ \hat{j}_2 \end{bmatrix} \\ &= \left(\begin{bmatrix} -R_1\omega_1^2 & a_1 \end{bmatrix} \begin{bmatrix} \cos\theta_2 & -\sin\theta_2 \\ \\ \sin\theta_2 & \cos\theta_2 \end{bmatrix} + \begin{bmatrix} -R_2\omega_2^2 & a_2 \end{bmatrix} \right) \begin{bmatrix} \hat{i}_2 \\ \\ \hat{j}_2 \end{bmatrix} \\ &= \begin{bmatrix} -R_1\omega_1^2\cos\theta_2 - R_2\omega_2^2 + a_1\sin\theta_2 & R_1\omega_1^2\sin\theta_2 + a_2 + a_1\cos\theta_2 \end{bmatrix} \begin{bmatrix} \hat{i}_2 \\ \\ \hat{j}_2 \end{bmatrix}. \end{aligned} \tag{4.10}$$

Thus, $\ddot{\overrightarrow{OB}}$ is expressed in terms of the measurements of 2^{nd} link position, angular velocity of each link from the corresponding encoder, and linear acceleration mea-

sured normal to each link in the reference frame of $\hat{i}_2$ and $\hat{j}_2$. Equation 4.10 makes calculating the magnitude of translational acceleration possible, which is

$$|\ddot{\overrightarrow{OB}}| = \sqrt{|\ddot{\overrightarrow{OB}}|_i^2 + |\ddot{\overrightarrow{OB}}|_j^2}. \tag{4.11}$$

The peak residual acceleration is defined as the maximum $\ddot{\overrightarrow{OB}}$ after the command profile ends, which is T_f seconds after the start. Usually the peak residual acceleration is measured right after the profile endpoint.

A common definition of the settling time is the time required for the system to settle within a certain percentage of the input amplitude, which is usually either 2% or 5%. This is not practical in that even 2% of the steady state value is too big to give a non-zero extra time after the profile stops. If any profile can give the zero-second settling time, then their performances can no longer be compared. As a result, a new definition of settling time is proposed for this work. The new settling time is defined as the time required for $\ddot{\overrightarrow{OB}}$ to stay below 0.3 m/s^2 after the input profile has stopped. Thus, the sum of actuation time and settling time is total move time. Figure 4.2 gives a visual illustration of the definition, where the purple dash line is the cutoff level at 0.3 m/s^2. The tolerance is selected based on simulations and experiments, such that the noise does not affect results and the performance of each profile can be ranked meaningfully. Naturally, the best profile has the least peak magnitude of residual acceleration and the smallest settling time.

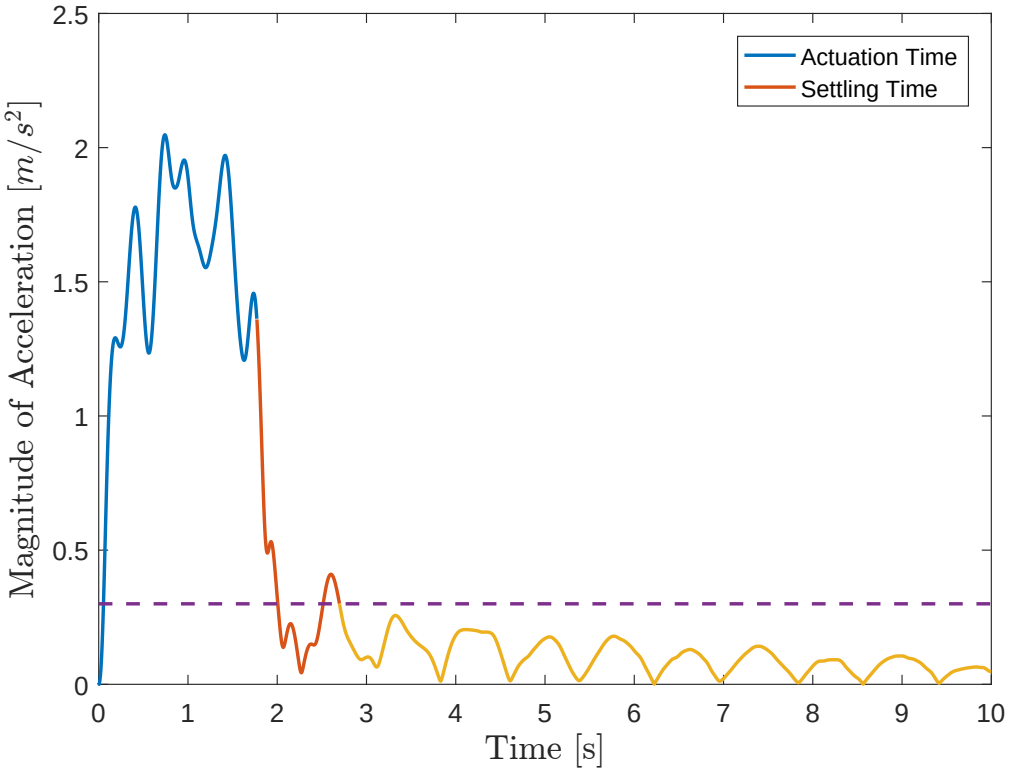

Figure 4.2. : Definitions of Actuation Time and Settling Time

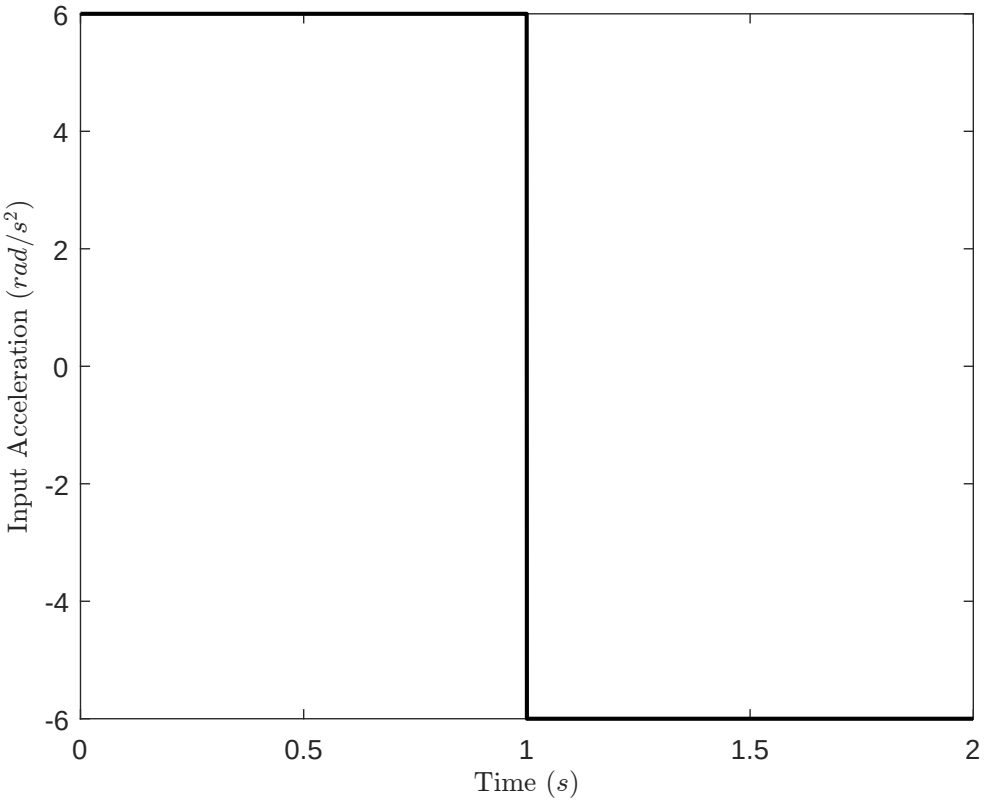

Figure 4.3. : Bang-bang Profile with $a_{max} = 6$ rad/s^2 running for 2 s.

4.2 Bang-Bang Profile

All commanded profiles will be compared with the traditional bang-bang profile on settling time and energy attenuation at selected frequencies. A bang-bang profile has a time-domain profile as shown in Figure 4.3. It consists of a segment of constant acceleration followed by a deceleration with same time span and magnitude.

This is the most efficient profile in terms of least actuation time with a given peak input acceleration. The frequency spectrum given in Figure 4.4 indicates that energy

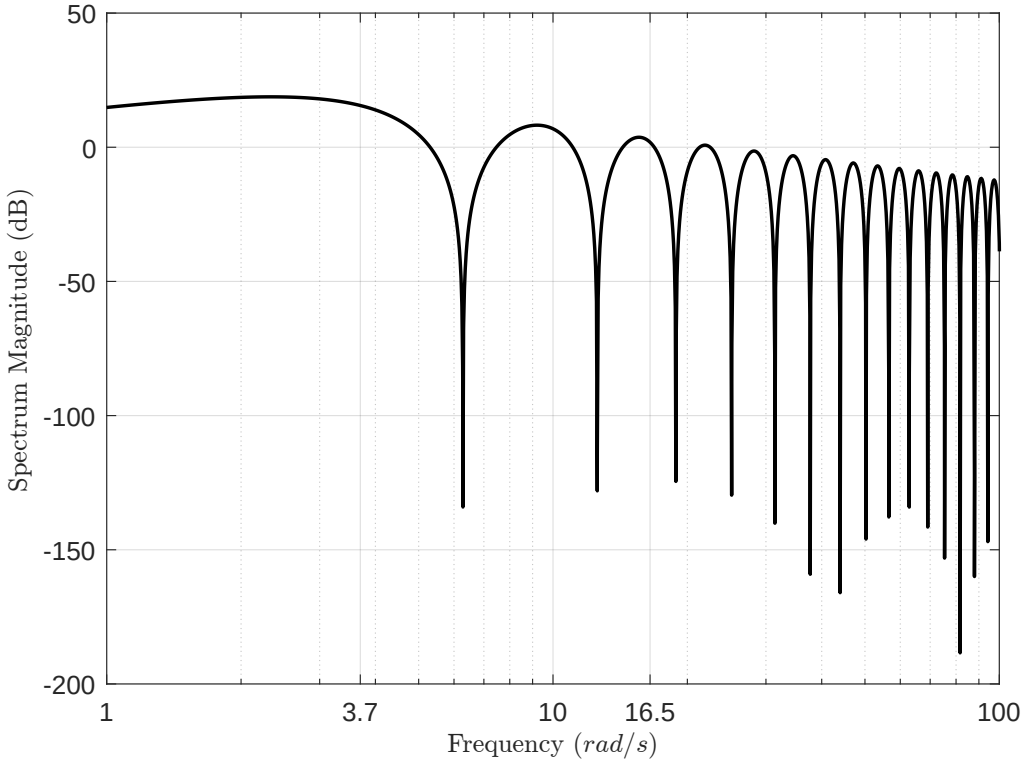

Figure 4.4. : Frequency Spectrum of a Bang-bang Profile with $a_{max} = 6$ rad/s^2 running for 2 s.

at system natural frequencies is not noticeably attenuated. As a result, this profile will excite system resonance and lead to significant residual vibrations.

Bang-bang profile has been implemented on the robotic arm in order to give an idea of how much residual vibrations will be added, as well as to be used as the benchmark for the command shaping method. The experimental results are shown in Figure 4.5. The desired link endpoints and motor trajectories are dashed. [a] and [b] are the desired acceleration profiles of the shoulder and elbow motors, [c] and [d] are the torque profiles for the 1^{st} and the 2^{nd} motors, [e] and [f] are the angular positions of the 1^{st} and the 2^{nd} links, [g] and [h] are the actual and desired angular positions

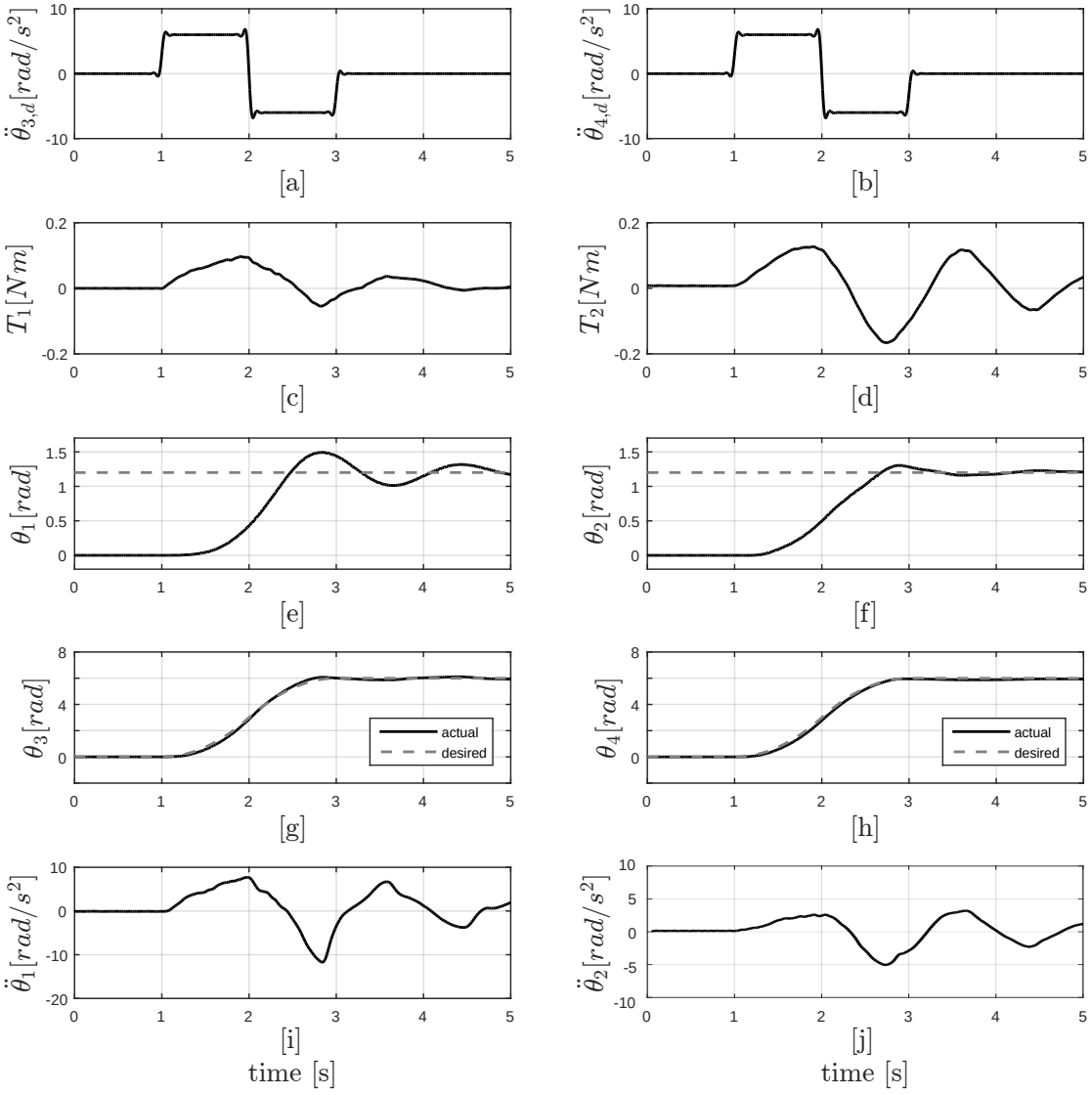

Figure 4.5. : Experimental Result of Bang-bang Profile on the Robotic Arm.

of the 1^{st} and the 2^{nd} motors, and [i] and [j] are the angular accelerations for the 1^{st} and the 2^{nd} links. As can be seen from [e] and [f], both links experience oscillation after the input ends. Acceleration signals in [i] and [j] also present significant residual vibrations. The settling time is 3.2985 seconds, which is more than 150% of the actuation time.

4.3 Ramped Sinusoid

The command shaping method is then implemented with a physical robotic arm, after both the theory and the hardware model have been studied. The desired profile drives both links to travel 1.2 rad. With a known gear ratio of 5, each motor needs to travel 6 rad. One essential step before constructing is to define the region of interest for peak input acceleration (a_{max}), since the input parameters to generate a profile with the command shaping method are a_{max} and ρ. Based on past experience, a good range of a_{max} is between 30 rad/s^2 and 75 rad/s^2. A step size of 5 rad/s^2 is chosen to give details on the effect of a_{max}. Because the objective function is sensitive to ρ, a step size of $\frac{1}{200}$ is used to investigate the effect of ρ.

This secton provides an analysis of the command shaping method with ramped sinusoid functions. Section 4.3.1 focuses on properties of input profiles; Section 4.3.2 focuses on simulation of the robotic arm with commanded profiles in MATLAB and Simulink; Section 4.3.3 focuses on experimental validation of simulation results on the physical system. Section 4.4 also has three subsections as Section 4.3 following the same logic as discussion on commanded profiles with versine functions.

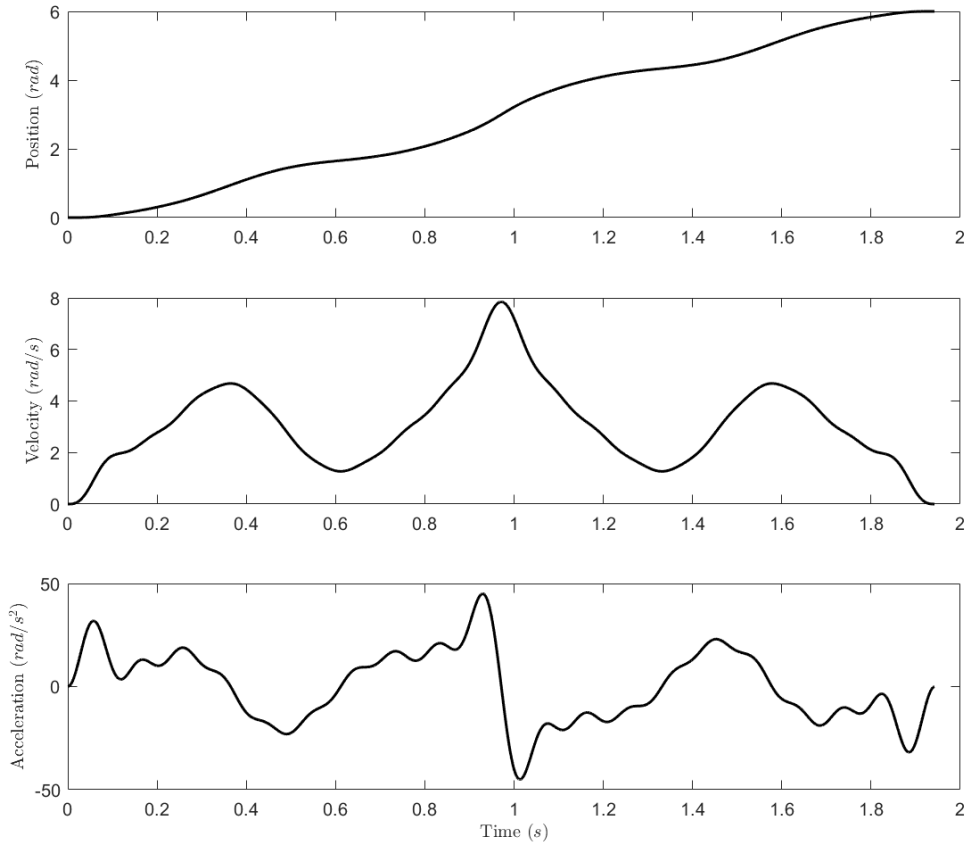

Figure 4.6. : Input Profile with $a_{max} = 45$ rad/s^2 and $\rho = 1$ with Ramped Sinusoid Functions.

4.3.1 Commanded Profile Analysis

Input profiles with ramped sinusoid functions are constructed with various a_{max} and ρ. As a general profile shaped with ramped sinusoid functions, Figure 4.6 presents the input profile with $a_{max} = 45$ rad/s^2 and $\rho = 1$ utilizing ramped sinusoid functions. Its frequency spectrum is given in Figure 4.7.

From the objective function J_{rs}, it is not hard to see that average energy at selected frequencies would be lower if ρ is higher. Figure 4.7 gives the comparison of

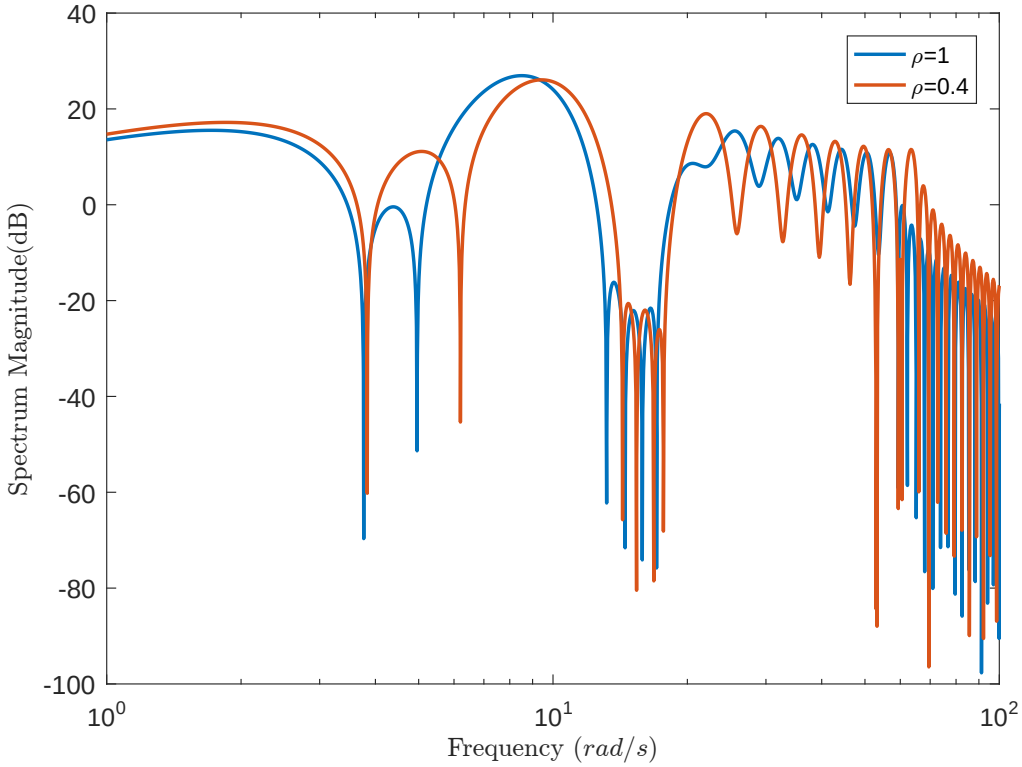

Figure 4.7. : Effect of ρ when a_{max} is 45 rad/s^2 with Ramped Sinusoid Functions.

two profiles with the same a_{max} of 45 rad/s^2, but different ρ. Both profiles have dips at system natural frequencies, indicating the command shaping method is working as expected. Dips of the profile having $\rho = 1$ are deeper than those of the profile having $\rho = 0.4$. Besides slightly deeper dips at system natural frequencies, the region with attenuated energy is wider. This leads to more tolerance for potential modeling error.

Figures 4.8 and 4.9 present the relationship between magnitude of frequency spectrum of input acceleration profile ($|F(\ddot{\theta}_{3,4})|$) and ρ for all interested a_{max}. Overall, $|F(\ddot{\theta}_{3,4})|$ decreases with higher ρ for the same peak input acceleration, however, $|F(\ddot{\theta}_{3,4})|$ is not monotonically decreasing with higher ρ. There are multiple local min-

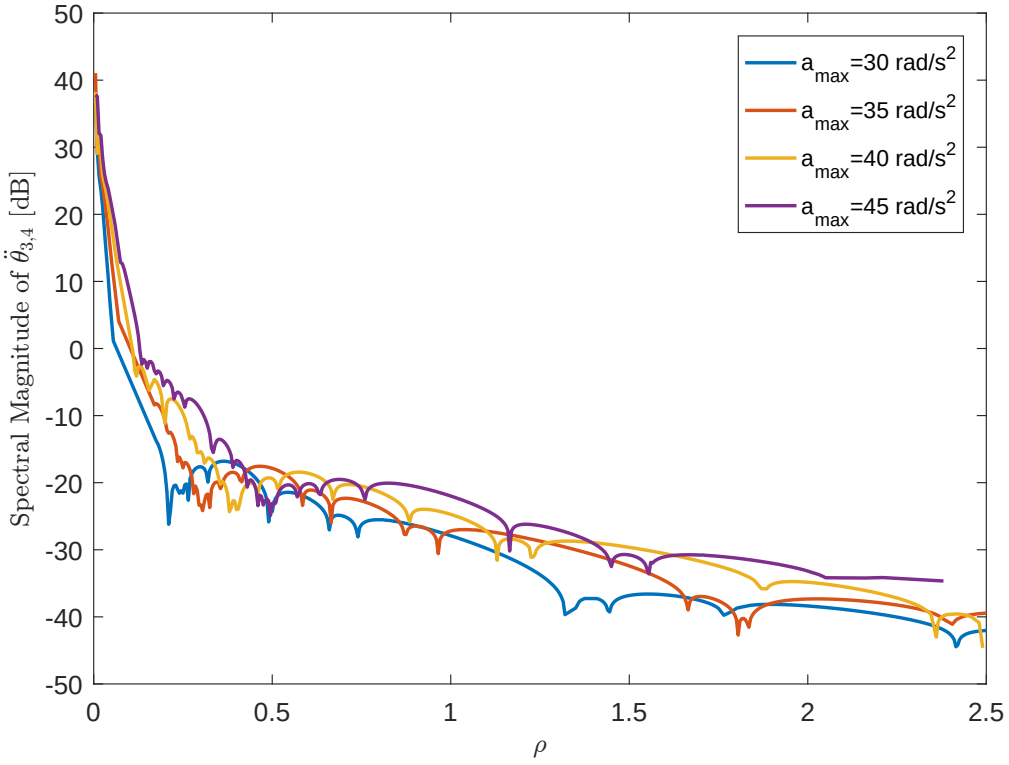

Figure 4.8. : Average Magnitude of Ramped Sinusoid Input Profile at 22 Selected Frequencies as a Function of ρ ($30 \leq a_{max} \leq 45$ rad/s^2).

ima as ρ increases. Such local minima suggest a local optimal profile with less residual vibrations than other ρ around this point. The effect of such local minima will be assessed carefully in Section 4.3.2.

Information from Figures 4.8 and 4.9 suggests that higher ρ would improve the performance, since lower $|F(\ddot{\theta}_{3,4})|$ implies less residual vibrations. Figure 4.10 gives the relationship between actuation time and ρ for each given peak input acceleration. For each value of peak input acceleration, the actuation time always increases with ρ, and for each ρ, the actuation time always decreases with peak input acceleration. Thus, the aforementioned argument is weakened and the trade-off between less resid-

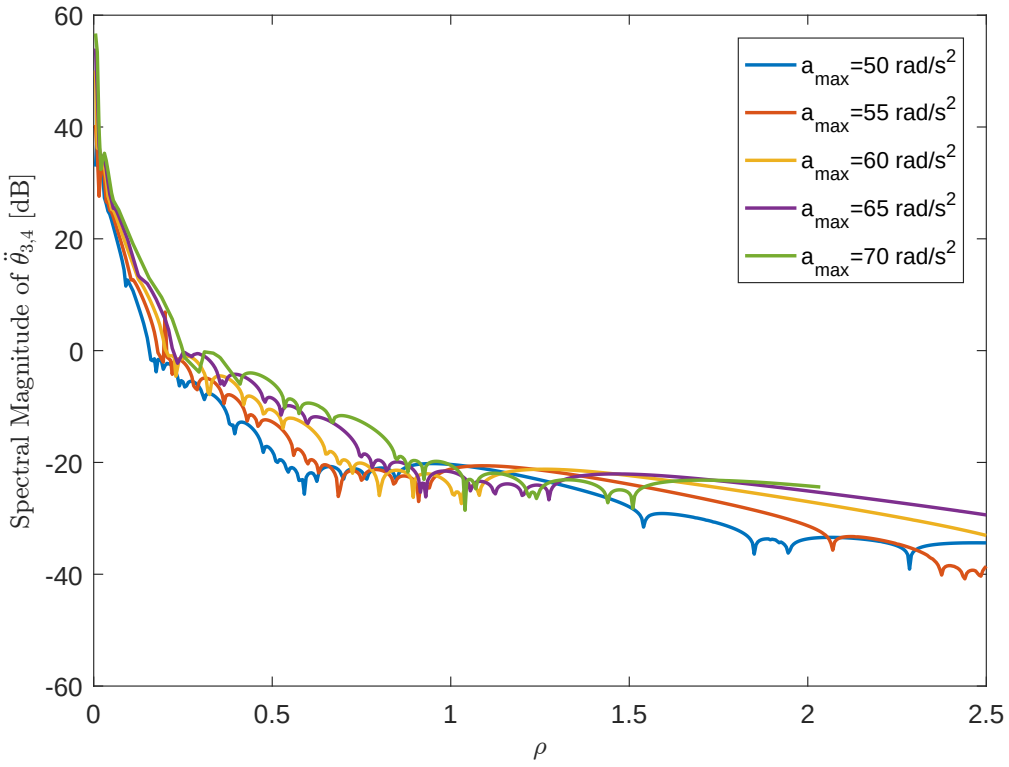

Figure 4.9. : Average Magnitude of Ramped Sinusoid Input Profile at 22 Selected Frequencies as a Function of ρ ($50 \leq a_{max} \leq 70$ rad/s^2).

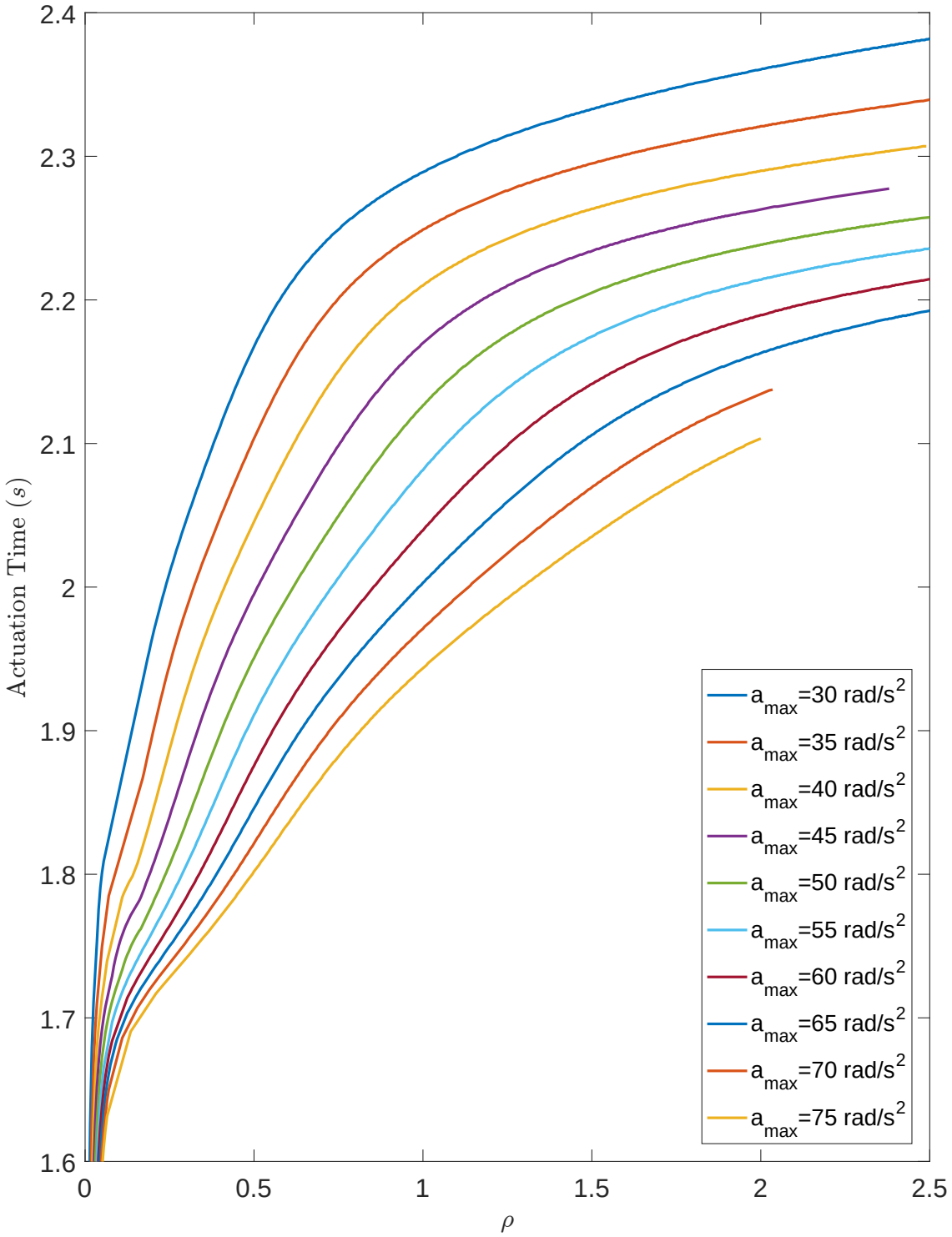

Figure 4.10. : Actuation Time as a Function of ρ with Ramped Sinusoid Functions.

ual vibrations and shorter actuation time needs to be weighted. This trade-off can be evaluated with the help of simulations discussed in Section 4.3.2.

4.3.2 Simulation of Robotic Arm

Analysis of input profiles constructed with the command shaping method utilizing ramped sinusoid functions confirms the command shaping method's ability to attenuate energy at selected frequencies. A Simulink model has been built to test the performance of the command shaping method with ramped sinusoid functions. As mentioned in Section 4.1, two important factors are amplitude of residual vibrations and settling time. The amplitude of residual vibrations is defined as the maximum of $|\overrightarrow{\ddot{OB}}|$ after the input profile ends. The settling time has been defined in Section 4.1. The total move time is defined as the summation of actuation time and the settling time.

Figures 4.11 and 4.12 show the relationship between total move time and ρ for each peak input acceleration. Total move time decreases with higher ρ for all peak input accelerations. Interestingly, total move time drops significantly at some ρ, instead of a smooth trend as for actuation time. After further investigation of the responses, the reason has been revealed. Since vibrations consist of multiple peaks and such peaks shift to earlier time and lower magnitude with higher ρ, when the last peak drops across the cutoff level, settling time will be determined by the earlier peak. As a result, settling time decreases significantly.

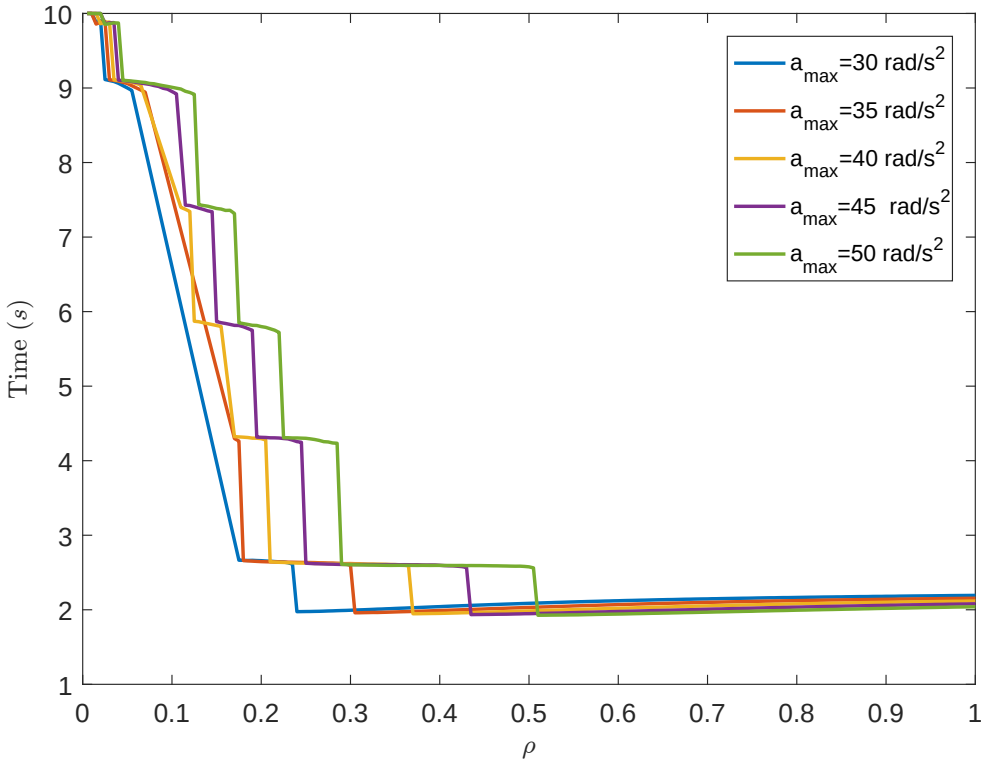

Figure 4.11. : Total Move Time as a Function of ρ with Ramped Sinusoid Functions.

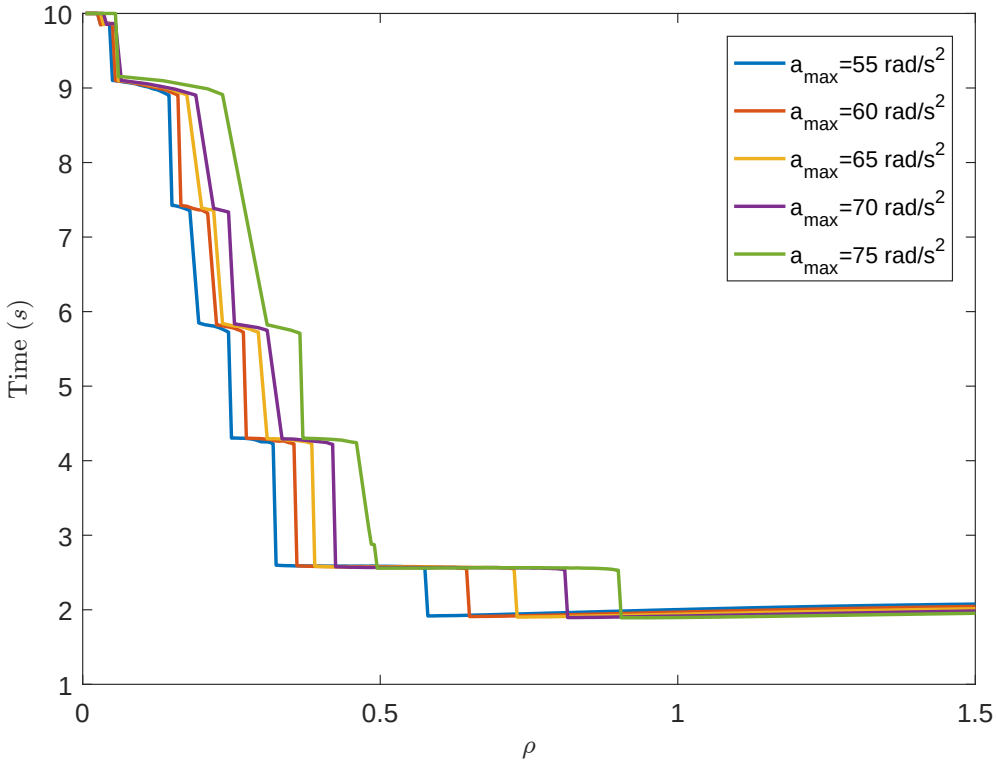

Figure 4.12. : Total Move Time as a Function of ρ with Ramped Sinusoid Functions.

Among all simulated profiles, there is one optimal combination of a_{max} and ρ for each a_{max} that gives the shortest total move time. Such profiles have a balance between good vibration reduction and acceptable time penalty, thus they will be validated on the physical robotic arm.

4.3.3 Experimental Validation

As simulations from Section 4.3.2 confirm that the command shaping with ramped sinusoid functions can effectively reduce residual vibrations, such method is worth validating on the physical robot. Thus, performance on the physical robot can be evaluated. Based on simulations, for each a_{max}, there is an optimal ρ giving the least total move time. All of such optimal cases are experimentally validated. Experimental results are averaged with 6 trials to minimize the effect of noise. Table 4.1 gives the detailed experimental results of all cases. Figure 4.13 summarizes all experimental results with total move time and actuation time for each input profile. Just with one glance, all experimental results outperformed their benchmark, as no case has its settling time longer than 0.2 seconds. Among these optimal profiles, total move time decreases with peak input acceleration. The benefit of higher peak input acceleration gets less significant, in other words, although settling time is decreasing, the amount of decrease is shrinking as well.

Figures 4.14 – 4.23 show the experimental results with settings included in corresponding captions. In each figure, [a] gives the desired input acceleration ($\ddot{\theta}_{3,4}$); [b] shows the frequency spectra of input acceleration; [c] gives the torques of the 1^{st}

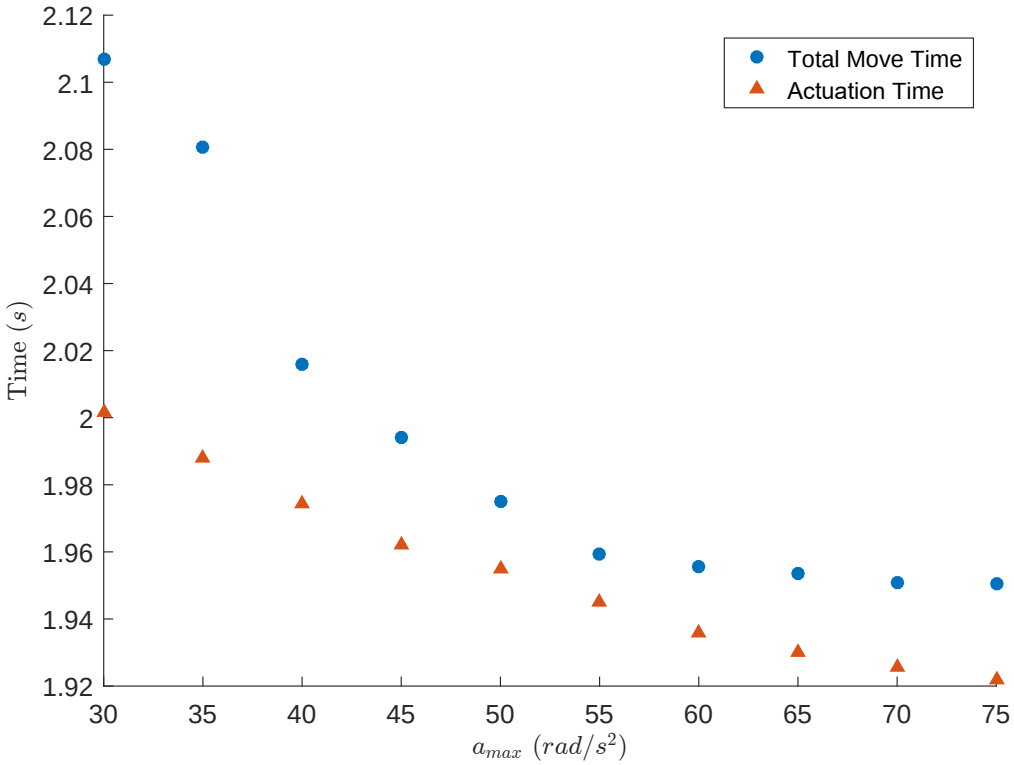

Figure 4.13. : Relationship between Settling Time, Actuation time and Peak Input Acceleration of Commanded Shaping Method with Ramped Sinusoid Functions.

Table 4.1. : Experimental Results of All Ramped Sinusoid Optimal Cases

a_{max} (rad/s^2)	ρ	Actuation Time (s)	Settling Time (s)	Total Move Time (s)
30	0.24	2.0015	0.1055	2.1070
35	0.305	1.9880	0.0925	2.0805
40	0.37	1.9745	0.0415	2.0160
45	0.435	1.9620	0.0320	1.9940
50	0.51	1.9550	0.0200	1.9750
55	0.58	1.9450	0.0145	1.9595
60	0.65	1.9360	0.0195	1.9555
65	0.73	1.9300	0.0235	1.9535
70	0.815	1.9255	0.0255	1.9510
75	0.905	1.9220	0.0285	1.9505

motor (T_1); [d] gives the torques of the 2^{nd} motor (T_2); [e] shows the desired and actual positions of the 1^{st} link (θ_1); [f] shows the desired and actual positions of the 2^{nd} link (θ_2); [g] shows the desired and actual positions of the 1^{st} motor (θ_3); [h] shows the desired and actual positions of the 2^{nd} motor (θ_4); [i] shows the actual angular accelerations of the 1^{st} link ($\ddot{\theta}_1$); and [j] shows the actual angular accelerations of the 2^{nd} link ($\ddot{\theta}_2$).

In all experimental results, energy around system natural frequencies has been successfully attenuated; energy around the second mode is attenuated more than that around the first mode; motors track the input well without steady-state error, and the 1^{st} link experiences more significant overshoot than the 2^{nd} link.

Looking at Figures 4.14 [a] and 4.23 [a], the peak input acceleration has been more than doubled, however, [c] and [d] of both figures show that the torques are not increased proportionally. As the torques are calculated in real time by the computed torque controller, this discrepancy can be ascribed to the feedback controller. In addition, input profiles change sharply at the transition between acceleration and deceleration, however, the actual torques only change a relatively small amount. As a result, the impact of feedback controller is more significant than expected and the relationship between actual torques and feedback controller needs to be studied.

Moreover, higher peak input acceleration also impairs the efficiency of the profile. In comparing the two most extreme profiles, when a_{max} is 30 rad/s^2, the acceleration of the 2^{nd} link only changed sign once, while that for $a_{max} = 75$ rad/s^2 changed sign three times. As a result, the 2^{nd} link has to decelerate during the course of acceleration.

This signified inefficiency can be explained by the time penalty factor (Γ). While the peak input acceleration has more than doubled from 30 rad/s^2, actuation time of these profiles does not vary a lot. As a result, the penalty factor has more than doubled.

As ρ increases from 0.24 to 0.905, the input profile gets less similar to a bang-bang profile. This matches the expectation of the higher priority on energy attenuation than approximating a bang-bang profile.

4.4 Versine

After the command shaping method with ramped sinusoid function has been proved to work as expected, the same analysis has been performed with versine functions.

4.4.1 Commanded Profile Analysis

This time, the velocity of each input profile is limited to 6 rad/s. This value is calculated from a 2 s bang-bang profile that has been used as benchmark. As a result, if two segments alone would not drive the motors to travel to the end-point, a constant velocity segment would be added between acceleration and deceleration. Apparently, the constant velocity segment in not needed in all profiles.

Figure 4.24 presents a typical commanded versine input profile with position, velocity and acceleration as reference. This input profile is constructed with $a_{max} = 45$

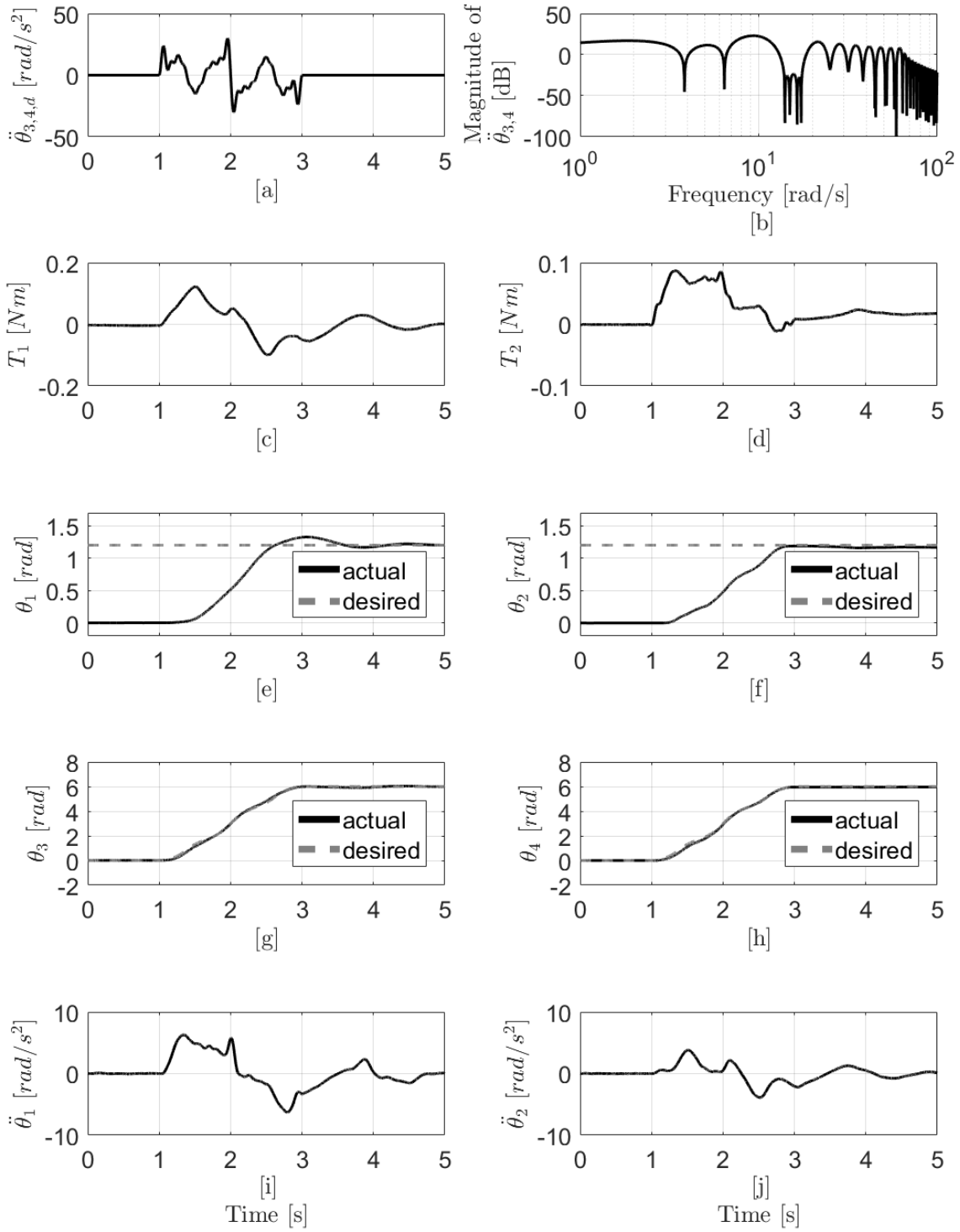

Figure 4.14. : Experimental Data of Ramped Sinusoid Function with $a_{max} = 30$ rad/s^2 and $\rho = 0.24$.

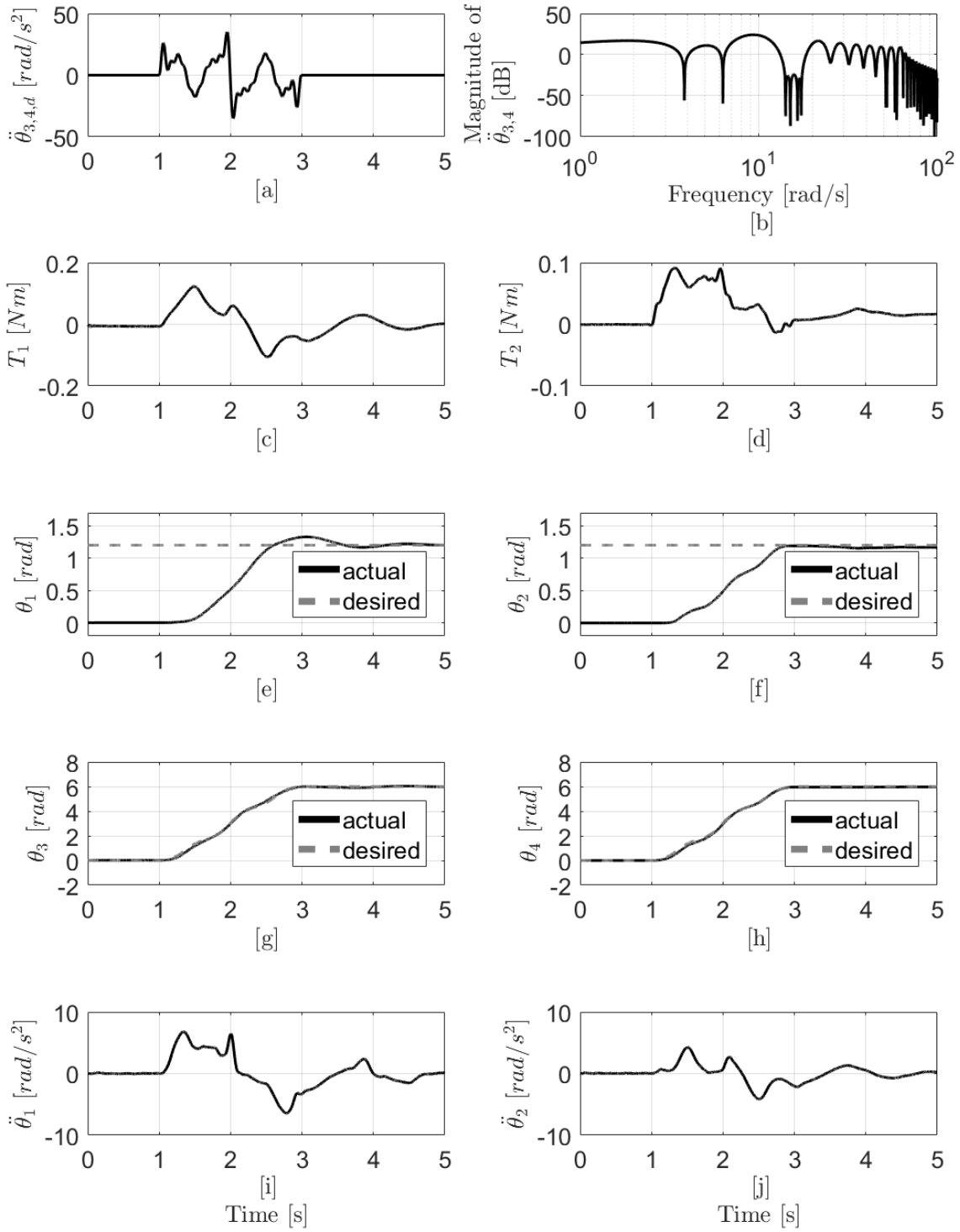

Figure 4.15. : Experimental Data of Ramped Sinusoid Function with $a_{max} = 35$ rad/s^2 and $\rho = 0.305$.

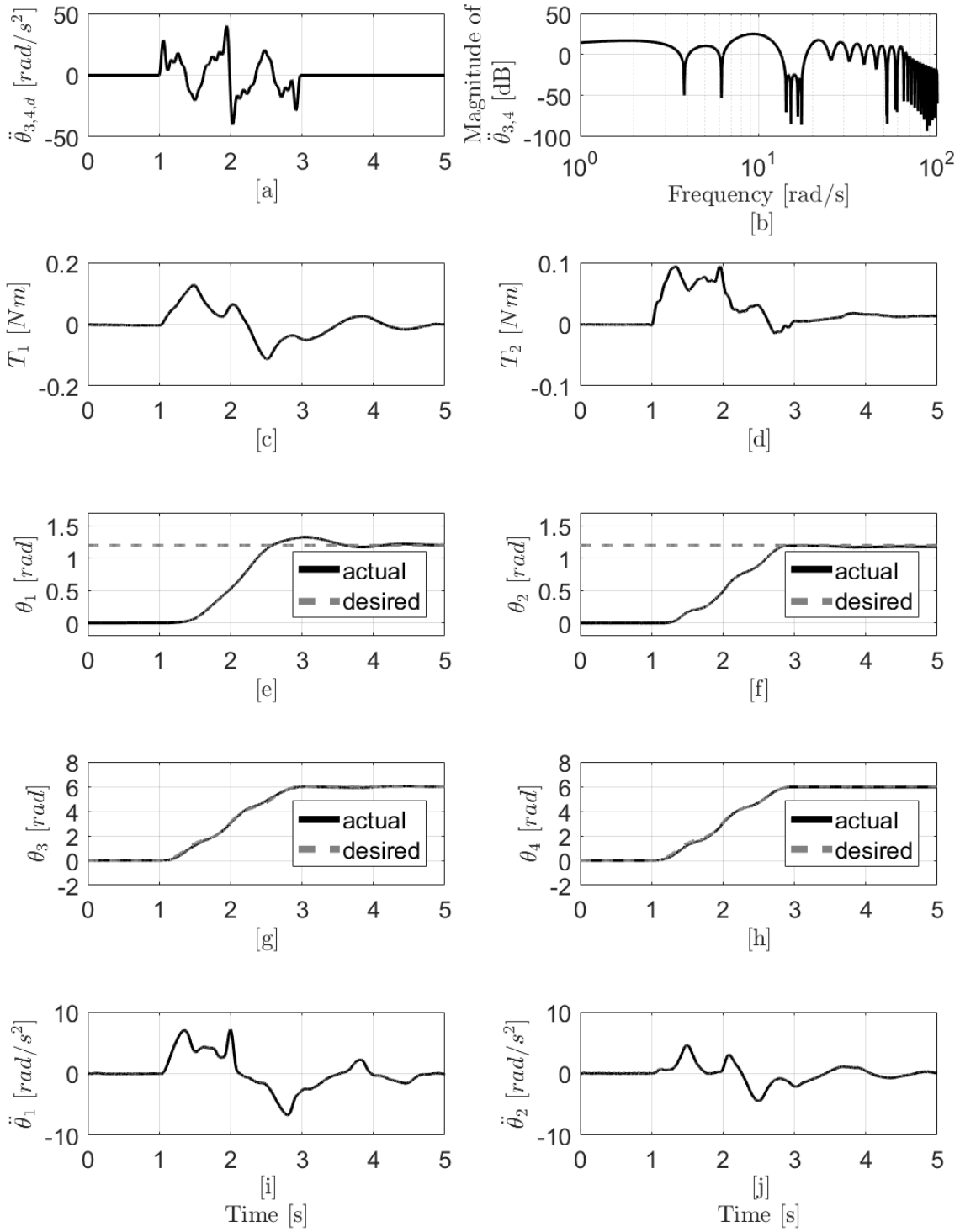

Figure 4.16. : Experimental Data of Ramped Sinusoid Function with $a_{max} = 40$ rad/s^2 and $\rho = 0.37$.

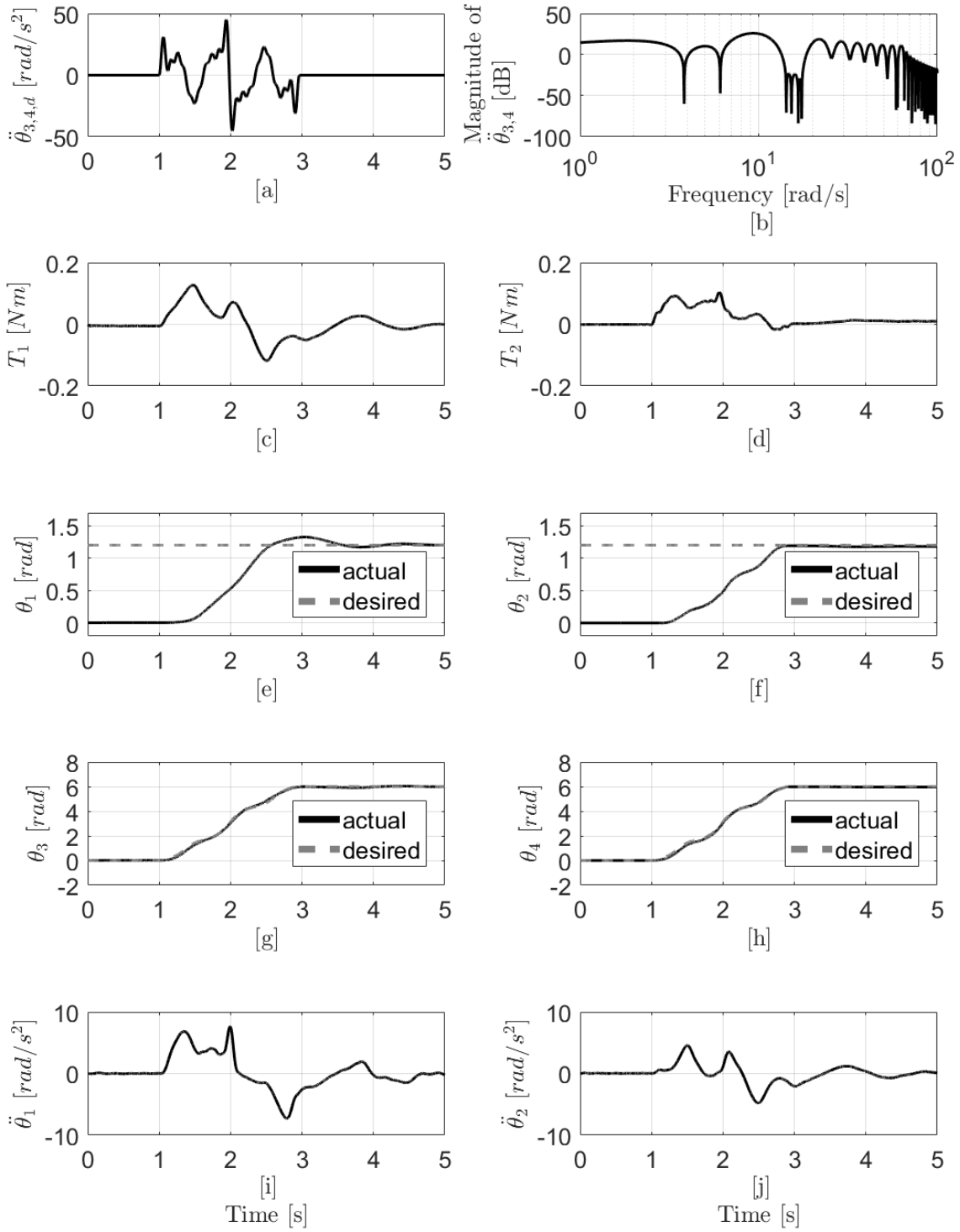

Figure 4.17. : Experimental Data of Ramped Sinusoid Function with $a_{max} = 45$ rad/s^2 and $\rho = 0.435$.

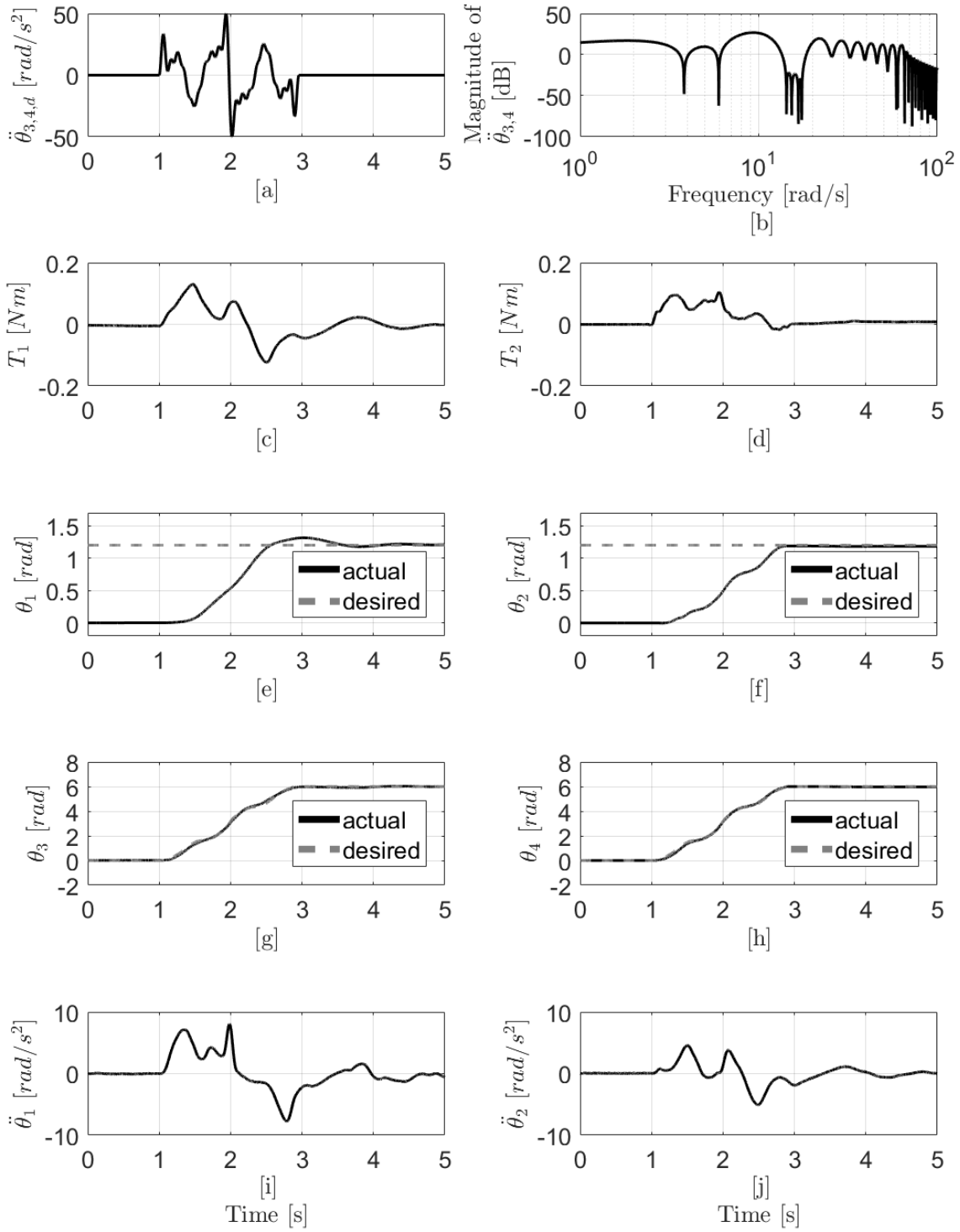

Figure 4.18. : Experimental Data of Ramped Sinusoid Function with $a_{max} = 50$ rad/s^2 and $\rho = 0.51$.

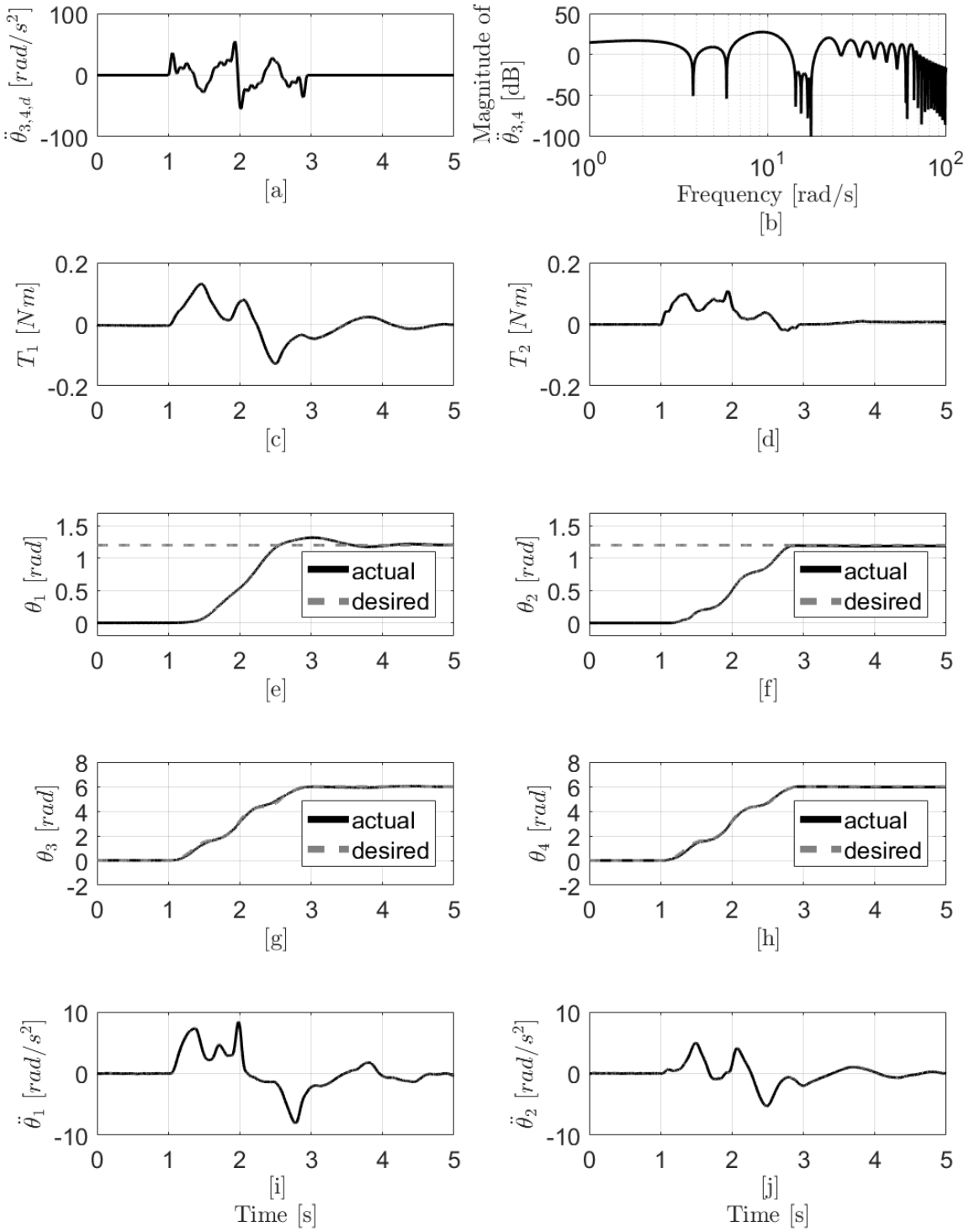

Figure 4.19. : Experimental Data of Ramped Sinusoid Function with $a_{max} = 55$ rad/s^2 and $\rho = 0.58$.

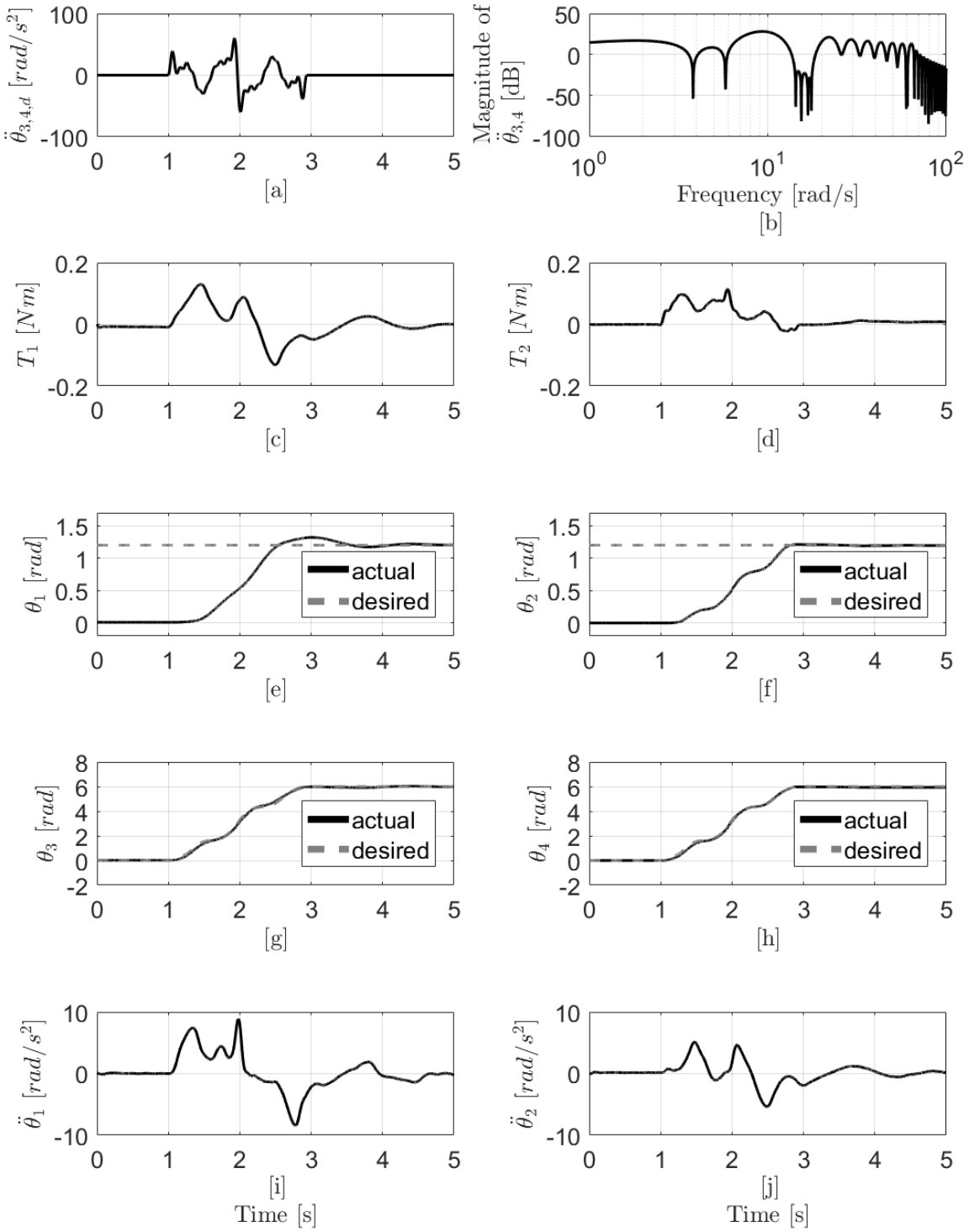

Figure 4.20. : Experimental Data of Ramped Sinusoid Function with $a_{max} = 60$ rad/s^2 and $\rho = 0.65$.

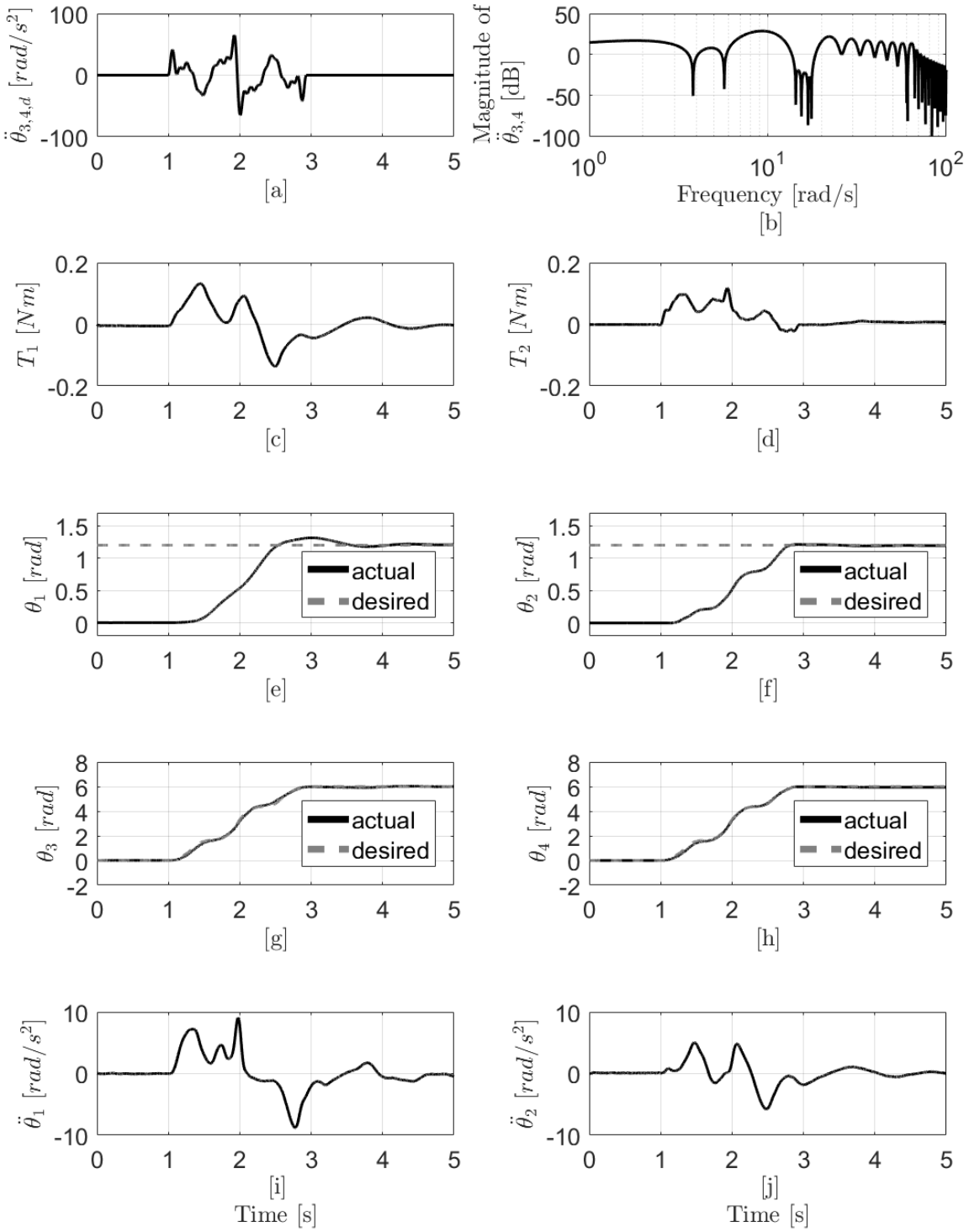

Figure 4.21. : Experimental Data of Ramped Sinusoid Function with $a_{max} = 65$ rad/s^2 and $\rho = 0.73$.

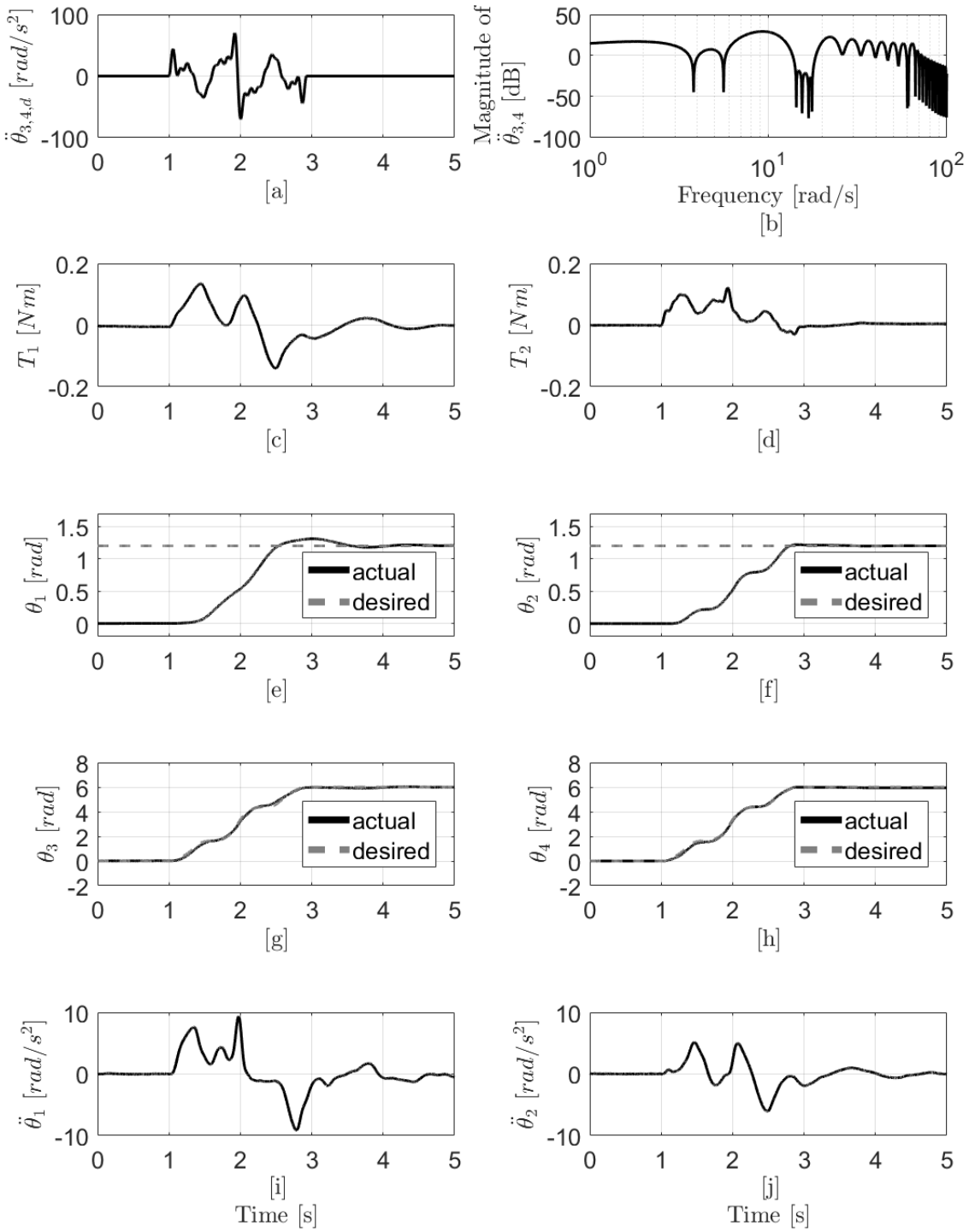

Figure 4.22. : Experimental Data of Ramped Sinusoid Function with $a_{max} = 70$ rad/s^2 and $\rho = 0.815$.

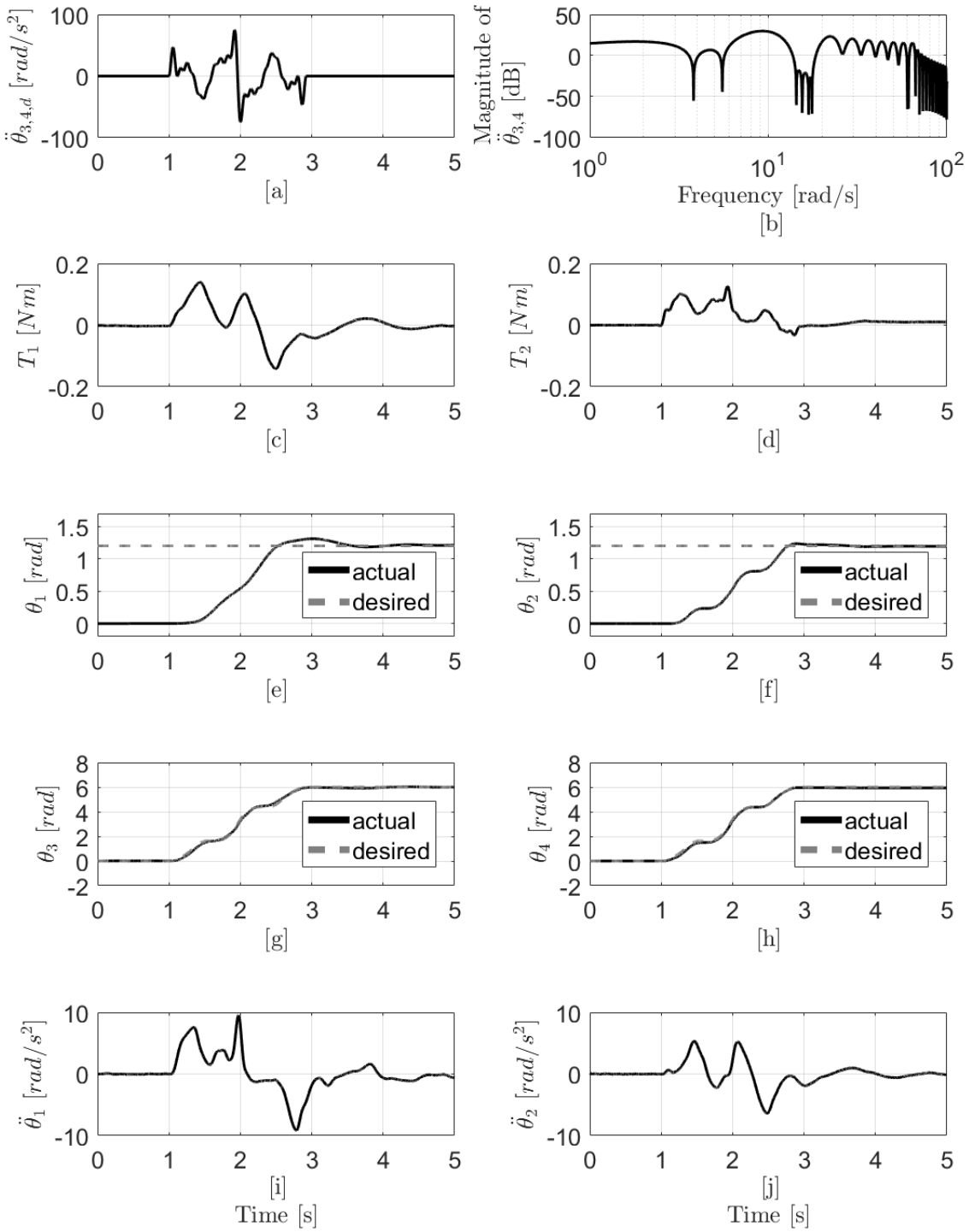

Figure 4.23. : Experimental Data of Ramped Sinusoid Function with $a_{max} = 75$ rad/s^2 and $\rho = 0.905$.

rad/s^2 and $\rho = 2.5$. It has three segments: acceleration, constant velocity and deceleration. In order to minimize vibrations, acceleration has to change sign during either acceleration or deceleration, which shows the inefficiency of the command shaping method over the bang-bang profile. Figure 4.25 shows the frequency spectrum of the same profile. Since the two segments are independent of each other, they are plotted separately. The figure shows that the command shaping method has successfully attenuated energy around both system frequencies in both segments. Besides the attenuated energy, the wide region of frequencies with attenuated energy suggests a good tolerance for modeling error.

Figures 4.26 to 4.28 are the plots of $|F(\ddot{\theta}_{3,4})|$ as a function of ρ with corresponding peak input acceleration. Since each complete versine profile consists of two independent segments, one acceleration segment and one deceleration segment, two curves are plotted in each figure. The black curve is the average of $|F(\ddot{\theta}_{3,4})|$ at 22 selected frequencies during accelerating, while the red curve represents the same parameter during decelerating. All these plots confirm that the average spectral magnitude of input profiles at selected frequencies is monotonically decreasing with ρ. In other words, higher ρ suggests less residual vibration. In addition, these figures also show that for the same ρ, average energy at selected frequencies would be higher with higher peak input acceleration. This is due to the higher energy level introduced with higher acceleration.

For a good profile, residual vibrations need to be minimized, and short time is preferred as well. Figures 4.29 – 4.31 present the relationship between actuation

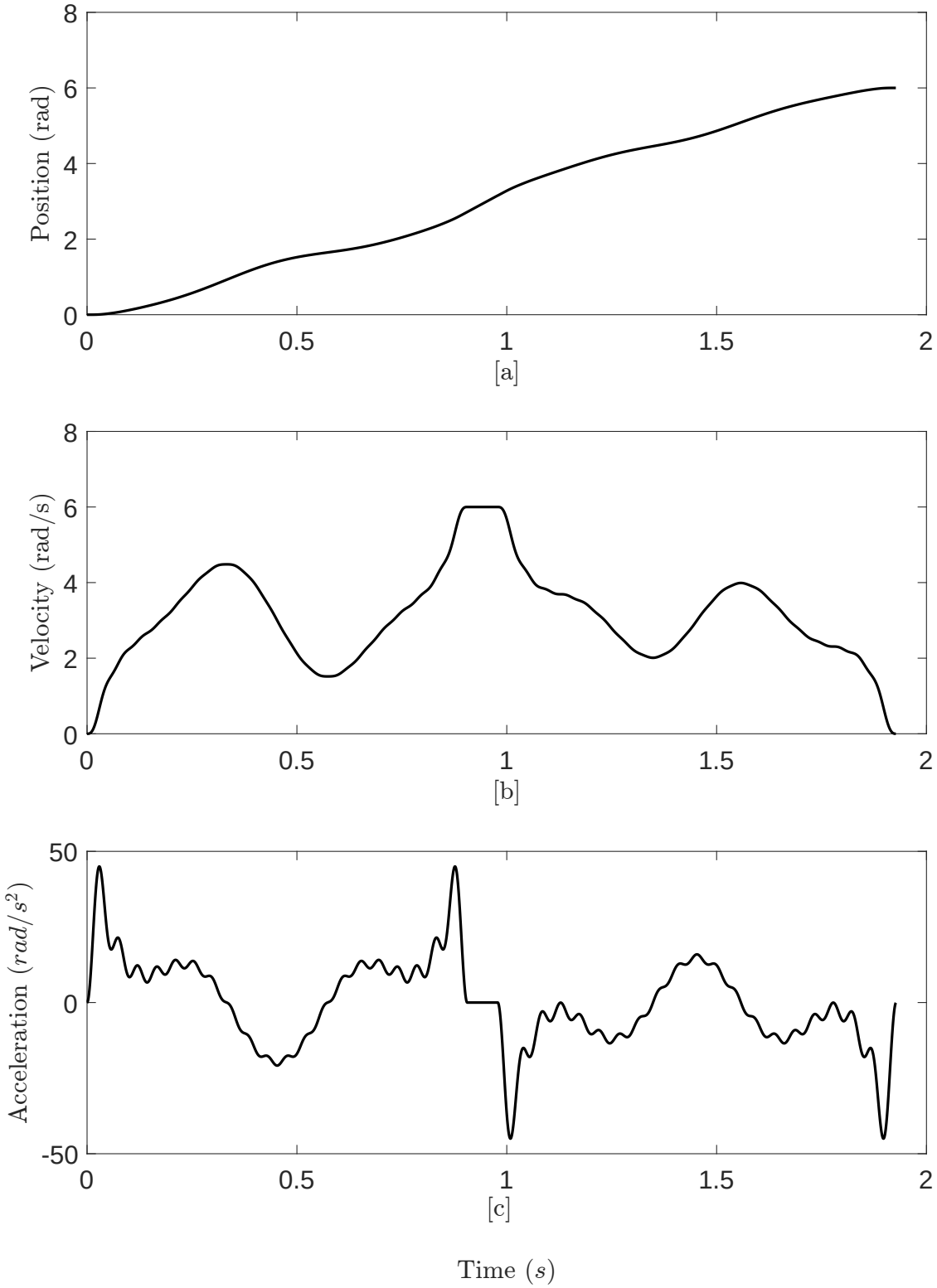

Figure 4.24. : Input Profile with $a_{max} = 45$ rad/s^2 and $\rho = 2.5$.

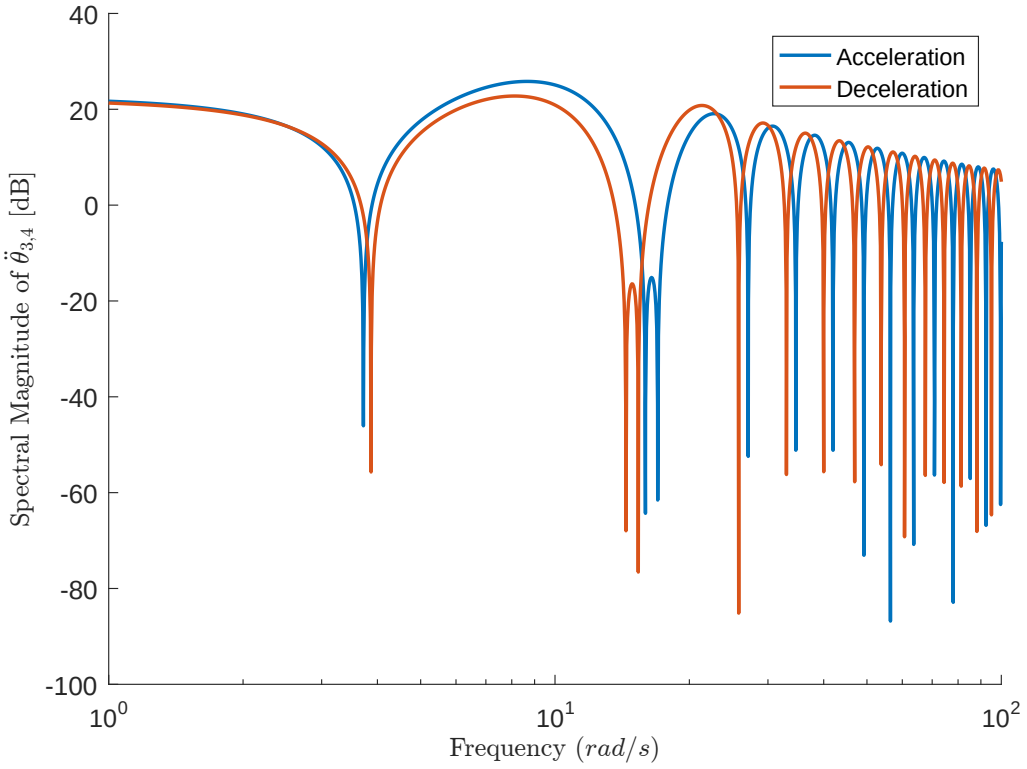

Figure 4.25. : Frequency Spectrum of Input Profile with $a_{max} = 45$ rad/s^2 and $\rho = 2.5$.

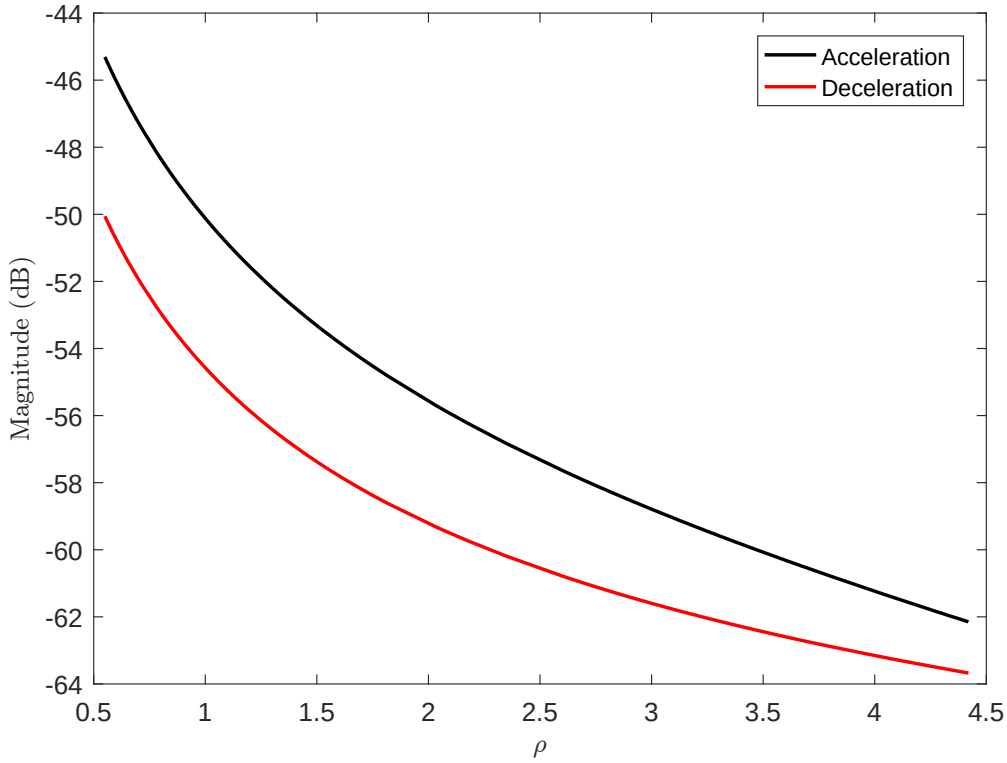

Figure 4.26. : Effect of ρ on Spectral Magnitude when a_{max} is 30 rad/s^2 with Versine Functions.

time and ρ for corresponding peak input acceleration. Actuation time monotonically increases with ρ if the profile has the same peak input acceleration, according to such figures. As for commanded profiles with ramped sinusoid function, smaller peak input acceleration guarantees shorter actuation time with same ρ. Thus, trade-off between less vibrations and shorter time has to be weighted before reaching a decision of good ρ with given a_{max}.

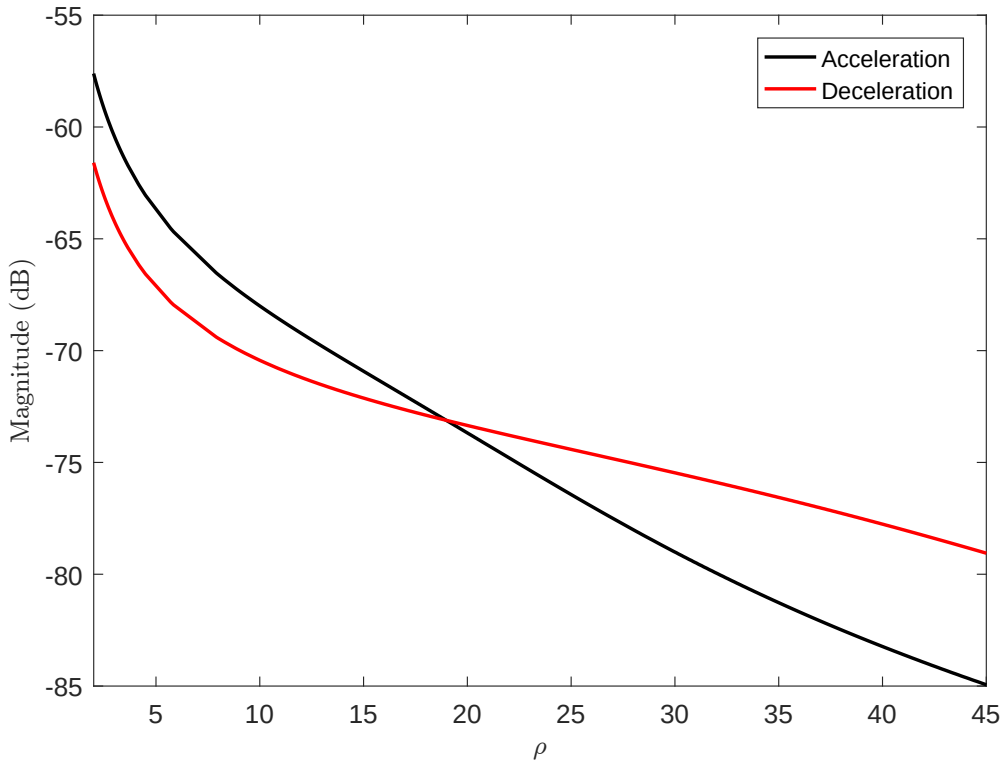

Figure 4.27. : Effect of ρ on Spectral Magnitude when a_{max} is 50 rad/s^2 with Versine Functions.

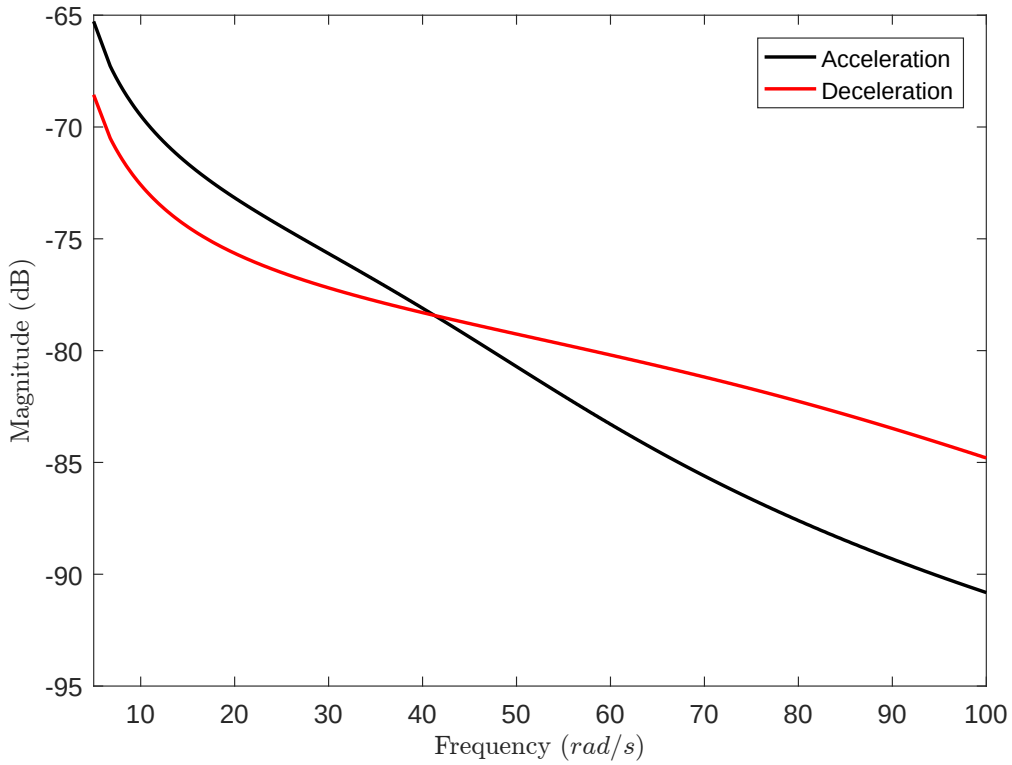

Figure 4.28. : Effect of ρ on Spectral Magnitude when a_{max} is 75 rad/s^2 with Versine Functions.

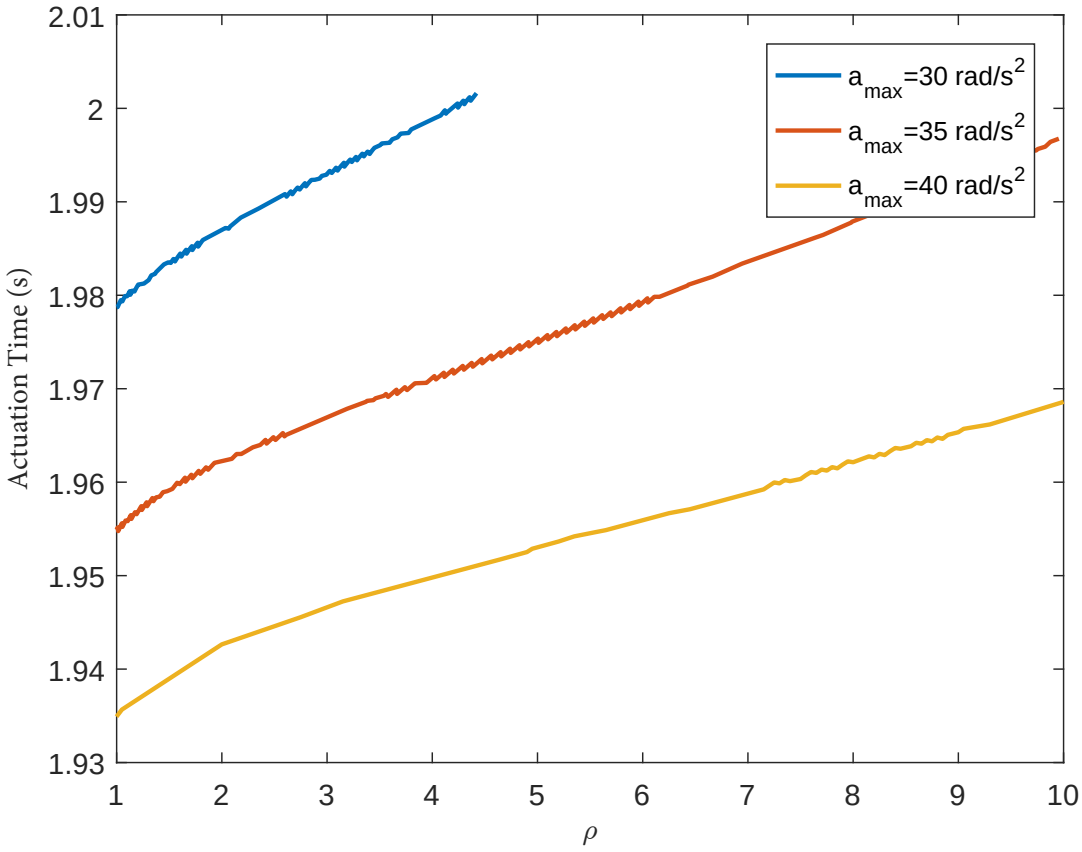

Figure 4.29. : Actuation Time of Versine Function with $a_{max} = 30$ rad/s^2, $a_{max} = 35$ rad/s^2 and $a_{max} = 40$ rad/s^2.

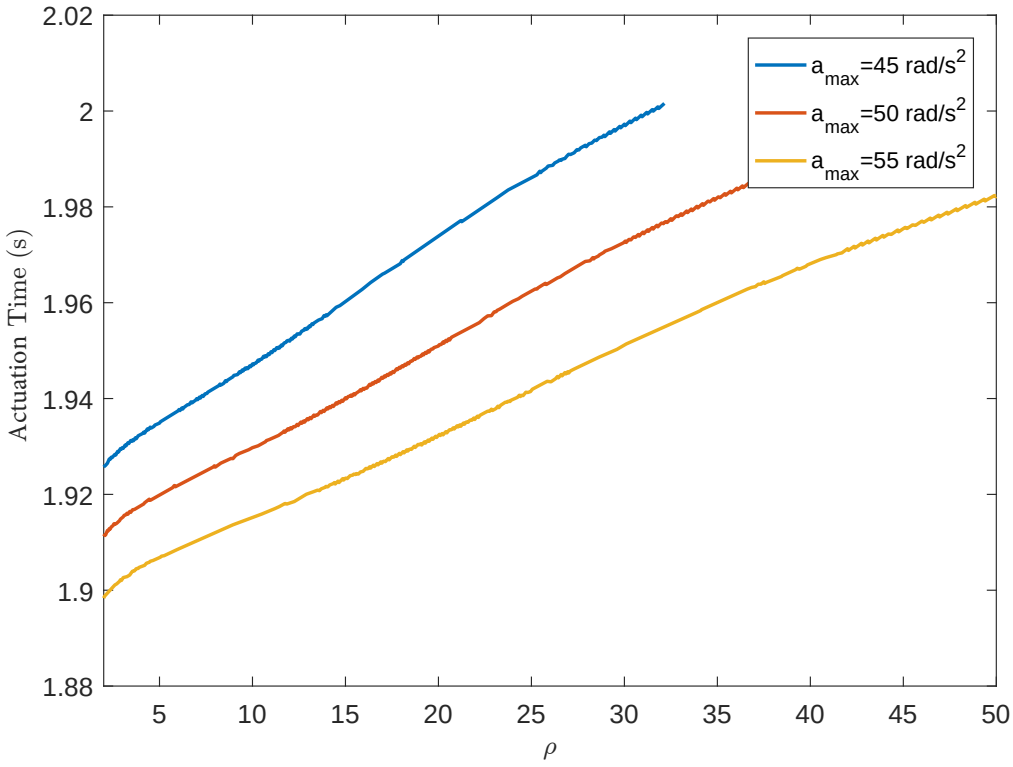

Figure 4.30. : Actuation Time of Versine Function with $a_{max} = 45$ rad/s^2, $a_{max} = 50$ rad/s^2 and $a_{max} = 55$ rad/s^2.

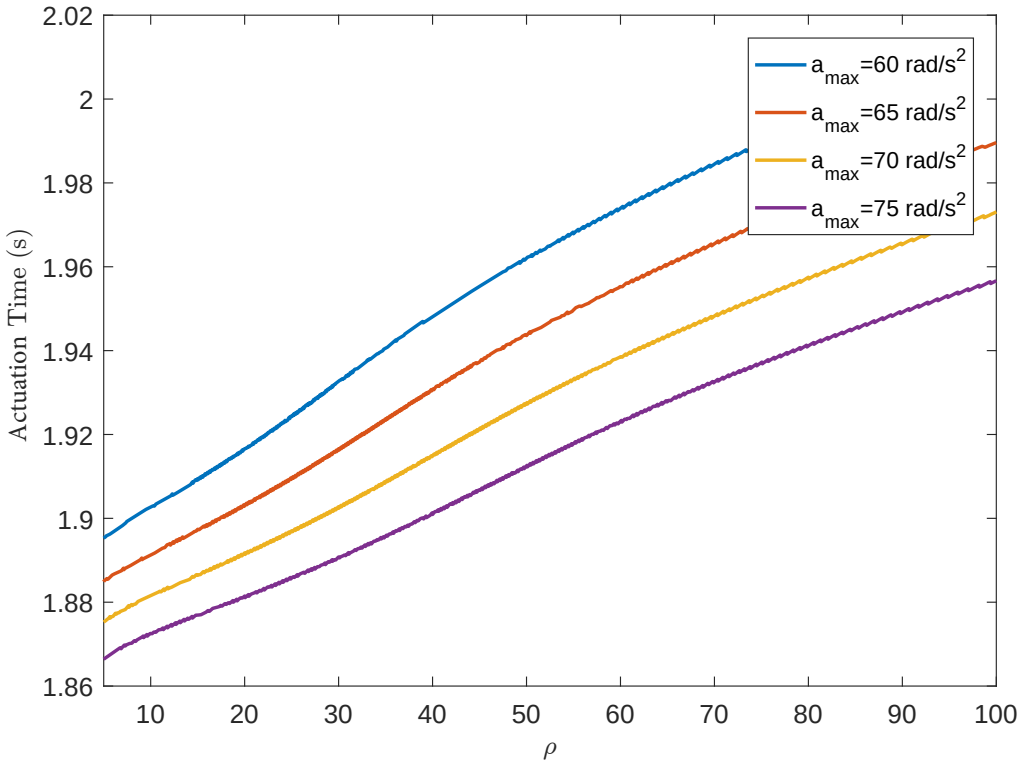

Figure 4.31. : Actuation Time of Versine Function with $a_{max} = 60$ rad/s^2, $a_{max} = 65$ rad/s^2, $a_{max} = 70$ rad/s^2 and $a_{max} = 75$ rad/s^2.

4.4.2 Simulation of Robotic Arm

Since the analysis of input profiles constructed with the command shaping method utilizing versine functions confirms the command shaping method's ability to attenuate energy at selected frequencies, the same procedure as in Section 4.3.2 has been followed to examine the performance of the command shaping method with versine functions.

Figures 4.32 – 4.34 show how peak residual vibration amplitude and settling time are affected by ρ. The range of ρ is part of the complete dataset in that ρ outside this range gives either not enough attenuation or too much attenuation resulting in zero settling time. Both peak residual vibration amplitude and settling time decrease with ρ when peak input acceleration remains the same. Moreover, these figures also tell the strong correlation between peak residual vibrations and duration of residual vibrations. As a result, either metric would indicate if a profile gives good performance. However, total move time is chosen as the unified parameter for comparing all profiles, because it takes both residual vibrations and the inefficiency of profiles into account. In addition, residual vibrations are stronger with higher peak input acceleration when ρ remains the same.

Figures 4.35 and 4.36 present the relationship between the total move time and ρ for each peak input acceleration. Total move time drops with higher ρ as expected. As for simulations with ramped sinusoid functions, the total move does not drop smoothly with increasing ρ. Thus, an optimal combination of a_{max} and ρ can be

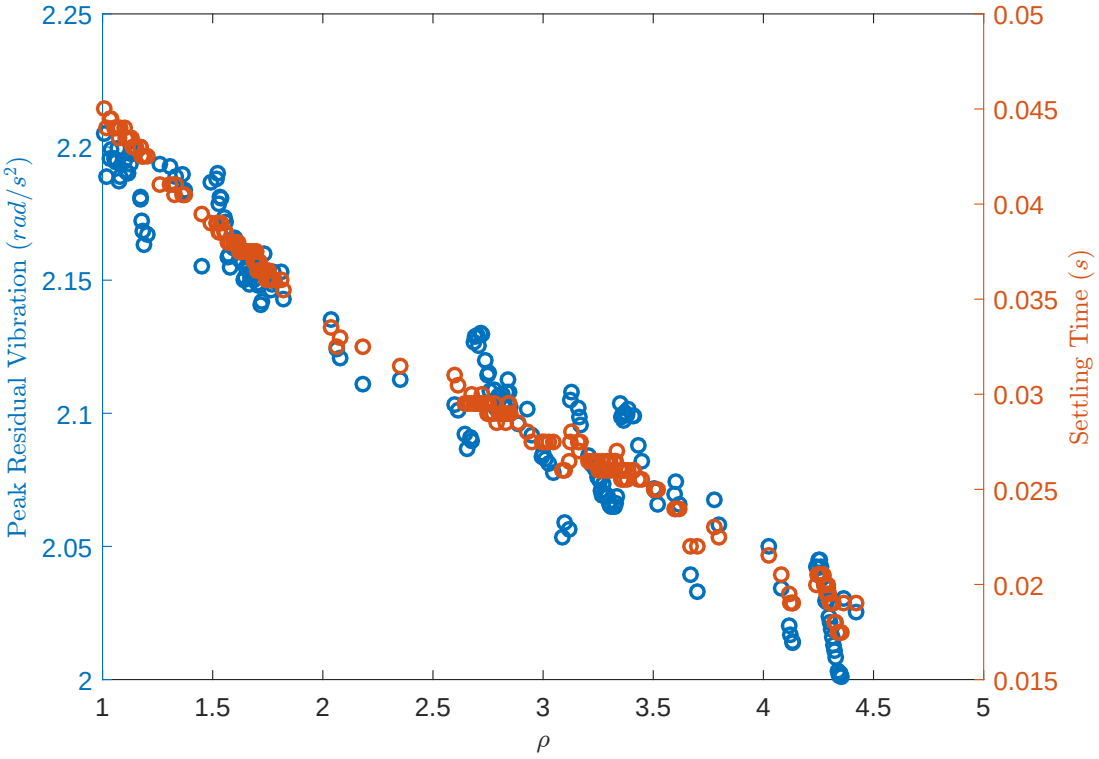

Figure 4.32. : Relationship between Peak Residual Vibration Amplitude, Settling Time and ρ when $a_{max} = 30$ rad/s^2 with Versine Functions.

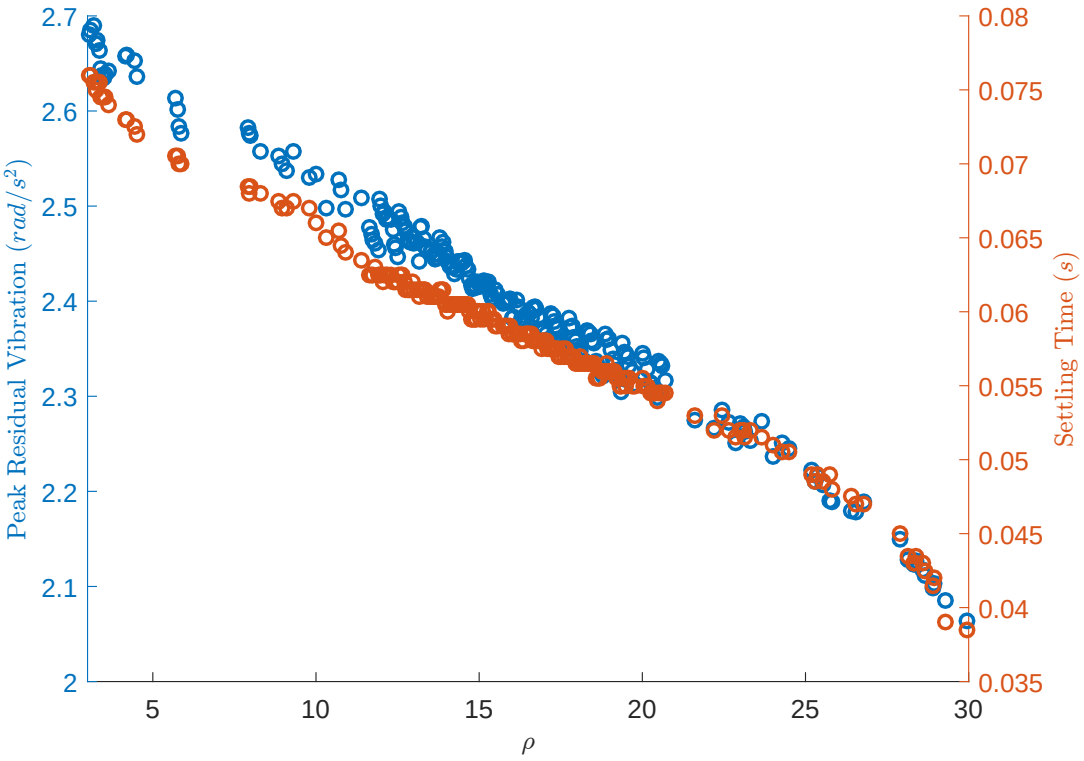

Figure 4.33. : Relationship between Peak Residual Vibration Amplitude, Settling Time and ρ when $a_{max} = 50$ rad/s^2 with Versine Functions.

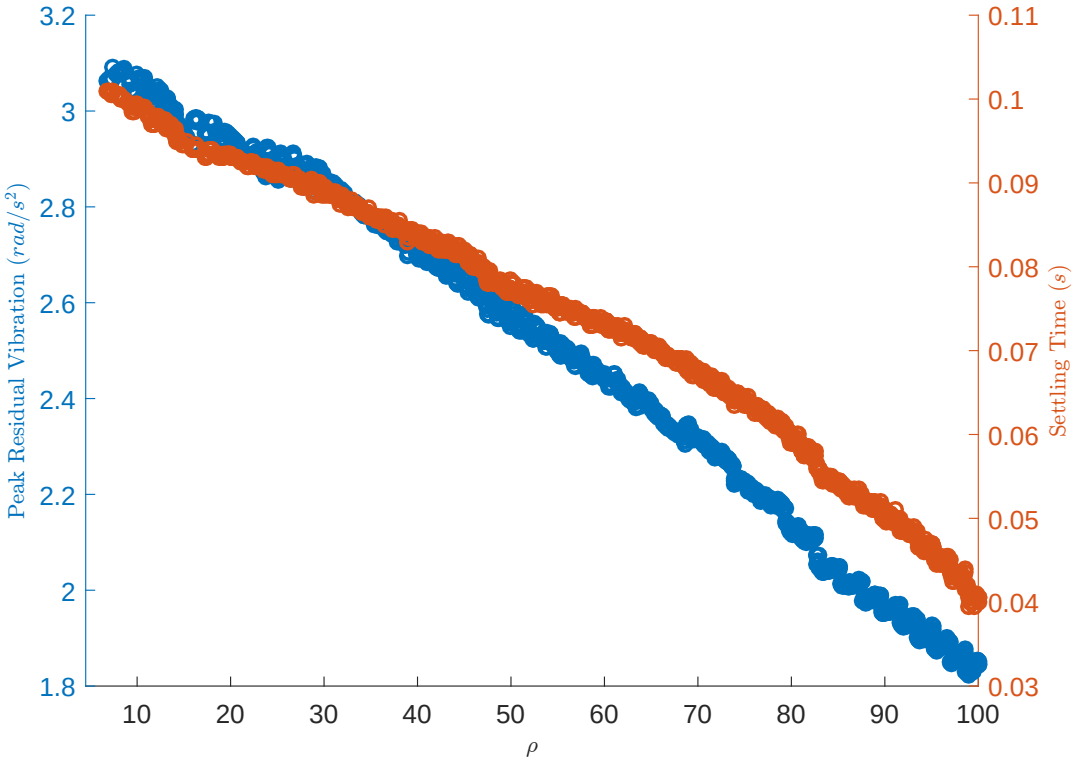

Figure 4.34. : Relationship between Peak Residual Vibration Amplitude, Settling Time and ρ when $a_{max} = 75$ rad/s^2 with Versine Functions.

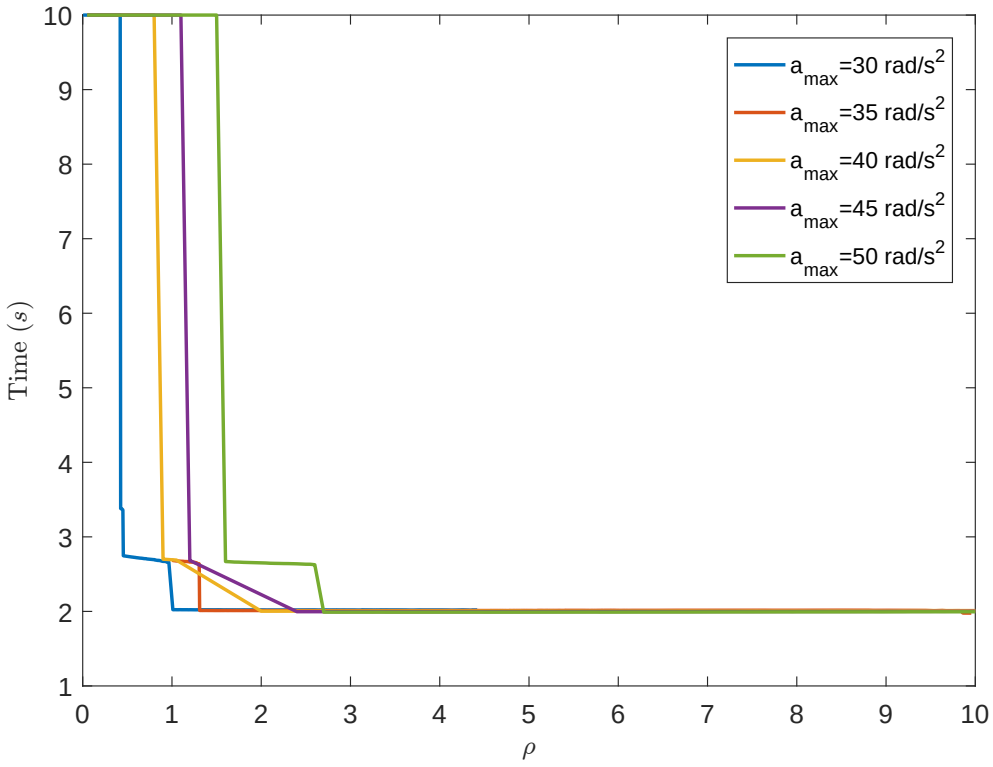

Figure 4.35. : Total Move Time of Versine Function with $a_{max} = 30$ rad/s^2, $a_{max} = 35$ rad/s^2, $a_{max} = 40$ rad/s^2, $a_{max} = 45$ rad/s^2 and $a_{max} = 50$ rad/s^2.

found to balance between residual vibration reduction and time penalty. Such profiles will be experimentally validated on the physical robotic arm.

4.4.3 Experimental Validation

The same procedure as for Section 4.3.3 has been followed to validate the command shaping method with versine functions on the physical robotic arm.

All experimental results of versine optimal cases are given in Table 4.2. Figure 4.37 gives the relationship between total move time, actuation time and peak input

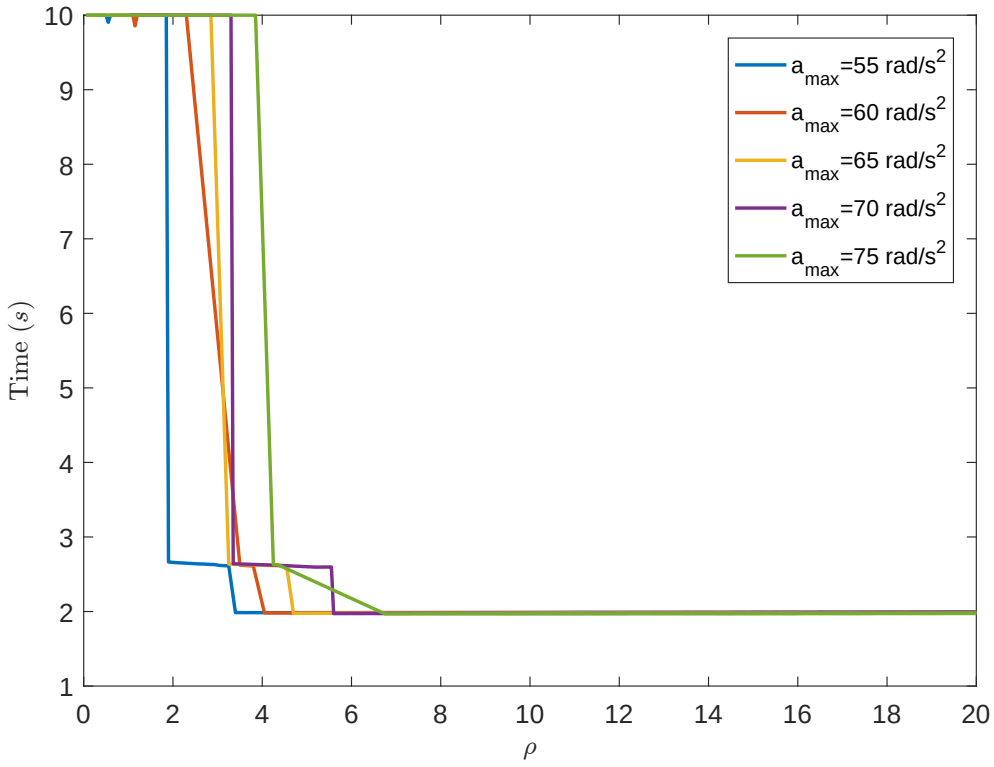

Figure 4.36. : Total Move Time of Versine Function with $a_{max} = 55$ rad/s^2, $a_{max} = 60$ rad/s^2, $a_{max} = 65$ rad/s^2, $a_{max} = 70$ rad/s^2 and $a_{max} = 75$ rad/s^2.

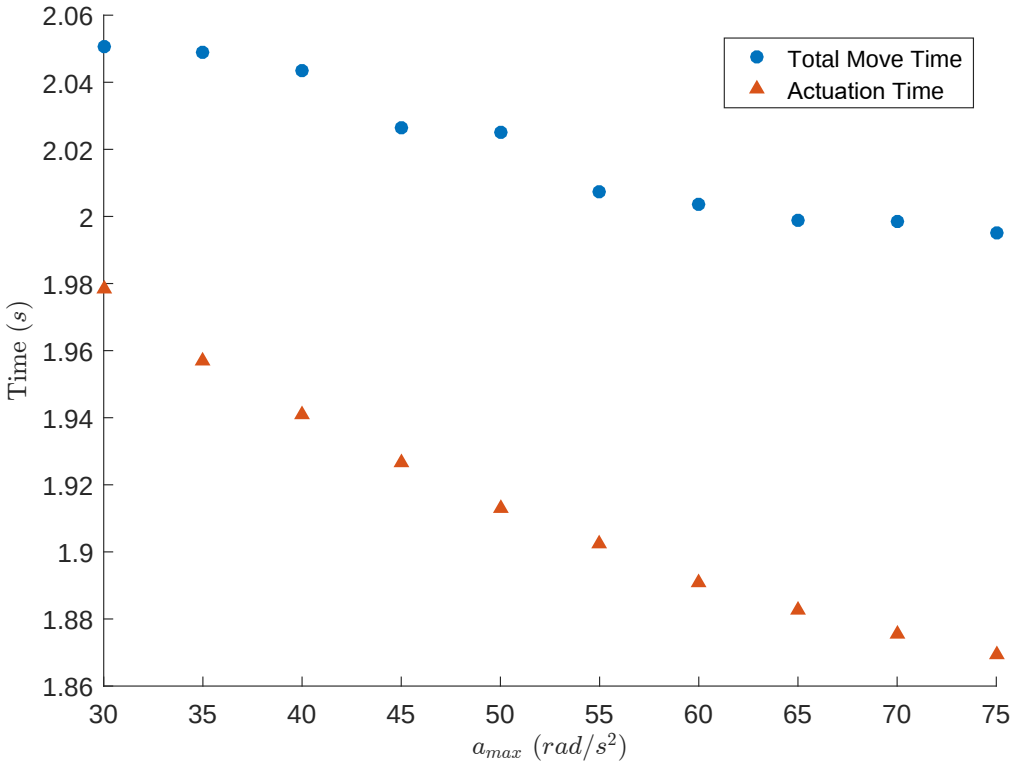

Figure 4.37. : Relationship between Settling Time, Actuation Time and Peak Input Acceleration of Commanded Shaping Method with Versine Functions.

Table 4.2. : Experimental Results of All Versine Optimal Cases

a_{max} (rad/s^2)	ρ	Actuation Time (s)	Settling Time (s)	Total Move Time (s)
30	1.1	1.9785	0.0720	2.0505
35	1.35	1.9570	0.0920	2.0490
40	2	1.9410	0.1025	2.0435
45	2.5	1.9265	0.1000	2.0265
50	2.7	1.9130	0.1120	2.0250
55	3.4	1.9025	0.1050	2.0075
60	3.5	1.8910	0.1125	2.0035
65	4.5	1.8825	0.1165	1.9990
70	6	1.8755	0.1230	1.9985
75	8	1.8695	0.1255	1.9950

acceleration. The same trend can be found as that with ramped sinusoid functions. The total move time of any profile is less than 2.06 seconds, while the benchmarked bang-bang profile needs 5.2985 seconds to reach the same state. For all experimental results, the total move time decreases with higher a_{max}, while the settling time increases a bit. This is due to the unavoidable noise and the way that settling time is defined. Thus, settling time is very sensitive to the acceleration signals around the threshold. In addition, total move time of profiles with versine functions has less variation than that with ramped sinusoid functions.

Figures 4.38 – 4.47 show the experimental results for the corresponding versine profiles, which follow the same layout as those with ramped sinusoid functions. Although the constant velocity segment exists in all profiles, the duration of that segment is very short. The peak acceleration is achieved at the beginning and the end of one segment, while the accelerations are far away from their limit in between two peaks. Furthermore, all input profiles present the change of sign in the middle of one segment, which shows the inefficiency of the command shaping method due to the focus on vibration reduction.

Even though the input profiles change sharply during the last peak of acceleration segment and the first peak of deceleration segment, the torque signals do not change proportionally. This suggests that there are other components affecting torques. Although energy around system natural frequencies has been successfully attenuated, it is noticeably higher than profiles with the same peak input acceleration using ramped sinusoid functions. This results from the fundamental difference of ρ in the two basis functions. The profile with versine functions is the summation of two segments, in which the frequencies with attenuated energy are slightly different. Although the energy at the selected frequencies is low, it is then offset by the other segment. As a result, it looks like the energy in the profiles with versine functions is significantly higher. However, the ideal range of ρ is different for each basis function to ensure the same level of energy attenuation. Moreover, the same level of energy attenuation does not guarantee the same level of performance if the basis functions are different.

Both motors track input profiles very well without noticeable difference between actual signals and input signals. The 1^{st} link has more overshoot than the 2^{nd} link, which is the same as what happens to profiles with ramped sinusoid functions. By looking at Figures 4.23 and 4.47, the response with ramped sinusoid functions has higher torques, higher link accelerations and changed direction of acceleration three times. The benefit of separating acceleration and deceleration is that no backward motion would exist even with very inefficient profile. The maximum torques on both links with versine profiles tend to be lower than those with ramped sinusoid profiles.

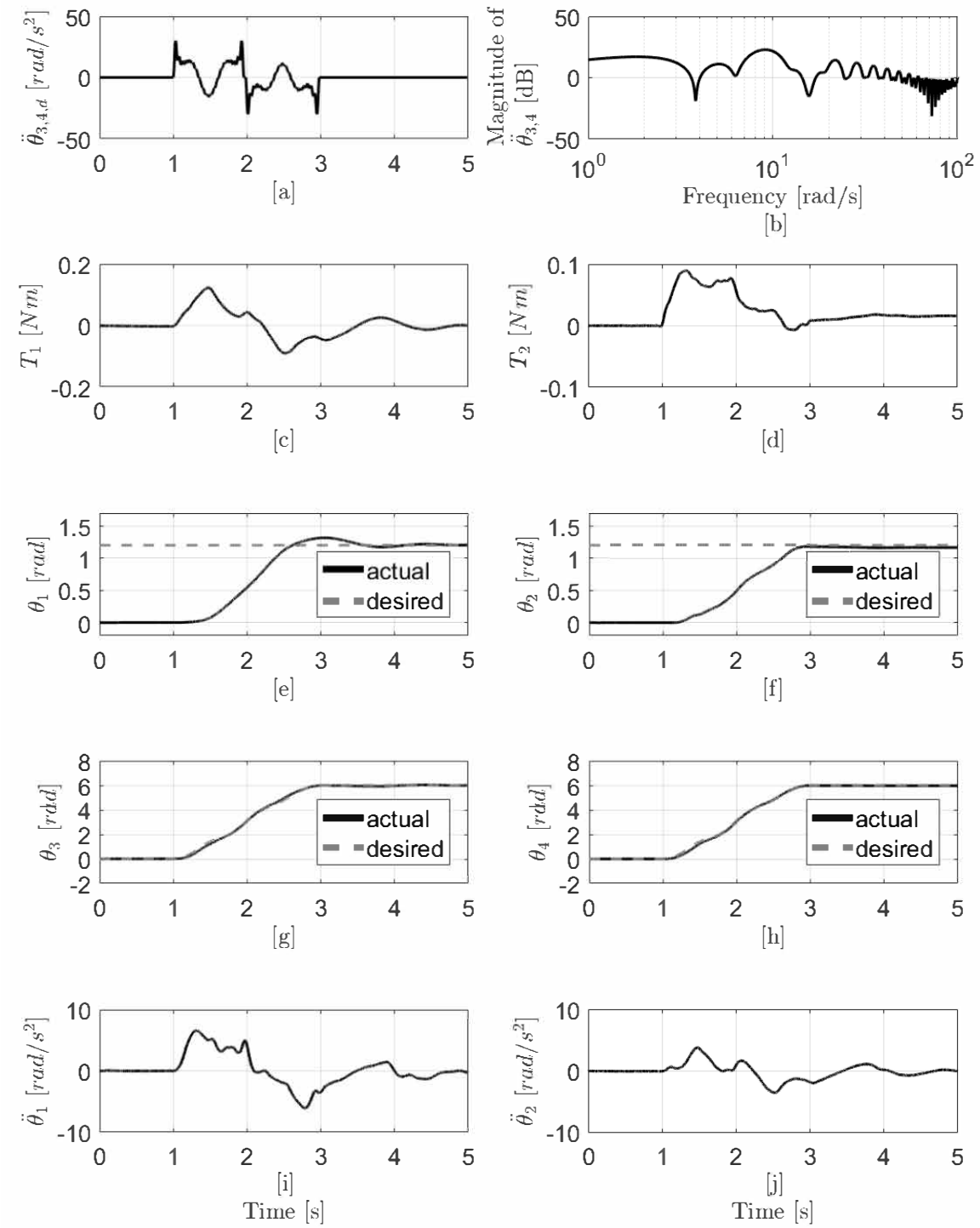

Figure 4.38. : Experimental Data of Versine Function with a_{max} = 30 rad/s^2 and $\rho = 1.1$.

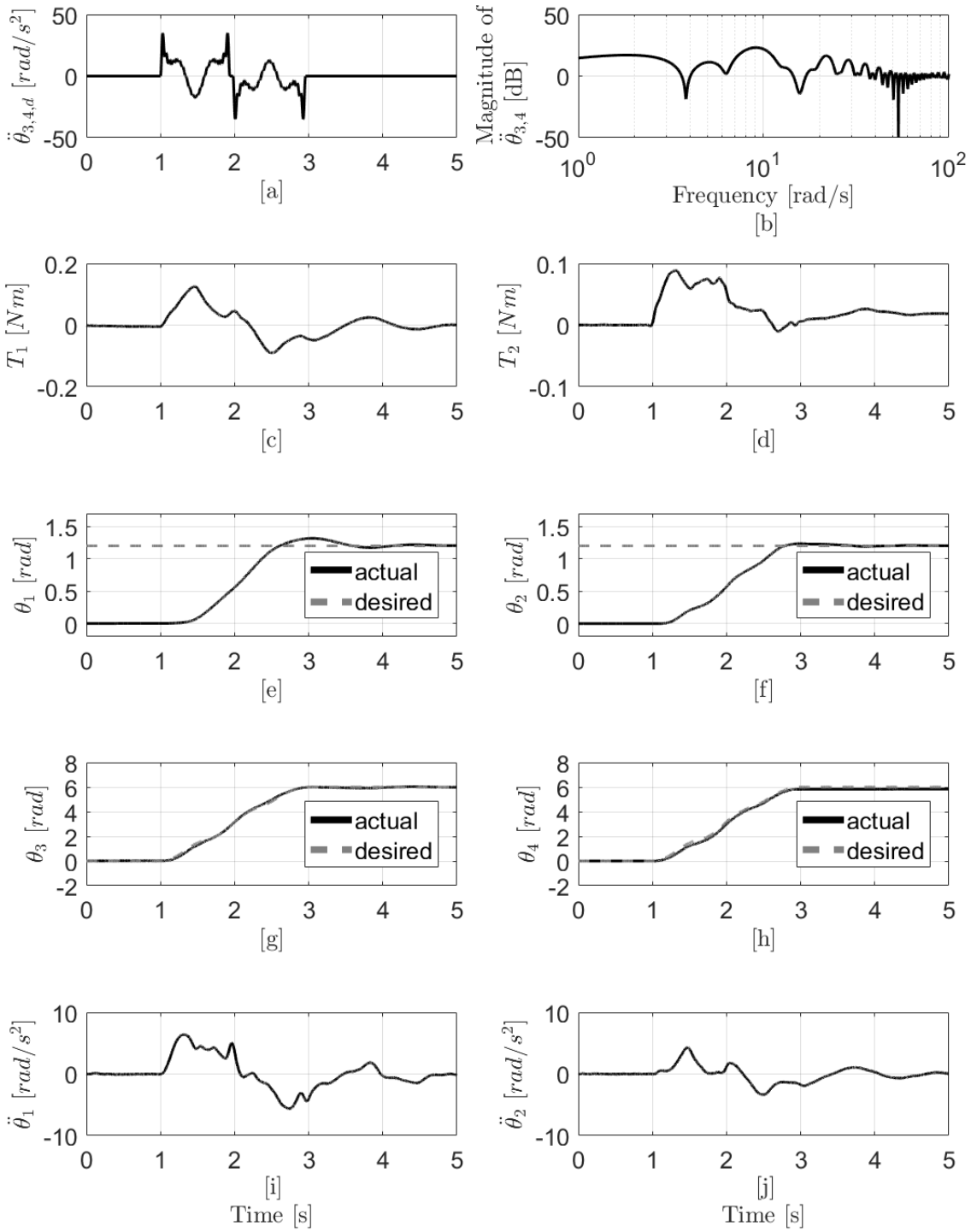

Figure 4.39. : Experimental Data of Versine Function with a_{max} = 35 rad/s^2 and $\rho = 1.35$.

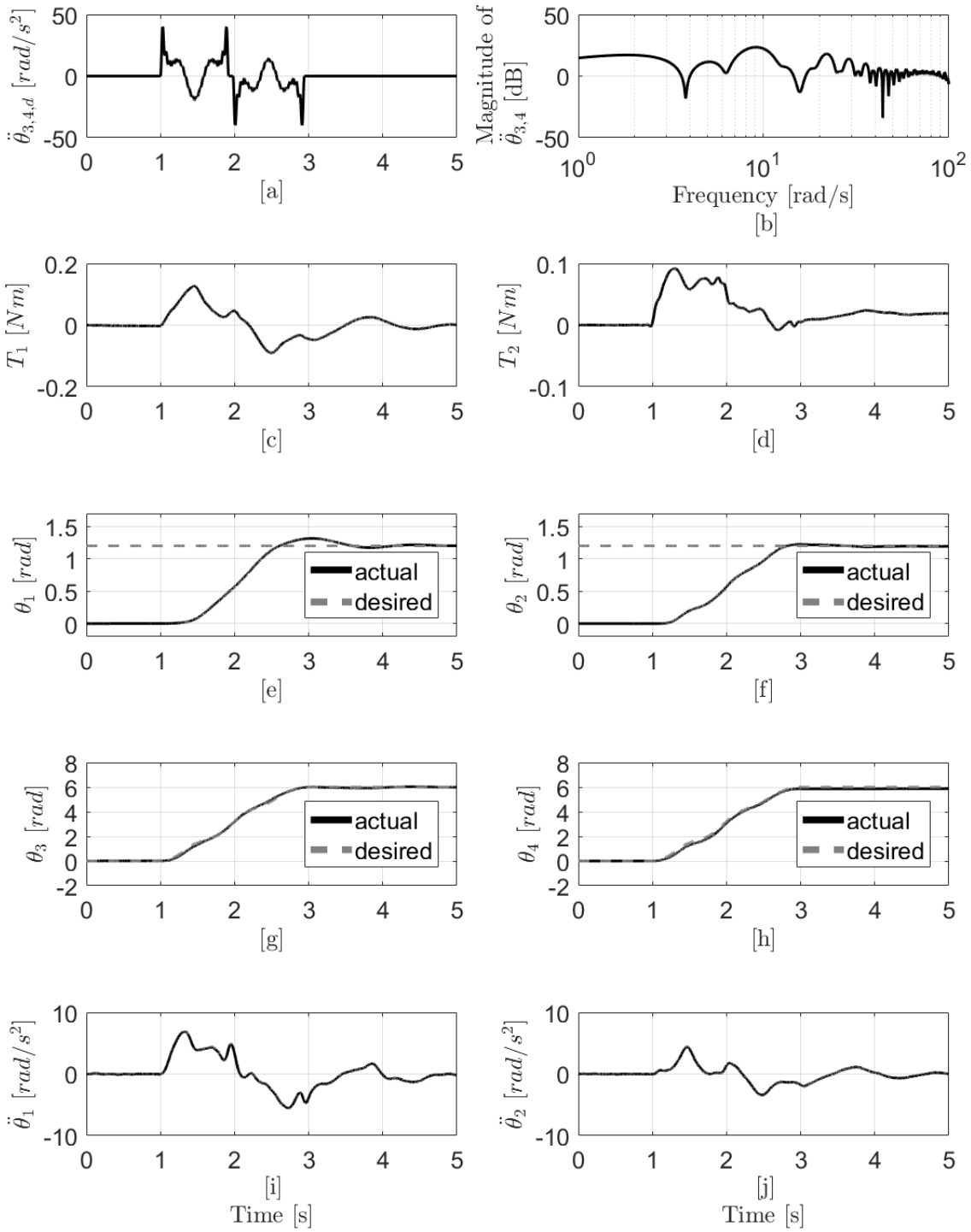

Figure 4.40. : Experimental Data of Versine Function with $a_{max} = 40$ rad/s^2 and $\rho = 2$.

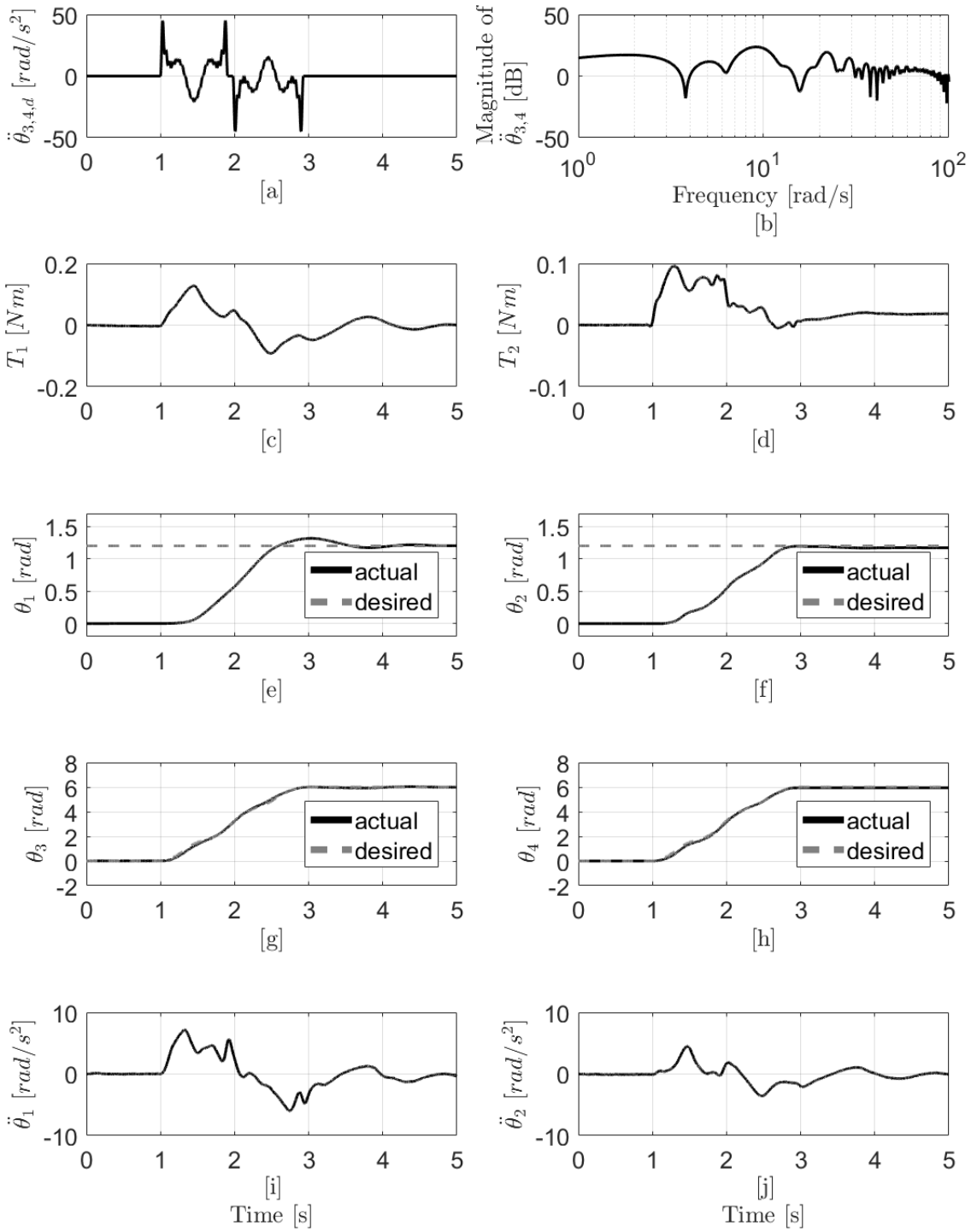

Figure 4.41. : Experimental Data of Versine Function with $a_{max} = 45$ rad/s^2 and $\rho = 2.5$.

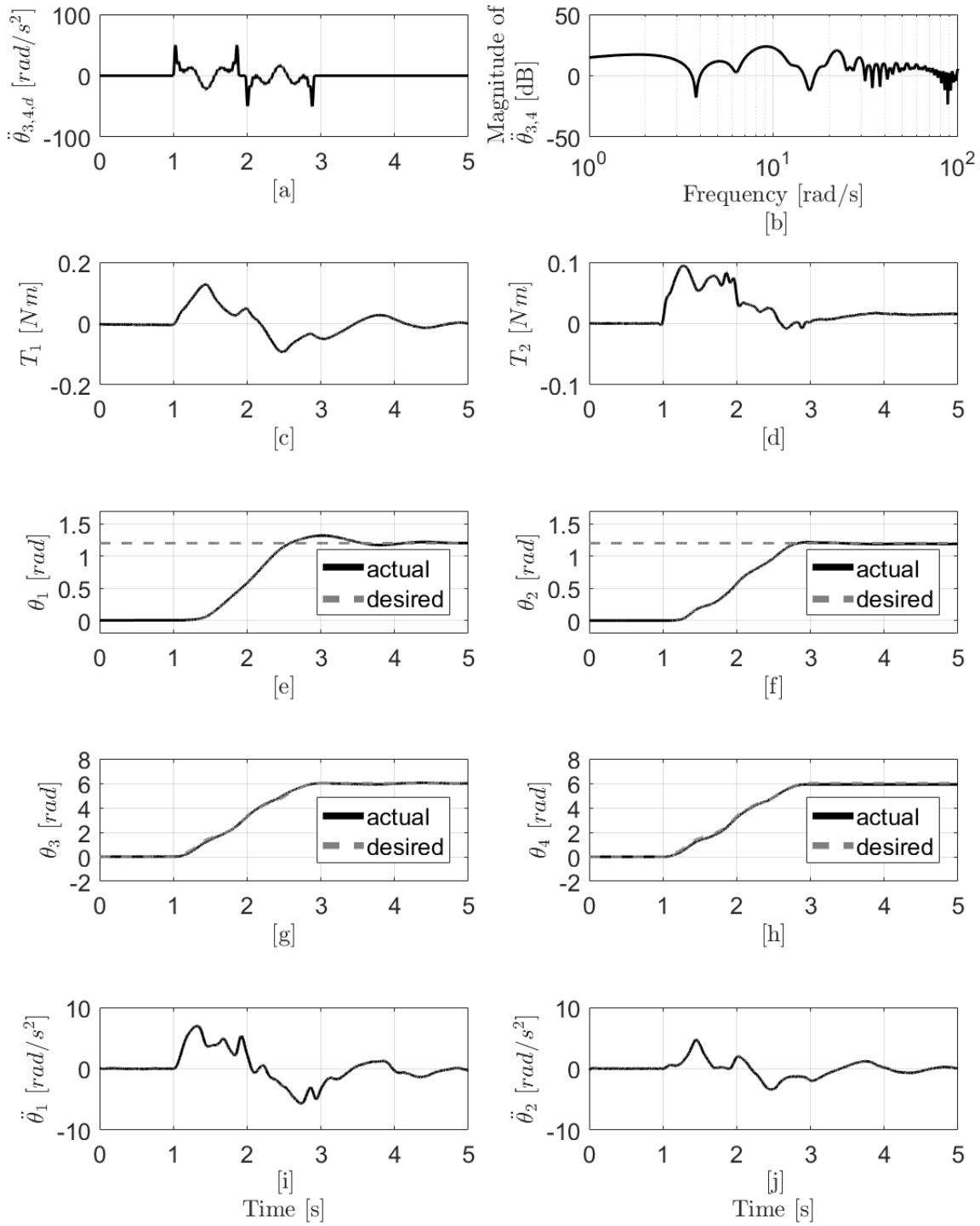

Figure 4.42. : Experimental Data of Versine Function with $a_{max} = 50$ rad/s^2 and $\rho = 2.7$.

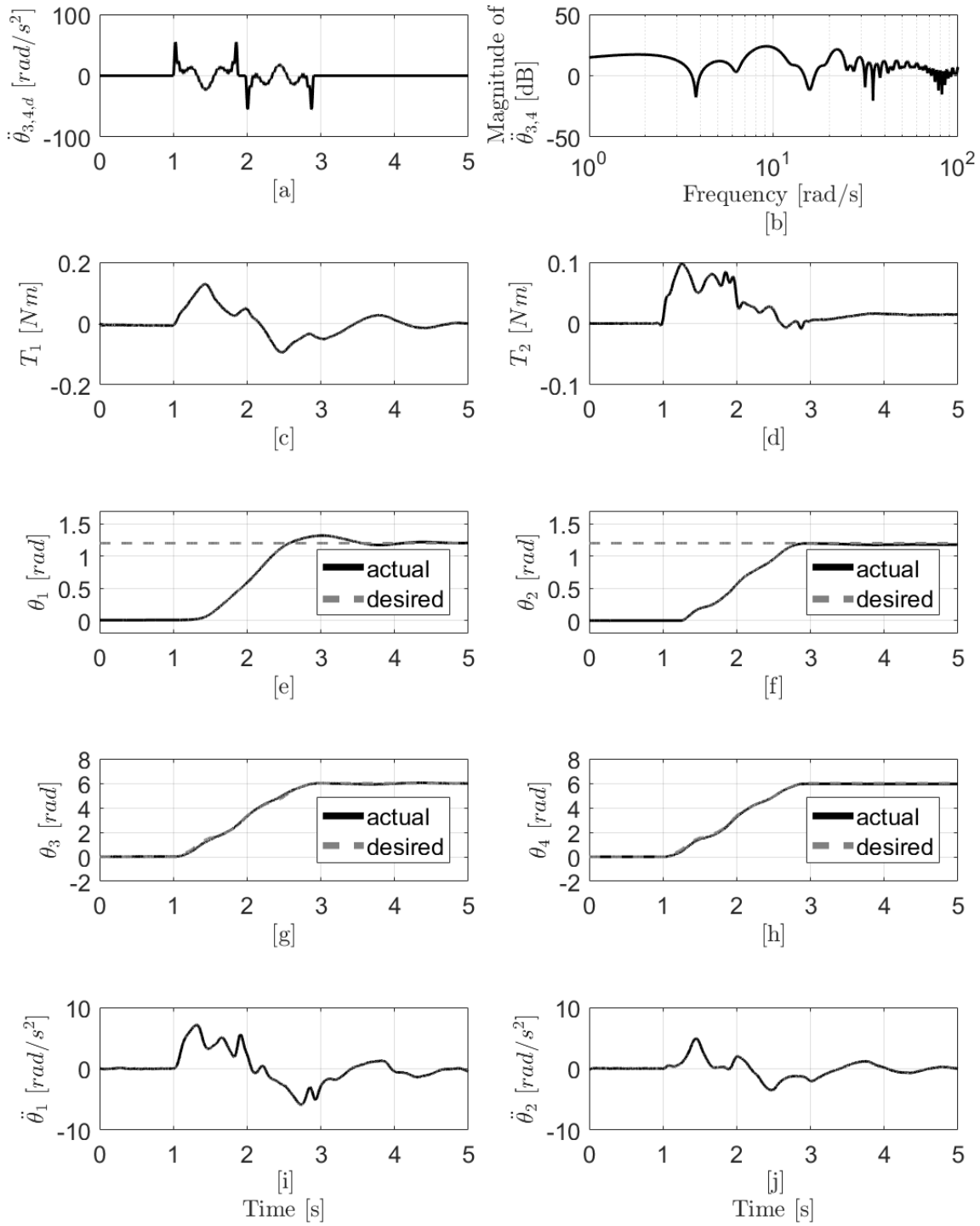

Figure 4.43. : Experimental Data of Versine Function with a_{max} = 55 rad/s^2 and $\rho = 3.4$.

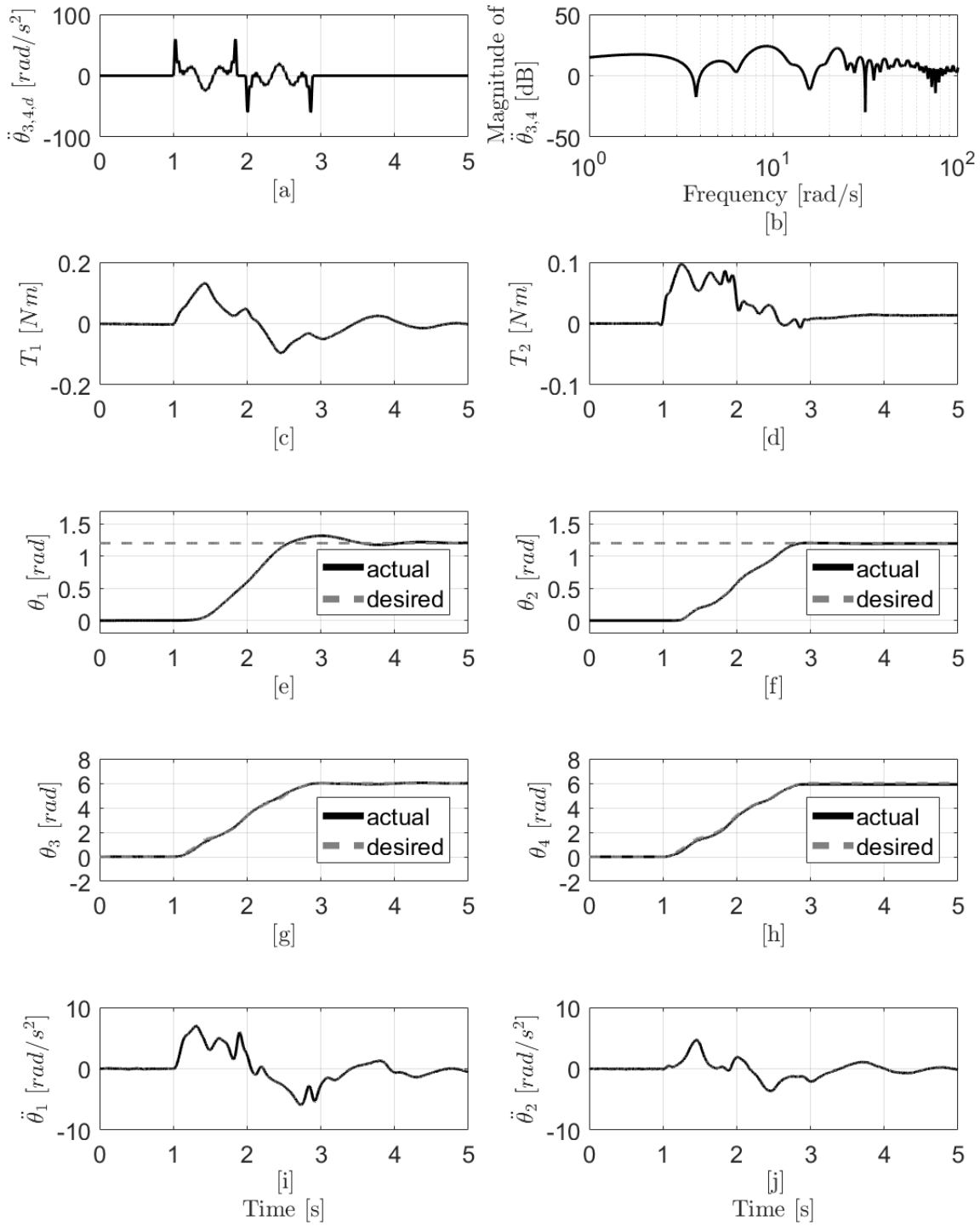

Figure 4.44. : Experimental Data of Versine Function with a_{max} = 60 rad/s^2 and $\rho = 3.5$.

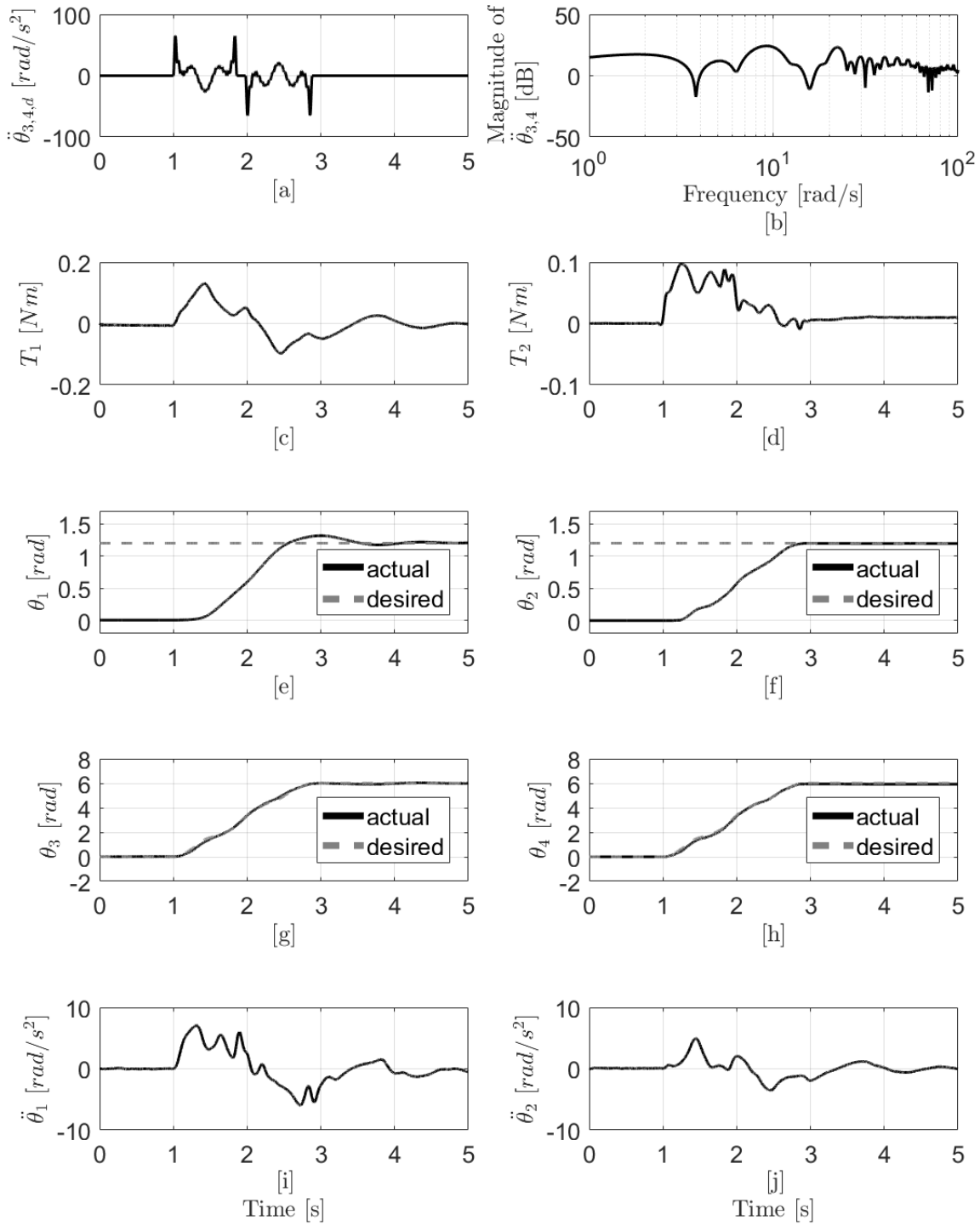

Figure 4.45. : Experimental Data of Versine Function with a_{max} = 65 rad/s^2 and $\rho = 4.5$.

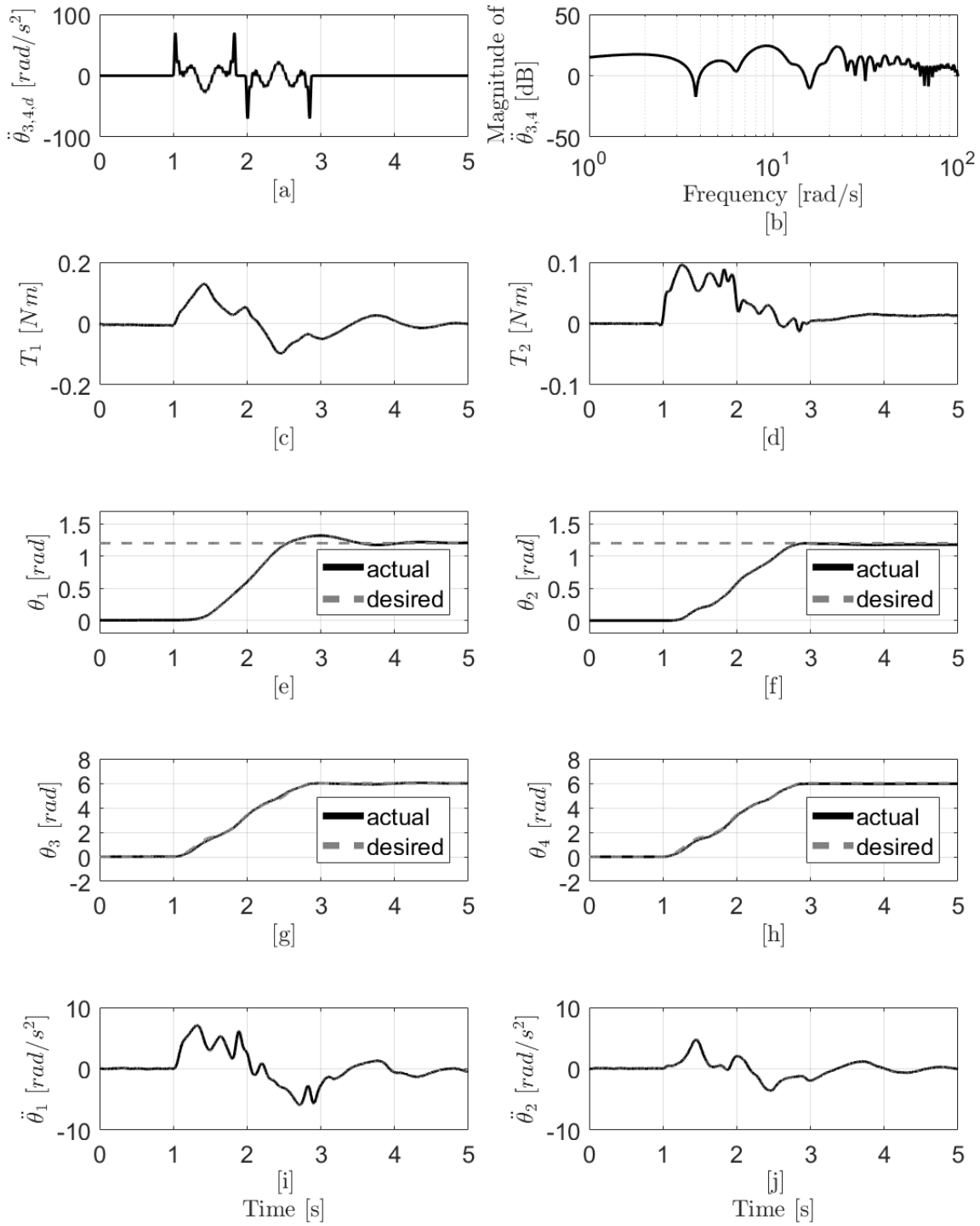

Figure 4.46. : Experimental Data of Versine Function with a_{max} = 70 rad/s^2 and $\rho = 6$.

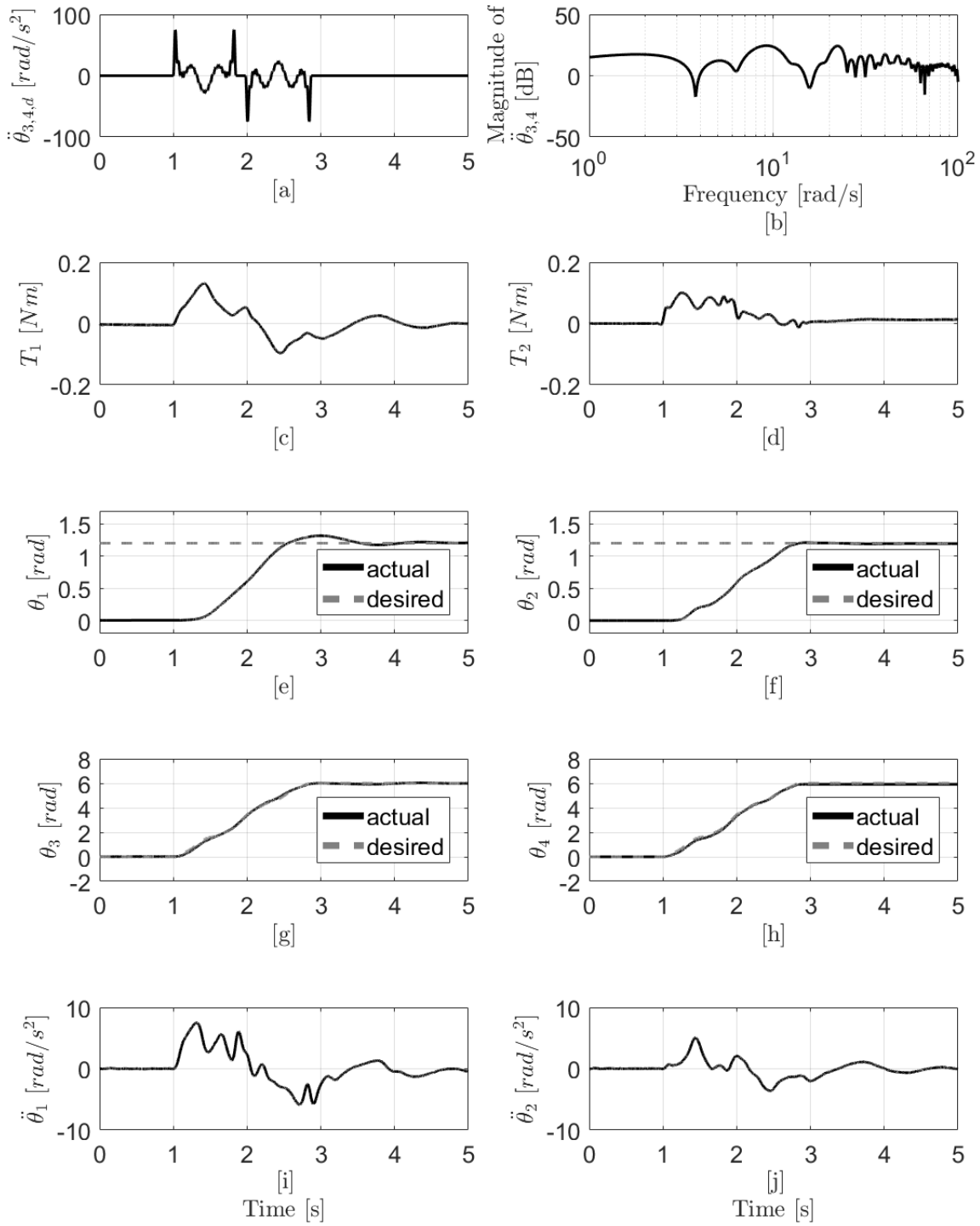

Figure 4.47. : Experimental Data of Versine Function with $a_{max} = 75$ rad/s^2 and $\rho = 8$.

5. CONCLUSION AND FUTURE WORK

5.1 Summary and Conclusions

In this work, the command shaping method with constrained peak input acceleration has been developed and implemented on a two-link flexible-joint robotic arm to minimize residual vibrations. It is based on the command shaping method with fixed actuation time, which needs a pre-determined actuation time and does not have control over input accelerations. Previous work proved the ability of the command shaping method to attenuate energy at selected frequencies, which reduces residual vibrations of a flexible-system, however, its lack of ability to incorporate motor torque limitations makes it less desirable. With the extension to the constrained input acceleration approach, profiles are determined with the input accelerations and weighting factor. Thus, less time is required when a more powerful motor has been installed. This is achieved with iterations of actuation time.

After the fundamental theory has been developed, the command shaping method with constrained peak input acceleration is tested with both simulations and experiments. The results confirmed that the new command shaping method successfully attenuates energy at selected frequencies. Both basis functions, ramped sinusoid and versine, performed as expected. The command shaping method with constrained peak input acceleration outperformed the bang-bang profile with a significant margin.

This improvement does not come without a price. The command shaping method cannot insert energy as efficiently as its comparable bang-bang profile, such that the actuation time would be longer than for the bang-bang profile. Based on simulations, the weight factor ρ, is the main parameter to weigh the trade-off between shorter settling time and less time penalty, which is a natural result of the inefficiency of the command shaping method, for given peak input acceleration. In addition, the wide window of frequency band with attenuated energy ensures robustness to modeling errors.

When comparing results from the two basis functions, profiles with ramped sinusoid functions tend to need less time to settle than profiles with versine functions when the peak input acceleration is above 35 rad/s^2. This is because profiles with versine functions have two separate segments, thus, the transition between acceleration and deceleration segments or acceleration and constant velocity segments or constant velocity and deceleration segments also has to be smooth to avoid excitation of system frequencies. On the other hand, since the whole ramped sinusoid profile is constructed with one segment, profiles with ramped sinusoid functions guarantee that no extra transition exists. Thus, the ability to limit peak velocity with versine functions also comes with a price, since actution time is longer.

Besides the differences, profiles generated with two basis functions share some common properties as well. The 1^{st} link tends to have more overshoot than the 2^{nd} link; both motors have good tracking on reference inputs without noticeable steady-state error; peak acceleration only lasts for a short amount of time; when the peak

input acceleration is doubled, the maximum torque from either motor only increases a relatively small amount.

This work confirms that the command shaping method with constrained peak input acceleration can effectively reduce residual vibrations of a two-link flexible-joint robotic arm without overconstraining the performance with a pre-determined actuation time.

A designer can take advantage of this work to generate a profile based on the input accelerations and input velocities and avoid the trial-and-error process on setting different actuation time in advance while improving the total move time.

5.2 Contributions

The primary contribution of this work is the application of the command shaping method with constrained peak input acceleration to a two-link flexible-joint robotic arm for the first time. From there, another benefit is the better understanding of how the combination of peak input acceleration and ρ impacts the residual vibrations and weighing the trade-off between actuation time and settling time. Thus, a method of selecting an optimal ρ for a given a_{max}, which warrants the least total move time, is given. Among all optimal cases, the total move time tends to be lower with higher peak input acceleration. In addition, the understanding of the inherent coupling between two modes and the focus on the endpoint leads to a unified performance metric to indicate the performance of each input profile.

There are other findings that suggest future work. The discovery that the relationship between input profile accelerations and actual torques is not exactly as expected suggests that the feedback controller is playing a significant role with the computed torque controller.

5.3 Recommendation for Future Work

With confirmed improvement of the command shaping method with constrained peak input accelerations, some issues during the course of this research suggest that more work may be valuable to explore.

Firstly, this work only specifies the start and end point regardless of the actual path on the Cartesian plane. As we all know, path-planning can also help reduce residual vibrations. For example, if flexibilities are known only to occur along the x-axis, a path that maximizes the motion along the y-axis would reduce residual vibrations noticeably. Thus, investigating the method of incorporating the path-planning with this work is promising to improve the performance.

Although the input profile effectively limits its peak acceleration, the actual profile reveals that it only requires a small amount of time to operate at its peak. Thus, the inefficiency of the command shaping method is apparent. Agrawal [31] developed an approach to address such issue with a new objective function and used a numerical method to find the solution. Since his approach requires iterations even with a fixed actuation time, higher demand on computational power would be evident for a simple combination of his work and this work, which would require two nested iterative

loops. However, this does suggest that addressing such issue may be possible and would potentially improve the command shaping method greatly.

Another area that is worthy to be explored is the influence of the feedback controller. As this work makes the command shaping method be able to generate a vibration-reduced profile with desired input accelerations, the actual motor torques do not change proportionally. This is mainly attributed to the feedback controller for the system, which is the computed torque controller in this application. The computed torque controller is nonlinear and does not give a direct relationship between input profile and torque output, which makes torques unknown when constructing input profiles. In addition, its nonlinearity also potentially introduces energy around natural frequencies, such that the ability of the command shaping method to reduce vibration is impaired.

Lastly, ρ affects the energy attenuation level differently on two different basis functions, which makes the comparison between them less straightforward. Normalizing the two terms in the objective function would possibly address the issue. In addition, all 22 points are weighted equally in the current objective function. Instinctively, the system natural frequencies usually do not have equal effect on residual vibrations. For example, in this work, the first mode has more impact than the second mode on residual vibrations. It is worthy to explore a method to weigh system natural frequencies differently, such that the performance can be improved while the inefficiency is not worsened.

LIST OF REFERENCES

LIST OF REFERENCES

[1] D. M. Aspinwall. Acceleration profiles for minimizing residual response. *Journal of Dynamic Systems, Measurement, and Control*, 102(1):3–6, 1980.

[2] R. L. Farrenkopf. Optimal open-loop maneuver profiles for flexible spacecraft. *Journal of Guidance, Control, and Dynamics*, 2(6):491–498, 1979.

[3] C. J. Swigert. Shaped torque techniques. *Journal of Guidance, Control, and Dynamics*, 3(5):460–467, 1980.

[4] J. D. Turner and J. L. Junkins. Optimal large-angle single-axis rotational maneuvers of flexible spacecraft. *Journal of Guidance, Control, and Dynamics*, 3(6):578–585, 1980.

[5] J. D. Turner and H. M. Chun. Optimal distributed control of a flexible spacecraft during a large-angle maneuver. *Journal of Guidance, Control, and Dynamics*, 7(3):257–264, 1984.

[6] A. L. Hale, W. Dahl, and J. Lisowski. Optimal simultaneous structural and control design of maneuvering flexible spacecraft. *Journal of Guidance, Control, and Dynamics*, 8(1):86–93, 1985.

[7] H. Sehitoglu and J. H. Aristizabal. Design of a trajectory controller for industrial robots using bang-bang and cycloidal motion profiles. *American Society of Mechanical Engineers, Dynamic Systems and Control Division (Publication) DSC*, 3:169–175, 1986.

[8] O. Smith. Posicast control of damped oscillatory systems. *Proceedings of the IRE*, 45(9):1249–1255, 1957.

[9] N. C. Singer. *Residual vibration reduction in computer controlled machines*. PhD thesis, Massachusetts Institute of Technology, 1989.

[10] N. K. Gupta. Frequency-shaped cost functionals-extension of linear-quadratic-gaussian design methods. *Journal of Guidance, Control, and dynamics*, 3(6):529–535, 1980.

[11] M. J. Balas. Enhanced modal control of flexible structures via innovations feedthrough. *International Journal of Control*, 32(6):983–1003, 1980.

[12] L. Meirovitch, H. F. VanLandingham, and H. Oz. Distributed control of spinning flexible spacecraft. *Journal of Guidance, Control, and Dynamics*, 2(5):407–415, 1979.

[13] M. J. Balas. Modal control of certain flexible dynamic systems. *SIAM Journal on Control and Optimization*, 16(3):450–462, 1978.

[14] H. Henrichfreise. The control of an elastic manipulation device using dsp. In *American Control Conference, 1988*, pages 1029–1035, June 1988.

[15] L. M. Sweet and M. Good. Re-definition of the robot motion control problem: Effects of plant dynamics, drive system constraints, and user requirements. In *Decision and Control, 1984. The 23rd IEEE Conference on*, pages 724–732. IEEE, 1984.

[16] S. Futami, N. Kyura, and S. Hara. Vibration absorption control of industrial robots by acceleration feedback. *Industrial Electronics, IEEE Transactions on*, (3):299–305, 1983.

[17] M. C. Readman. *Flexible joint robots*. CRC press, 1994.

[18] P. Tomei. A simple pd controller for robots with elastic joints. *Automatic Control, IEEE Transactions on*, 36(10):1208–1213, 1991.

[19] L. Tian and A. A. Goldenberg. Robust adaptive control of flexible joint robots with joint torque feedback. In *Robotics and Automation, 1995. Proceedings., 1995 IEEE International Conference on*, volume 1, pages 1229–1234. IEEE, 1995.

[20] H. Moulin and E. Bayo. On the accuracy of end-point trajectory tracking for flexible arms by noncausal inverse dynamic solutions. *Journal of dynamic systems, measurement, and control*, 113(2):320–324, 1991.

[21] J. Ghosh and B. Paden. Pseudo-inverse based iterative learning control for nonlinear plants with disturbances. In *Decision and Control, 1999. Proceedings of the 38th IEEE Conference on*, volume 5, pages 5206–5212. IEEE, 1999.

[22] C. Lin and Y. Hsiao. Adaptive feedforward control for disturbance torque rejection in seeker stabilizing loop. *Control Systems Technology, IEEE Transactions on*, 9(1):108–121, 2001.

[23] N. C. Singer and W. P. Seering. Preshaping command inputs to reduce system vibration. *Journal of Dynamic Systems, Measurement, and Control*, 112(1):76–82, 1990.

[24] S. P. Bhat and D. K. Miu. Precise point-to-point positioning control of flexible structures. *Journal of Dynamic Systems, Measurement, and Control*, 112(4):667–674, 1990.

[25] P. H. Meckl. *Minimizing residual vibration of a linear system using appropriately shaped forcing functions*. Master's thesis, Massachusetts Institute of Technology, 1984.

[26] P. H. Meckl. *Control of vibration in mechanical systems using shaped reference inputs*. PhD thesis, Massachusetts Institute of Technology, 1988.

[27] A. Azad, M. H. Shaheed, Z Mohamed, M. Tokhi, and H. Poerwanto. Open-loop control of flexible manipulators using command-generation techniques. *Flexible Robot Manipulators Modelling, Simulation and Control, London, United Kingdom: The Institution of Engineering and Technology*, pages 207–233, 2008.

[28] V. M. Beazel. *Command Shaping Applied to Nonlinear Systems with Configuration-Dependent Resonance*. PhD thesis, Purdue University, 2004.

[29] W. Chatlatanagulchai, V. M. Beazel, and P. H. Meckl. Command shaping applied to a flexible robot with configuration-dependent resonance. In *American Control Conference, 2006*, pages 6–pp. IEEE, 2006.

[30] L. Y. Pao and M. A. Lau. Robust input shaper control design for parameter variations in flexible structures. *Journal of dynamic systems, measurement, and control*, 122(1):63–70, 2000.

[31] A. Agrawal. *Constrained Optimized Command Shaping for Minimizing Residual Vibration in a Flexible-Joint Robot*. Master's thesis, Purdue University, 2015.

[32] A. Scheel, A. Agrawal, Y. Wu, N. Jacobs, and P. H. Meckl. Command shaping applied to a two-link flexibile-joint robot. *Journal of Dynamic Systems, Measurement, and Control*.

[33] J. D. Yegerlehner. *The Application of Artificial Neural Networks to the Control of Nonlinear SystemUndergoing Changes in a System Parameter*. Master's thesis, Purdue University, 1992.

[34] R. Kinceler and P. H. Meckl. Corrective input shaping for a flexible-joint manipulator. In *American Control Conference, 1997. Proceedings of the 1997*, volume 3, pages 1335–1339. IEEE, 1997.

[35] W. Chatlatanagulchai. *Backstepping Intelligent Control Applied to a Flexible-Joint Robot Manipulator*. PhD thesis, Purdue University, 2006.

[36] H. C. Nho. *Precise motion control of flexible-joint robot manipulators with an intelligent payload estimator*. PhD thesis, Purdue University, 2004.

[37] M. W. Spong. Modeling and control of elastic joint robots. *Journal of dynamic systems, measurement, and control*, 109(4):310–318, 1987.

[38] R. S. Lee. *Optimal parameter estimation for long-term prediction in the presence of model mismatch applied to a two-link flexible joint robot*. PhD thesis, Purdue University, 2011.

[39] B. Yao. Adaptive robust control of robot manipulators-theory and experiment. *IEEE Transactions on Robotics and Automation*, 10(5):705–710, 1994.